

DISSERTATION

DEVELOPMENT OF A NOVEL ENDOPROSTHESIS FOR CANINE LIMB-  
SPARING USING A FINITE ELEMENT APPROACH

Submitted by

Snehal Shetye

Department of Mechanical Engineering

In partial fulfillment of the requirements

For the degree of Doctor of Philosophy

Colorado State University

Fort Collins, Colorado

Fall 2010

Doctoral Committee:

Department Head: Susan P. James

Advisor: Christian M. Puttlitz

Susan P. James  
Brandon G. Santoni  
Paul R. Heyliger

Copyright by Snehal Sharadkumar Shetye 2010.

All Rights Reserved.

## ABSTRACT

### DEVELOPMENT OF A NOVEL ENDOPROSTHESIS FOR CANINE LIMB- SPARING USING A FINITE ELEMENT APPROACH

Osteosarcoma is the most prevalent bone tumor in the canine population and the distal radius is the most commonly affected site. To date, amputation has been the preferred treatment option among veterinarians for distal radius osteosarcoma. However, with the advent of better chemotherapy protocols and the subsequent increasing survival rates, interest has now turned towards saving the legs of dogs with osteosarcoma. The current endoprosthesis used for limb-sparing is associated with a high failure rate, and hence, the design of a novel endoprosthesis is warranted.

To aid in the development of a new endoprosthesis for canine limb-sparing a finite element model of the canine forelimb was generated. Accurate mechanical properties of soft tissues are essential to build a reliable finite element model. Since no data exists regarding the mechanical properties of canine carpal ligaments, six primary stabilizing ligaments of the canine carpus were identified and their mechanical properties were investigated by uniaxial testing in a materials testing machine.

Convergence and validation are two crucial steps in the development of a finite element model. Convergence was investigated by generating three models with increasing mesh resolution. For the purposes of validation, eight intact canine forelimbs were tested in a materials testing machine. The limbs were instrumented to record bone

strains and relative displacements. The acquired data were used to validate the canine forelimb model.

The current endoprosthesis was evaluated to determine the mechanical underpinnings of clinical failures associated with these implants using the canine forelimb finite element model. The implant failure locations predicted by the model were similar to those observed clinically. The use of a locking plate in place of the current non-locking plate was also investigated. Several stress redistribution strategies were also examined.

A novel modular design was developed in collaboration with the Colorado State University's Veterinary Teaching Hospital oncology surgeons. The design was extensively evaluated with the use of the validated and converged finite element of the canine antebrachium. The design was modified and improved based on the results. Significant stress reduction was achieved within the proximal radial screws and the distal metacarpal screws. Off-axis loading of the construct was also eliminated. The final design was approved for prototype development, biomechanical testing and cadaveric evaluation.

## Acknowledgements

I would like to thank my advisor Dr. Christian Puttlitz for all the help and guidance I received throughout the course of my PhD and for not being satisfied with mediocrity. I could not have finished this project without his constant support.

Thanks to my committee members Dr. Susan James, Dr. Paul Heyliger and Dr. Brandon Santoni for providing me with the necessary tools to successfully complete my doctoral dissertation.

Thanks to Dr. Stewart Ryan and Dr. Nicole Ehrhart for providing me with an excellent clinical perspective on canine distal radius osteosarcoma and helping with the design of the endoprosthesis.

I would like to thank all my colleagues (Dr. McGilvray, Dr. Ayturk, Kevin, Ben, Devin, Cecily, Amy, Dr. Womack) at the Orthopaedic Bioengineering Research Laboratory for their support and making my time in Fort Collins fun and enjoyable.

A special thanks to Ketan Malhotra for his help with testing the canine carpal ligaments.

Thanks to Dr. Robert E. Lee and Mr. Dennis Madden for providing all the canine forelimb specimens required for this study.

Special thanks go to my father (Sharadkumar Shetye) and mother (Shilpa Shetye) for funding my education and for their untiring support as I struggled through graduate school.

And finally, thanks to my wife - for everything.

*This dissertation is dedicated to my loving and beautiful wife, Runzun.*

## TABLE OF CONTENTS

ABSTRACT.....	ii
Acknowledgements.....	iv
1 Background.....	1
1.1 Anatomy of the Canine Antebrachium .....	1
1.1.1 Geometry .....	1
1.1.2 Joints and Ligaments.....	4
1.2 Material Properties .....	6
1.2.1 Bone .....	6
1.2.2 Articular Cartilage .....	8
1.2.3 Ligaments.....	10
1.3 History of Canine Limb-sparing.....	11
1.4 Finite Element Modeling.....	16
1.4.1 Material Properties .....	17
1.4.2 Convergence and Validation .....	18
1.5 Force Plate Analysis of Canine Gait.....	19
2 Specific Aims .....	20
2.1 Specific Aim #1: Determine the mechanical properties of canine carpal ligaments.....	20
2.2 Specific Aim #2: Develop a validated and converged model of the canine forelimb.....	20
2.3 Specific Aim #3: Evaluate the endoprosthesis currently used for canine limb sparing.....	21
2.4 Specific Aim #4: Design a novel endoprosthesis using the finite element model of the canine forelimb .....	21
3 Mechanical Properties of Canine Carpal Ligaments .....	22
3.1 Introduction .....	22

3.2	Methods.....	23
3.3	Results.....	26
3.4	Discussion.....	29
4	Model Development.....	33
4.1	Model Generation.....	33
4.1.1	Geometry.....	33
4.1.2	Material Properties.....	36
4.2	Model Convergence.....	39
4.3	Model Validation.....	42
4.3.1	Cadaver Experiments.....	42
4.3.2	Validation Results and Discussion.....	44
5	Evaluation of Current Generation Endoprosthesis.....	48
5.1	Introduction.....	48
5.2	Model Development.....	49
5.3	Endoprosthesis Evaluation Results.....	52
5.4	Discussion.....	57
6	Novel Endoprosthesis Design.....	60
6.1	Introduction.....	60
6.1.1	Locking Vs. Non-locking Plates.....	61
6.1.2	Locking & Non-locking Screws.....	62
6.2	Preliminary Design Iterations (Methods and Preliminary Results).....	63
6.3	Final Design Rationale and Evaluation.....	69
6.3.1	Modular design.....	69
6.3.2	Ease of alignment between the proximal radius section and the carpus.....	71
6.3.3	Stress reduction within the radial screws.....	73
6.3.4	Procedure for implantation of endoprosthesis.....	74
6.4	Results.....	75
6.4	Discussion.....	80
6.4.1	Tie Constraint Stress Predictions.....	84
7	Conclusion.....	86
8	References.....	88

## LIST OF FIGURES

Figure 1-Canine forelimb regions.....	1
Figure 2-Canine antebrachial region bones.....	2
Figure 3-Canine carpal region bones (two layers).....	2
Figure 4-Canine metacarpal region bones (adapted from [1]).....	3
Figure 5—Illustrations of the palmar (A) and lateral (B) views of the left forelimb of a dog that indicates the anatomic locations of the 6 ligaments harvested for testing. V = Metacarpal bone V. ....	6
Figure 6- Hierarchical structure of bone.....	8
Figure 7- Layered structure of cartilage.....	9
Figure 8- Representative graphs depicting stiffness obtained from a load-displacement curve (A) and elastic modulus obtained from a stress-strain curve (B). ....	11
Figure 9-Endoprosthesis and dedicated limb-sparing bone plate available for distal radial limb-sparing surgery in dogs. (A) Disassembled view; (B) assembled view, top; (C) assembled view, side. Note the flared distal end of the endoprosthesis (arrow). (Adapted from Liptak <i>et al.</i> ).....	14
Figure 10- (A) Endoprosthesis implanted in patient (B) Radiograph of canine forelimb with implanted endoprosthesis.....	15
Figure 11- 2nd (current) generation endoprosthesis employing significant weight reductions... ..	16
Figure 12-A typical stress-strain curve for 316L type stainless steel (cold worked).....	18
Figure 13-Photographs of the area micrometer (A) and the experimental apparatus containing a ligament specimen with 3 reflective markers (arrows) affixed to it (B).....	24
Figure 14-Mean $\pm$ SD elastic modulus for each of the 6 canine ligaments.....	27
Figure 15-Mean $\pm$ SD ultimate strength for each of the 6 canine ligaments.....	28
Figure 16-Segmentation of cortical bone in AMIRA.....	33
Figure 17-Three models of the canine forelimb with increasing mesh resolutions. ....	34
Figure 18-Ligaments represented as nonlinear one-dimensional spring elements (arrows).....	36
Figure 19-Nonlinear hyper elastic material behavior applied to all cartilage layers.....	37
Figure 20-Non-linear force-displacements curves for the six primary carpal ligaments obtained from <i>in vitro</i> experiments.....	38
Figure 21-Convergence model parameters. ....	39
Figure 22-Convergence data summary. All values are presented as percentage difference compared to the high resolution model.....	39
Figure 23-Principal strains at location 1.....	40
Figure 24-Principal strains at Location 2.....	41
Figure 25-Principal strains at Location 3.....	41

Figure 26-Total contact area for the radiocarpal joint .....	42
Figure 28-Location of strain gauge rosettes on the radius and ulna .....	43
Figure 29-Construct for testing of canine forelimbs (H=Humerus, C=Radius, P=Bottom potting box) .....	43
Figure 30-Comparison of strain predictions from the model with values from the validation experiments .....	46
Figure 31-Comparison of minimum principal strain predictions from the model with values from the validation experiments .....	47
Figure 32-Comparison of max. principal strains between the two loading regimes (Intact Vs. Tendon Resection) .....	47
Figure 33-Endoprosthesis spacer .....	49
Figure 34-Dynamics Compression Plate (DCP) .....	49
Figure 35-Radius with holes created in TrueGrid for insertion of proximal screws .....	49
Figure 37-Non-locking plate and screw design used for evaluating the current generation endoprosthesis. A coefficient of friction value of 0.25 was set between the plate and screw heads.....	51
Figure 36-Final model incorporating the current endoprosthesis construct .....	50
Figure 38-An ulnar pin was inserted to evaluate the possible biomechanical contribution of the ulna .....	52
Figure 39-von Mises stress distribution within the proximal radial screws. ....	53
Figure 40-von Mises stress distribution within the radius.....	53
Figure 41-von Mises stress distribution within the distal metacarpal screws.....	54
Figure 42-von Mises stress distribution within the 3rd metacarpal bone.....	54
Figure 43-von Mises stress distribution within the endoprosthesis spacer screws. Arrow indicates location of maximum stress. ....	55
Figure 44-von Mises stress distribution within the endoprosthesis spacer. Arrow indicates location of maximum stress.....	55
Figure 45-von Mises stress distribution within the dynamic compression plate. ....	56
Figure 46-Comparison of von Mises stress predictions between the non-locking and locking constructs.....	57
Figure 47-Greater stress dissipation can be observed within the radius for the locking plate construct (B) as compared to the non-locking plate construct (A). ....	59
Figure 48-Idealized representations of the radius and 3rd metacarpal bones .....	63
Figure 49-Proposed initial design 1 for the endoprosthesis.....	63
Figure 50-Proposed initial design 2 for the endoprosthesis.....	64
Figure 51-First iteration based on requirements of the oncology surgeons .....	65
Figure 52-Lip (arrow) provided at the distal end of the PEC for added stability of the distal end of the radius .....	66
Figure 53-Implant evaluated using the idealized bone constructs.....	67
Figure 55-DEC with screws at a 15 degree angle (Iteration 3) .....	68
Figure 54-DEC with a zero degree bend (Iteration 2) .....	68
Figure 56-Final proximal component.....	70

Figure 57-Final mid-diaphyseal component (MEC).....	70
Figure 58-Final distal endoprosthesis component.....	71
Figure 59-The preoperative apparatus for installation of new endoprosthesis.....	72
Figure 60-Individual components of the apparatus .....	73
Figure 61-von Mises stress distribution in the distal metacarpal screws. ....	76
Figure 62-von Mises stress distribution in the proximal radius screws.....	76
Figure 63-von Mises stress distribution in the radius.....	77
Figure 64-von Mises stress distribution in the 3 <sup>rd</sup> metacarpal. ....	77
Figure 65-von Mises stress distribution in the PEC.....	78
Figure 66-von Mises stress dsitribution in the MEC. ....	78
Figure 67-von Mises stress distribution in the DEC. ....	79
Figure 68-Comparison of peak von Mises stresses for three support conditions(Base, distal support, ulnar support).....	80
Figure 69-High bending stresses (arrows) due to removal of intramedullary stem support. ....	80
Figure 70-Location of max. von Mises stress after ignoring the stress concentrations due to tie constraints .....	82
Figure 71-Abnormal stress concentration caused by tie constraints.....	83

# 1 Background

## 1.1 Anatomy of the Canine Antebrachium

### 1.1.1 Geometry

The canine thoracic limb consists of the scapular, axillary, brachial, cubital, antebrachial, carpal, metacarpal and phalangeal regions [Figure 1]. The current study focuses on the antebrachiocarpal, carpal and metacarpal regions. The antebrachial region consists of the radius and ulna [Figure 2]. The carpal region consists of a total of seven bones divided into two transverse layers. The proximal layer consists of the radial carpal, ulnar carpal and the accessory carpal bones and the distal layer in the carpal region consists of the numbered carpal bones I-IV [Figure 3]. The metacarpal region consists of the numbered metacarpal bones I-V [Figure 4].

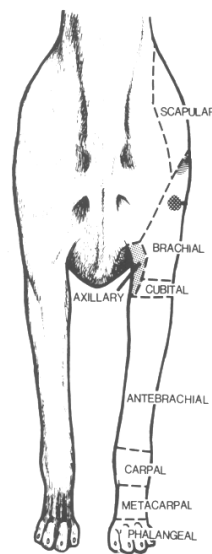
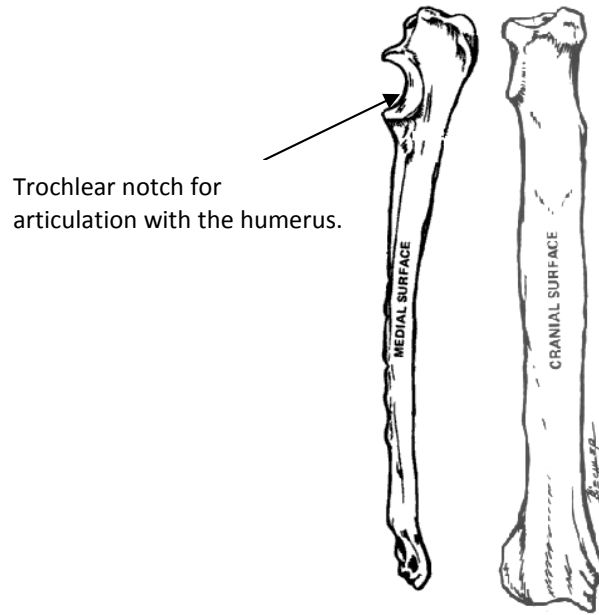
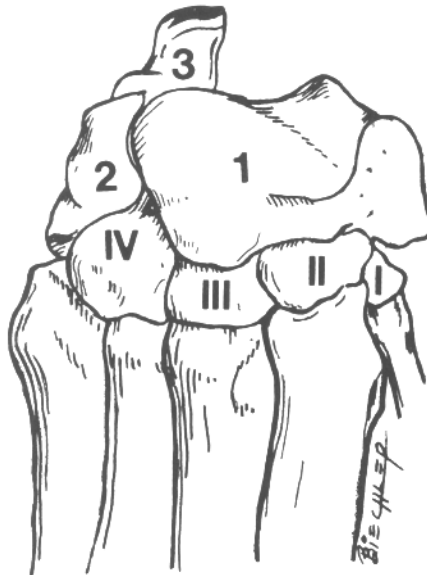


Figure 1-Canine forelimb regions.



**Figure 2-Canine antebrachial region bones (adapted from [1]).**

The radius is the main weight-supporting bone of the forearm. It articulates proximally with the humerus bone forming the elbow joint and distally with the radial carpal bone. The radius also articulates with the ulna proximally (by its caudal surface) and distally (by its lateral border) [3].



**Figure 3-Canine carpal region bones (two layers) (adapted from [1]).**

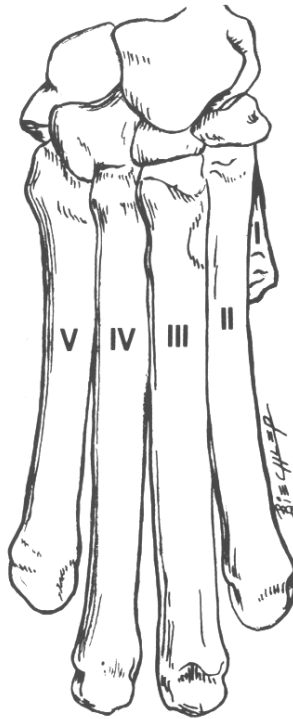


**Figure 4-Canine metacarpal region bones (adapted from [1]).**

The ulna, which is the longest bone of the canine skeleton, extends from the elbow to the carpus. A large trochlear notch [Figure 2] at the proximal end of the ulna articulates with the humerus. At the distal end, the lateral styloid process of the ulna articulates with the ulnar carpal and the accessory carpal bones and also with the ulnar notch of the radius [3].

The radius and ulna bones articulate proximally with the humerus. The load transferred through the humerus is shared equally at the proximal end of both bones [4]. Both the radius and ulna consist of a raised, oval rough area at the middle third of the bones. This is where the interosseous ligament attaches. As compared to the interosseous ligament present in the human forearm, this ligament is much shorter (~2cm) [5]. An interosseous membrane exists on both sides of the ligament and attaches to the opposed interosseous crests of the radius and ulna [3]. This membrane is perforated at various points for the passage of various arteries, veins

and the interosseous nerve. As compared to the human forearm, only a small amount of rotational movement is allowed between these two bones.

The carpus represents the region between the forearm and the metacarpus. The radial carpal bone is the largest of all the carpal bones. It articulates proximally with the radius and distally with the four numbered carpal bones. Laterally, the radial carpal bone articulates extensively with the ulnar carpal bone. The ulnar carpal bone, which is smaller than the radial carpal bone, articulates proximally with the radius and ulna, distally with the fourth and fifth metacarpal, medially with the radial carpal and on the palmar side with the accessory carpal.

The metacarpal bones II-V are the primary load-bearing bones of the metacarpus. The Metacarpal I bone is quite small and slender, and does not bear any load.

### **1.1.2 Joints and Ligaments**

The radius and the ulna are joined together with the proximal and distal radioulnar synovial joints and the strong interosseous ligament along with the weak interosseous membrane [3].

The triangular fibrocartilage present at the distal end of the ulna and radius in humans is referred to as the articular disc in canine anatomy [6-8]. The smooth distal end of this articular disc forms 10% of the articular surface of the antebrachiocarpal joint [7].

The antebrachiocarpal joint exists between the distal part of the radius and ulna and the proximal row of carpal bones [3]. The middle carpal joint is defined between the two rows of carpal bones and the carpometacarpal joint is located between the distal row of the carpal bones and the metacarpus. The whole carpal joint acts like a hinge joint (ginglymus), allowing flexion and extension with limited lateral movement [5]. The intermetacarpal joints are close-fitting joints between the proximal ends of the metacarpal bones. The bones are joined together by fibrous tissues called the interosseous metacarpal ligaments [3].

Numerous ligaments exist to ensure stability of the carpal joint. The flexor retinaculum and the palmar carpal fibrocartilage are two primary structures that ensure the integrity of the carpal joint. The flexor retinaculum has two sleeves (superficial and deep) with tendons located between them [3]. The palmar carpal fibrocartilage is a thick cartilagenous structure that covers the palmar aspect of all carpal bones and the proximal parts of metacarpals III, IV and V. It smoothes the irregularities at the carpo-metacarpal joint and provides a smooth surface for the carpal canal [3]. It is also the primary structure that prevents hyperextension of the carpal joint.

The medial and lateral collateral ligaments (MC, LC) of the carpus limit valgus and varus movement of the carpal joint, respectively. These ligaments are primarily stabilizing ligaments. The medial collateral ligament originates from a tubercle above the styloid process of the radius and terminates at the most medial part of the radial carpal bone. A second oblique part, after originating from the styloid process, runs obliquely to the palmaromedial surface of the radial carpal bone [3]. The lateral collateral ligament originates at the styloid process of the ulna and inserts at the most lateral aspect of the ulnar carpal bone [Figure 5].

Along with the palmar carpal fibrocartilage, the palmar radiocarpal (PR) and the palmar ulnocarpal (PU) intra-articular ligaments prevent hyper-extension of the carpal joint [9] [Figure 5]. The palmar ulnocarpal ligament connects the ulna with the radial carpal bone. A short leaf of this ligament also connects with the accessory carpal bone. The palmar radiocarpal bone connects the radius with the radial carpal bone. The primary ligaments that prevent hyper-extension of the carpo-metacarpal joint are the accessorometacarpal ligaments [9]. Both originate from the accessory carpal bone. The accessorometacarpal-IV (AMC-IV) ligament, after originating from the accessory carpal bone, inserts in the metacarpal-IV bone and the accessorometacarpal-V (AMC-V) ligament attaches with the metacarpal-V bone [Figure 5].

Numerous other short ligaments unite the carpal bones transversely holding them together in the two rows [3].

Many published papers have investigated the canine carpal joint anatomically. Mikic et al. [6] provided a detailed analysis of the antebrachio-carpal joint in dogs using radiographs and gross dissection. Nordberg et al. [10] used magnetic resonance imaging to investigate the anatomy of normal canine carpal ligaments. Turan et al. [11] used computed tomography to examine the morphology of the carpal tunnel. Warnock et al. [12] used arthroscopy to comprehensively examine the ligaments and bones of the canine antebrachio-carpal joint.

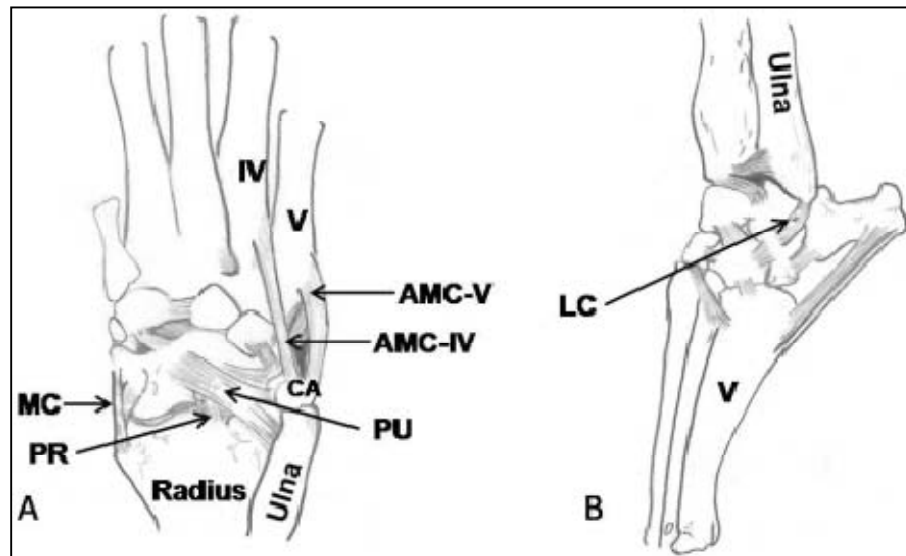


Figure 5—Illustrations of the palmar (A) and lateral (B) views of the left forelimb of a dog that indicates the anatomic locations of the 6 ligaments harvested for testing. V = Metacarpal bone V.

## 1.2 Material Properties

### 1.2.1 Bone

Bone has a complex hierarchical structure [Figure 6]. At the nanostructural level, it is composed of apatite crystals and collagen fibrils [13]. These fibrils combine to form collagen fiber bundles. At the microstructural level, the collagen fibers form into lamellae or haversian canals with

concentric layers of lamellae. Groups of haversian canals are referred to as osteons which are approximately 10-500 $\mu$ m in diameter [1]. Hydrated bone consists of around 20% water with the mineral phase constituting 77% of the remainder [14]. 90-95% of the organic phase consists of Type I collagen [15]. Collagen fibrils contribute significantly to the anisotropy of bone [16]. From a macrostructural point of view, bone can be broadly classified as cortical (dense) or trabecular (porous) bone. All long bones have a dense cortical shell and trabecular bone exists interiorly within this shell. These two types of bone can be generally distinguished by the relative amount of porosity they exhibit, however, there exists some controversy as to whether they both have the same microstructure [1, 17, 18].

Bone exhibits a capacity for self repair. Trabecular bone is generally more active and gets remodeled faster as compared to cortical bone [1]. Osteoclasts are primarily responsible for bone resorption and osteoblasts are responsible for bone formation. The disruption of the functions of these bone cells can cause osteoporosis, osteopenia and other related diseases.

The macrostructural mechanical properties of cortical bone have been reported in various studies . The longitudinal moduli of cortical bone ranges from 5 to 22 GPa and also varies with respect to age, species and orientation [19-22]. There is a positive correlation between elastic modulus of bone and the applied strain rate [23]. The macrostructural mechanical properties of cancellous bone are significantly lower as compared to the microstructural properties. The Young's moduli of trabecular bone range from 100-4000 MPa [14, 24]macrostructurally, however, nanoindentation of trabecular struts have reported

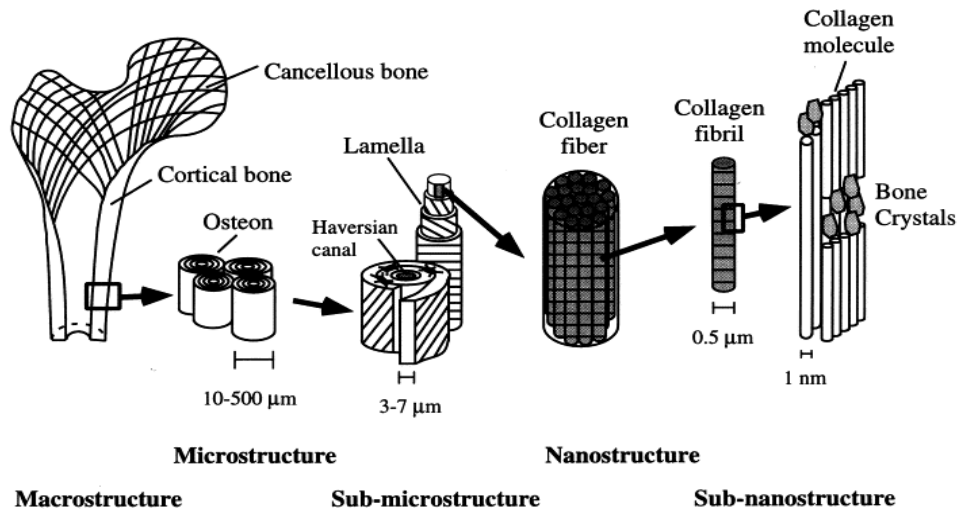


Figure 6- Hierarchical structure of bone (adapted from Rho et al. [1]).

Young's moduli of 15-20 GPa [25]. Cortical and trabecular bone exhibit anisotropy [21]. The orientation of trabecular spicules is preferentially along the primary mechanical loading configuration [21].

Care must be taken when using canine trabecular bone as a model for human bone. Kuhn et al. [26] showed qualitative similarities between canine cancellous bone and human bone, however some quantitative differences were observed. Several studies have investigated the material properties of canine cortical and trabecular bone [26-29]. Kaneps et al. [29] investigated the changes that occurred in canine cortical bone following immobilization and consequent remobilization with exercise. They showed decreased mechanical properties following immobilization for canine cortical and cancellous bone.

### 1.2.2 Articular Cartilage

Cartilage is an avascular, connective tissue and is present in all diarthrodial joints. Articular cartilage is composed of 68-85% water, 10-20% collagen and 5-10% of proteoglycan by weight [30]. The most common form of cartilage is hyaline cartilage. Other forms of cartilage include fibrocartilage (intervertebral disc, meniscus) and elastic cartilage (ear, larynx) [30]. Hyaline

cartilage is most generally found at the articulating ends of long bones and on bones within a synovial joint. Cartilage degeneration is a major cause for the onset of osteoarthritis in joints.

Articular cartilage is a multiphasic structure with two phases: a fluid phase which consists of water and electrolytes and a solid phase consisting of collagen, proteoglycans, chondrocytes and proteins. It is generally regarded in literature as a layered medium with four zones as shown in Figure 7 [2].

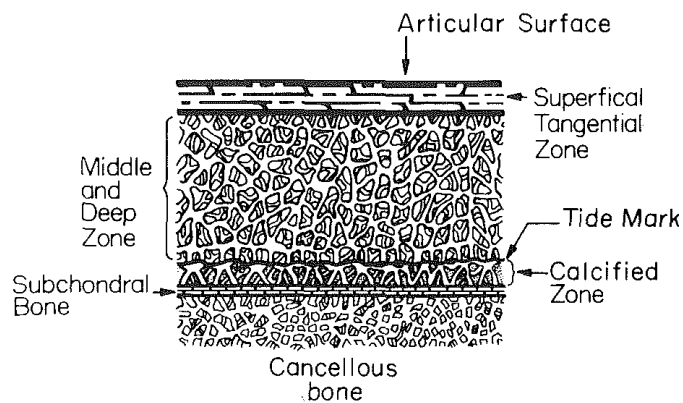


Figure 7- Layered structure of cartilage (adapted from Mow et al. [2]).

Initial attempts at finite element modeling of articular cartilage modeled the tissue as isotropic and linearly elastic. Later, numerous viscoelastic models were proposed, however they failed to take into account the interstitial fluid flow. When cartilage is compressed, water is pushed out and when soaked in fluid, it absorbs water [31]. Currently, the most popular theories for cartilage behavior have been the biphasic theory proposed by Mow et al. [2] and the triphasic theory proposed by Lai et al. [32] that takes into account the Donnan osmotic pressure effects.

To date, the compressive mechanical properties of canine carpal cartilage have not been investigated. Elliot et al. [33] investigated the tensile properties of canine knee articular cartilage. Instantaneous moduli for human articular cartilage (knee) vary from 5-14 MPa [34, 35] which is highly dependent upon strain magnitude and orientation. Physiological strains above

15% have been reported in articular cartilage [36], which is expected given its relatively low modulus. Proteoglycan-induced swelling pressures and interstitial fluid contribute heavily to the hyperelastic response, preventing excessive compressive strains [14].

### **1.2.3 Ligaments**

Ligaments are soft connective tissues that support load only in tension. They aid in the stability of diarthrodial joints and guide motion. Rupture of ligaments generally leads to abnormal joint kinematics, pain and osteoarthritis [30]. Immobilization of joints has been shown to adversely affect the connected soft tissues in terms of their mechanical properties and mass [37].

Ligaments are mainly composed of parallel bundles of type I collagen, elastin, proteoglycans, glycolipids and water (65-70% of total weight). Ligaments have a hierarchical structure composed of fibrils, fibers, subfascicular units, fascicule and the tissue level structure [30]. The ligament insertions to bone are of two types: direct and indirect. In a direct insertion, the transition from ligament to bone occurs in four phases: ligament, fibrocartilage, mineralized fibrocartilage and bone [30]. Indirect insertions consist of superficial fibers connected to the periosteum and deep fibers (Sharpey fibers) connected to the bone.

There exist numerous standardized protocols for obtaining the mechanical properties of ligaments. Since ligaments connect bone to bone, the whole bone-ligament-bone complex is excised for uniaxial testing. The load-deflection curve obtained can be used to determine the structural properties [Figure 8] of the ligament substance. Various techniques have been used for the measurement of the cross-sectional area of ligaments [30, 38, 39] which is needed for stress calculations. The resultant stress-strain curve can be used to obtain the mechanical properties of the ligament substance. Controversy exists in methods used for measuring the strain in the ligament. Crosshead displacement generally does not provide accurate local

deformation measurement of the ligament substance. In contrast, extensometers and stereophotogrammetry techniques have been used to obtain high fidelity local strain values.

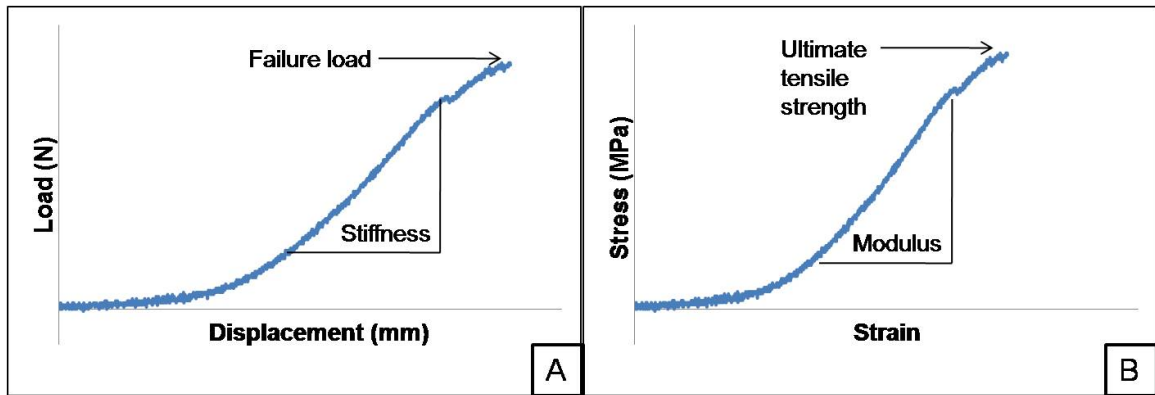


Figure 8- Representative graphs depicting stiffness obtained from a load-displacement curve (A) and elastic modulus obtained from a stress-strain curve (B).

Nearly all ligaments display nonlinear elastic behavior. The stretching of crimped collagen fibers contribute to the nonlinear toe region observed in the initial part of the load-deformation curve. To this date, no published literature exists that has investigated the mechanical properties of canine carpal ligaments.

### 1.3 History of Canine Limb-sparing

Osteosarcoma (OSA) is a debilitating disease afflicting nearly 8000 dogs every year in the USA [40]. It selectively affects large and giant breed dogs with occurrences increasing with age [40-42]. Males have a slightly higher predilection than females towards the development of osteosarcoma [40, 42]. However, neutered dogs have twice the risk when compared to sexually intact dogs [42]. Increasing weight and height have also been shown to be associated with an increased risk of osteosarcoma [42]. The metaphyseal region of long bones is the most frequently affected site, with front limbs affected twice as often as rear limbs [40]. Pure-breed dogs have a higher predilection for osteosarcoma as compared to mixed-breed dogs [43].

Canine osteosarcoma which has many similarities to human osteosarcoma, also serves well as a model to study the etiology, behavior and treatment of osteosarcoma [44, 45]. It is more common among dogs than humans. Also, the disease progresses faster in dogs and hence the efficacy of various treatment protocols can be reported earlier in the treatment period. Furthermore, the costs associated with clinical trials of dogs are considerably less as compared to human clinical trials. Osteosarcoma is a relative uncommon disease among humans. It affects children and young adolescents. Approximately 400 cases of osteosarcoma are reported every year [46]. The current survival rate for human osteosarcoma patients is around 60% [45].

Historically, the gold standard for the treatment of canine osteosarcoma has been amputation [44, 47-50]. For dogs treated with amputation alone, metastasis caused early death with a survival rate of merely 10% after one year [40]. The addition of adjuvant chemotherapy protocols has improved the survival rate up to 60% [40]. The chemotherapy drug, cisplatin has been shown to increase the median survival time after amputation. Carboplatin and doxorubicin are second-generation drugs that have been used for adjuvant chemotherapy, however, they have not shown greater or equal survival rates as compared to cisplatin [49, 51]. Recently, several studies have investigated combination chemotherapy protocols which involve a combined use of cisplatin or carboplatin and doxorubicin [50]. Studies have also investigated the use of radiation therapy in place of chemotherapy [45, 52]. However, the use of radiation therapy alone is highly detrimental and results in poor local tumor control [52].

Generally, the mobility and quality of life after amputation is acceptable to the owners and even large and giant breed dogs often function satisfactorily [47]. However, there are some instances where limb-sparing is preferred over amputation. Dogs with severe orthopaedic conditions and

giant breeds can benefit greatly from limb-sparing. Also, some owners absolutely refuse amputation.

Owing to the good results obtained from amputation along with adjuvant chemotherapy protocols, the interest has now turned to saving the legs of the dogs afflicted with osteosarcoma. No differences in survival rates have been found between amputation with cisplatin and limb-sparing with cisplatin [48]. Dogs with osteosarcoma in the distal radius are an ideal candidate for limb-sparing treatment since arthrodesis of the antebrachio-carpal joint does not affect the overall function of the limb. In contrast, arthrodesis of the elbow joint has resulted in poor limb function [53]. Limb-sparing is recommended when the tumor is limited to less than 50% of the diaphysis of the afflicted bone [40]. Dogs undergoing limb-sparing are commonly treated with some form of preoperative treatment such as intra-arterial cisplatin and radiation therapy [40, 54]. Currently, dogs are also treated with some local chemotherapy implantation during surgery.

Traditionally, limb-sparing has utilized a massive cortical allograft in conjunction with a dynamic compression plate [52]. The allograft is filled with polymethylmethacrylate to enhance screw union within the intramedullary canal. The effect of polymethylmethacrylate on allograft union in a canine model has been investigated by Straw et al. [55] and no adverse effects on allograft healing were reported. However, the management of massive cortical bone allografts is a costly and time-consuming process. The maintenance of a bone bank requires personnel and the non-availability of allografts is also a cause for concern.

Owing to the above mentioned issues related to cortical allografts, a metal endoprosthesis was developed [56] [Figure 9, Figure 10]. However, the failure rates (40%) associated with these endoprostheses have been reported to be similar to those observed with massive cortical

allografts [56]. The major contributing factors for failure observed in the metal endoprosthesis design were loss of screw purchase in the proximal radius and shear failure of the screw. These were attributed to the high discrepancy between the stiffness of the metal spacer compared to bone and the weight of the metal endoprosthesis. Interestingly, the cortical allograft implants demonstrated failure at the interface between the metacarpal bone and screws [56].



**Figure 9-Endoprosthesis and dedicated limb-sparing bone plate available for distal radial limb-sparing surgery in dogs. (A) Disassembled view; (B) assembled view, top; (C) assembled view, side. Note the flared distal end of the endoprosthesis (arrow). (Adapted from Liptak *et al.*)**

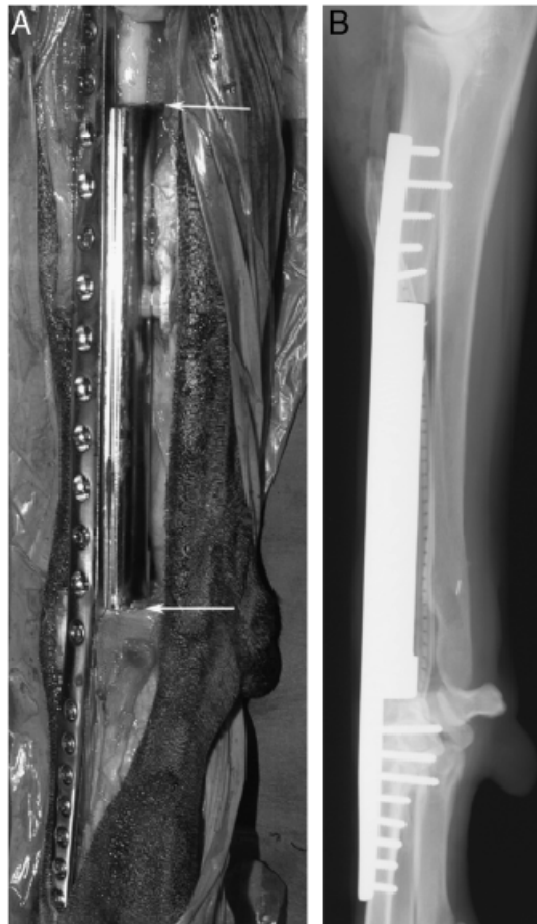


**Figure 10-(A) Endoprosthesis implanted in patient (B) Radiograph of canine forelimb with implanted endoprosthesis.**

A second generation metal endoprosthesis [Figure 11] was developed which employed significant weight reduction strategies to combat the high failures rates associated with the first generation model. However, this design has not been clinically or biomechanically tested. Another important, yet uninvestigated, issue related to canine limb sparing is the resection of the ulna. Traditional surgery practice dictates the partial resection of the ulna if the tumor is adherent to it [40]. Practically, the resection of the ulna makes it easier for the surgeon to perform the limb sparing surgery effectively. A biomechanical study [57] investigated the effect of ulna resection along with limb-sparing.

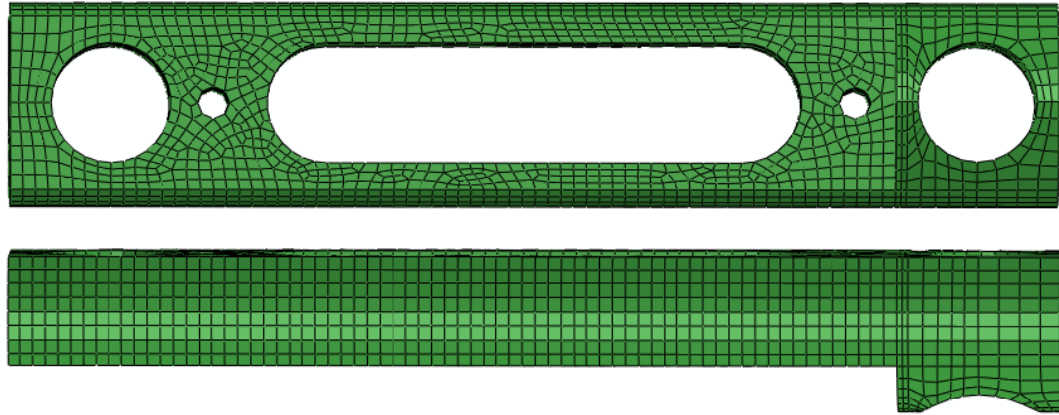


**Figure 11- 2nd (current) generation endoprosthesis employing significant weight reductions.**

They found no significant difference between failure loads for forelimbs with or without ulna resection. However, local stress redistribution to the radius was not examined. Therefore, discordance between these biomechanical test results and those observed clinically by veterinarians exists.

#### **1.4 Finite Element Modeling**

The first recorded application of the finite element method in orthopaedic tissue was by Brekelmans et al. [58, 59] wherein it was applied as a two-dimensional analysis of the human femur. Since that seminal paper, the finite element method has been applied to numerous biological tissues. Multiple studies have used the finite element method to analyze the human wrist joint [60-67]. Ulrich *et al.* [66] used an FE model of the radius, scaphoid and lunate to analyze the load transfer characteristics of the distal radius. Rogge *et al.* [67] used an FE model of the distal radius to investigate the fixation stability of pins used in distal radius fractures. More recently, Troy and Garbiner [65] investigated the failure of the distal radius caused by off-axis loads using an FE model of the human wrist. The mechanical behavior of the carpal bones after transaction of the transverse carpal ligament was investigated by Guo et al. [68] using a sophisticated finite element model of the human wrist. A very comprehensive model of the

human wrist has been developed by Gislason *et al.* [63] to investigate maximal grip loading in the human wrist. Interestingly, most of the aforementioned models have used tetrahedral elements for simulating the contact surfaces. The only FE study involving canine antebrachial bones was performed by Coleman *et al.* [69] which investigated the required epiphyseal loads to simulate *in vivo* strain fields.

#### **1.4.1 Material Properties**

Cortical bone has been modeled as an isotropic and linearly elastic material with a Young's modulus ( $E$ ) 10-20.1GPa and a Poisson's ratio  $\nu=0.2-0.4$  [60, 63, 65, 68] in FE models of the human wrist. Trabecular bone has been generally modeled as a single block of elements with  $E=100-4000$  MPa [14, 24] and  $\nu=0.2-0.4$  [60, 63, 65]. Some studies have used CT-based density data to incorporate local variation in mechanical properties of trabecular bone [14, 70]. Cartilage has been modeled as linearly elastic and isotropic with  $E=1-48$  MPa and  $\nu=0.3-0.49$  [60, 63, 65]. Some later studies have modeled cartilage as a non-linear hyperelastic material. Ligaments have been traditionally modeled as either linearly elastic, hyperelastic and as discrete linear and non-linear one-dimensional spring elements [65, 71]. Some have also included the nonlinear toe region and ligament pretension in their formulae [14].

##### **1.4.1.1 Metallic Biomaterials**

The two most common metallic alloys used in the manufacturing of metallic biomedical implants are 316L surgical stainless steel and Ti6Al4V titanium alloy. Both have been shown to be well-tolerated in a biological environment after implantation. ASTM recommends 316L stainless steel which exhibits better corrosion resistance as compared to 316 steel [72]. Both 316L (cold worked) and Ti6Al4V have similar tensile strengths of approximately 860MPa [73]. 316L has yield strength of 695MPa and Ti6Al4V has yield strength of 795MPa [73]. The advantage of using titanium alloys is the absence of artifacts during post-operative radiographic evaluation of

fracture healing. However, the cost of titanium implants is significantly higher as compared to stainless steel implants. The fatigue limit of Ti6Al4V at 10 million cycles (500MPa) is significantly higher than 316L (200MPa) in a simulated body environment [73, 74]. However, the fretting endurance limits of both materials are comparable [74]. Most of the commercially available 316L cortical screws are cold worked [73] and hence the material properties are approximately the same. Figure 12 shows atypical stress-strain curve for austenitic 316L stainless steel.

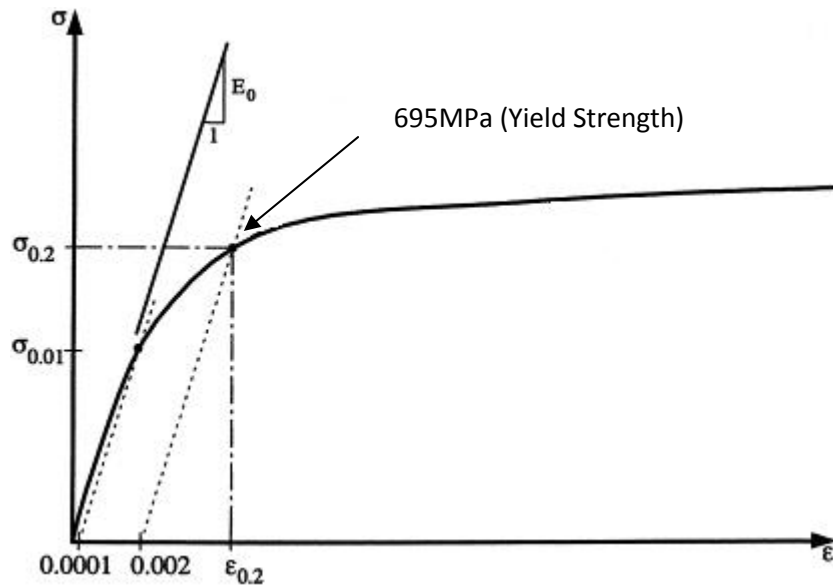


Figure 12-A typical stress-strain curve for 316L type stainless steel (cold worked).

### 1.4.2 Convergence and Validation

Convergence and validation are two often neglected steps needed for the development of a reliable finite element model. Most of the above mentioned FE models fail to provide any convergence data. Previous literature [75, 76] has made it clear that approximate analyses, like the FE method should provide a rigorous accounting of the reported mesh refinement results. The tolerance used for convergence should also be provided. It is generally accepted that no finite element model can be considered completely validated when simulating biological tissue

[77], however, it is critically important to experimentally validate the specific parameters of interest. It is also important to validate the numerical model under a variety of loads to exclude any possibility of coincidental agreement.

## **1.5 Force Plate Analysis of Canine Gait**

Force plates are used for the kinetic analysis of gait. The first ever recorded force plate application was in 1916 [78]. The initial force plates used only mechanical systems for force measurement, and hence, required very large forces to obtain adequate displacement. Since the late 1950's most force plate systems have used strain gauges for measurement of force. The first study to use the force plate system on canines used it to compare the gait of dogs treated with total hip replacements or excisional arthroplasty for the treatment of hip dysplasia [79]. Later, the seminal work of Budsberg et al. [80] analyzed the kinetics of the walking gait in healthy dogs. They reported that the forelimb encounters 70% BW of vertical load at the peak of the walking gait cycle as compared to 43% BW at the hind limb. A later study by Budsberg *et al.* [81] evaluated the kinetics of gait in healthy dogs at trot. At trot, the forelimb encounters 110% BW of vertical load, as compared to 70% BW at the hind limb. Extensive kinematic analyses have also been performed using force plates and stereophotogrammetry [82-87]. Hottinger et al. [84] analyzed the kinematics of walking in healthy large breed dogs. They provided extensive data on joint angles at the cubital and the antebrachioacarpal joint during a normal gait cycle. More recently, Nielsen et al. [85] provided a comprehensive kinetic and kinematic gait assessment of a healthy canine thoracic limb at walk.

## **2 Specific Aims**

From the preceding it is clear that the current endoprosthesis is not an acceptable solution for limb-sparing of dogs afflicted with distal radius osteosarcoma. Our overarching goal is to design a novel endoprosthesis which has improved mechanical integrity and provides a functional limb to the dog. In order to achieve this goal, we propose the following specific aims.

### **2.1 Specific Aim #1: Determine the mechanical properties of canine carpal ligaments**

Accurate mechanical properties of soft tissue such as ligaments and cartilage are required for the development of an accurate finite element model. No data is currently available regarding the mechanical properties of canine carpal ligaments, Therefore, in this aim, six primary stabilizing ligaments of the canine carpal joint under uniaxial tensile loading will be tested. The force-displacement data will be implemented in the FE model of the canine forelimb in the subsequent specific aim.

### **2.2 Specific Aim #2: Develop a validated and converged model of the canine forelimb**

Clinical evaluation of novel prostheses design involves a significant financial and time investment. Finite element modeling provides a faster and cheaper alternative to clinical trials. We propose to develop, validate and converge a finite element model of the canine forelimb which will aid in the evaluation of the current generation endoprosthesis (Specific Aim #3) as well facilitate in the development of novel designs (Specific Aim #4). Comprehensive mechanical data will be collected from the *in vitro* testing of intact canine forelimbs in order to achieve thorough validation of the finite element model. Three models with increasing mesh resolutions will also be created for establishing model convergence.

### **2.3 Specific Aim #3: Evaluate the endoprosthesis currently used for canine limb sparing**

The current endoprosthesis used in canine limb-sparing is associated with a failure rate of 40%. However, the exact mechanical underpinnings associated with these high clinical failure rates remain unknown. It is proposed to evaluate this endoprosthesis using the finite element model of the canine antebrachium. Finite element models of the current generation endoprosthesis will be created using ABAQUS (SIMULIA, Providence, RI) and implanted in the intact FE model as per standard surgical protocols. The efficacy of the implant will be evaluated by applying physiological loads that are equivalent to the force experienced by the canine forelimb during trot.

### **2.4 Specific Aim #4: Design a novel endoprosthesis using the finite element model of the canine forelimb**

Considering the mechanical limitations of the current generation endoprosthesis learnt from Specific Aim 3, we propose to develop a novel endoprosthesis for canine limb-sparing. The finite element model of the canine forelimb will be a critical element in the development of this implant. Two novel prostheses will be developed and designed within the size, weight and physiological limitations associated with the canine forelimb. The finite element models of the novel endoprosthesis designs will be implanted in the validated and converged finite element model of the canine forelimb and tested under a load of 110% BW (trot).

### **3 Mechanical Properties of Canine Carpal Ligaments (Original Publication: Shetye SS, Malhotra K, Ryan SD, Puttlitz CM, Determination of Mechanical Properties of Canine Carpal Ligaments, American Journal of Veterinary Research, August, 2009)**

#### **3.1 Introduction**

The antebrachium in dogs is prone to several conditions that can adversely affect function. These include ligamentous injury, fracture, luxation, osteoarthritis, and primary bone neoplasia. Treatment of these conditions often requires pancarpal arthrodesis. Implants used in pancarpal arthrodesis must withstand substantial loads, especially because plates are most often applied to the compression side of the radiocarpal joint [88]. In dogs with osteosarcoma of the distal portion of the radius, limb-sparing surgery has been successfully performed by means of primary tumor resection and placement of an allograft or metal endoprosthesis during pancarpal arthrodesis. Many currently used metal limb-sparing endoprostheses are large [56, 89] and composed of stainless steel. It has been hypothesized that these implants are affected by factors such as excessive weight, which may contribute to fixation failure. Investigators have compared the metal endoprosthesis and allograft limb-sparing techniques in a prospective clinical study [56] and a biomechanical study [57]. There was discordance between failure-mode results for the acute biomechanical testing and for the dogs in the clinical study. The most common failure mode of these endoprostheses in clinical situations is loss of screw purchase in the proximal radius bone, which leads to loosening of the device and the need for further surgical intervention, such as revision surgery or limb amputation [56]. To date, design modifications to the endoprosthesis have not been evaluated with rigorous biomechanical testing or prospective clinical trials. From the standpoint of design development of an implant, testing these implant modifications in vivo requires a substantial investment of resources (namely, time, money, and cadaveric tissue). The finite element method has been used to develop computational models of the human carpus [65, 68]. A finite element model of the

canine radius has been developed to determine loading conditions that result in replication of in vivo strain fields [69]. However, to our knowledge, development of a comprehensive finite element model of the canine carpal joint has not been reported. Our laboratory group has developed a computational (finite element) model of the canine antebrachium from the elbow joint to the metacarpal bones to enable virtual evaluation of prostheses and modifications to surgical procedures used in the canine antebrachium to predict failure modes and optimize implant design. The key steps in developing an accurate finite element model include simulating the anatomic structures (geometric aspects) and assigning the appropriate material properties to the constituent components of the model. Stiffness of the ligaments in the human wrist has been reported [90]. However, fundamental anatomic differences exist between the antebrachial joints of humans and dogs [6]; therefore, these data cannot be directly extrapolated to canine tissues. Additionally, we are not aware of any published reports that provide descriptions of the mechanical properties of canine carpal ligaments. Therefore, the objective of the study reported here was to establish a relevant dataset of the force-displacement and stress-strain relationships of the ligaments in the canine forelimb to provide data for incorporation into a finite model of the canine antebrachium.

### **3.2 Methods**

**Sample population**—Twenty-six carpal sections were collected from the cadavers of 13 dogs. The mean ( $\pm$  SD) body weight of the dogs (7 females and 6 males) was  $28.7 \pm 5.69$  kg. The dogs were euthanized for reasons unrelated to this study.

**Sample collection and preparation**—Six ligaments of interest (AMC-IV, AMC-V, PR, PU, MC, and LC) were collected. Because of size and anatomic limitations, all 6 ligaments were unable to be harvested from each dog. The forelimbs were disarticulated at the shoulder joint and frozen ( $-20^{\circ}\text{C}$ ) until dissection. For dissection, forelimbs were thawed; ligaments were then isolated as

bone-ligament-bone preparations (with at least 10 mm of bone included on each side of each ligament), wrapped in gauze soaked in saline (0.9% NaCl) solution, and stored again at  $-20^{\circ}\text{C}$  until the day of testing. Specimens were thawed at ambient temperature for 8 hours prior to mechanical testing. The bone-ligament-bone preparations were potted in PMMA and coupled to custom-designed mechanical fixtures. All possible care was used to ensure that the long axis of the ligament was aligned with the tensile axis of a servohydraulic materials testing machine. In addition, the PMMA pot at one end of each ligament was attached to a universal joint that allowed orientation of the ligament along the tensile axis when tension was applied.

**Measurement of cross-sectional area and length**— To transform the load data into stress variables, the cross-sectional area of each ligament was measured by use of a custom-designed apparatus that included a high-resolution micrometer [Figure 13]. A compressive load was applied across the cross-sectional area, which resulted in a constant pressure of 0.12MPa [39]. Because of the shape of the fixture, the cross-sectional area under consideration was modeled as a rectangle and its corresponding dimensions were the height of the specimen (as determined by the value obtained by use of the micrometer) and the width of the fixture occupied by the ligament.

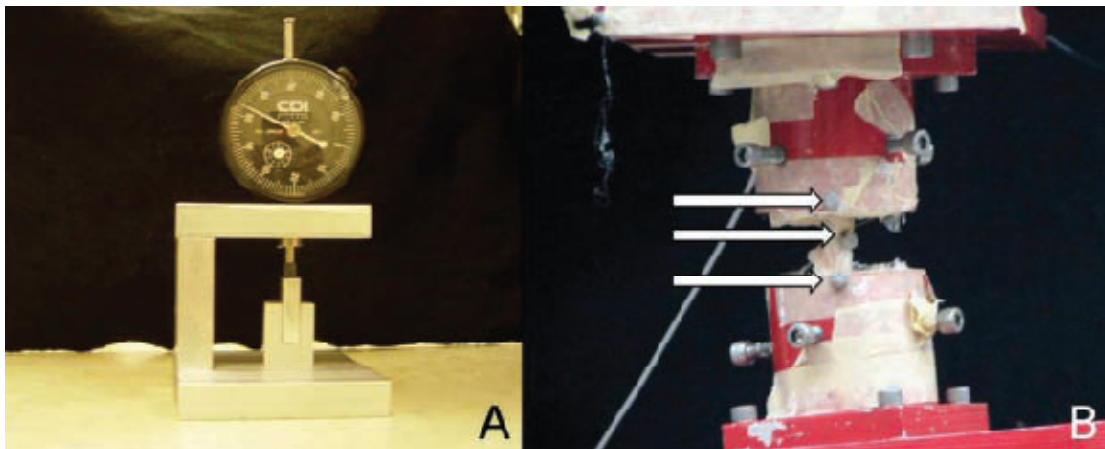


**Figure 13-Photographs of the area micrometer (A) and the experimental apparatus containing a ligament specimen with 3 reflective markers (arrows) affixed to it (B).**

Cross-sectional areas for the PR, MC, and LC ligaments were measured with handheld Vernier calipers because of the small dimensions of these ligaments.

**Mechanical testing**—Quasi-static tensile tests were performed on all specimens (n = 8 specimens/ligament) by use of a servohydraulic MTS in conjunction with a six degree-of-freedom load cell. Each specimen was preconditioned for 10 cycles by applying a 2% maximum strain via a Haversine waveform. Tension was subsequently applied at a strain rate of 0.5%/s to each specimen until ligament failure, which was defined as a sharp reduction in the monotonically increasing load-displacement data. Stereophotogrammetry was used to ensure there was no slippage between the fixtures and PMMA during testing. Specifically, 3 reflective markers were affixed to specimens in the experimental apparatus (1 was affixed on each of the 2 mechanical fixtures, and the third was sutured to the midpoint of the ligament; Figure 13). These markers were tracked via real-time monitoring by use of a 3-camera system. When slippage was detected during any portion of the testing, the resultant specimen data were excluded from the analysis.

**Data analysis**—Force and displacement data were synchronized by use of a light-emitting diode that was triggered by the MTS software and recorded by means of the stereophotogrammetry cameras during testing. Data were recorded at the same rate (60 Hz) by use of the MTS and camera system. Displacement data were obtained from the MTS, and the resultant strain was calculated by use of the equation  $\varepsilon = (l_f - l_o)/l_o$ , where  $\varepsilon$  is the engineering strain,  $l_f$  is the final ligament length, and  $l_o$  is the initial ligament length. Force data obtained by use of the MTS were divided by the cross-sectional area of the specimen to obtain the engineering normal stress (i.e.,  $\sigma$ ). The resultant stress-strain data were plotted, and the stiffness coefficient was obtained as the slope of the linear region of the associated force-displacement curve. In addition, slope of the linear region was used to obtain the elastic modulus (i.e., Young's modulus) of the ligament.

Failure load for each specimen was obtained at the maximum point in the load-displacement plot from the MTS. The failure mode for each ligament was also recorded. Stiffness, elastic modulus, ultimate strength, and cross-sectional area were compared across the ligament population by use of a one-way ANOVA with the Student-Newman-Keuls *post hoc* test for multiple comparisons. All data were evaluated for normality. A rank transformation was performed on data that were not normally distributed. Ligaments were also stratified into 3 groups: the AMC ligaments [AMC-IV and AMC-V], the intra-articular ligaments [PR and PU], and the palmar carpal ligaments [MC and LC]. Value of  $p < 0.05$  was considered significant.

### **3.3 Results**

Mean values of elastic modulus for each ligament were determined [ Figure 14]. The mean modulus did not differ significantly ( $p = 0.142$ ) between AMC-IV and AMC-V ligaments. The AMC-IV ligament had the highest mean ( $\pm$  SD) elastic modulus of all ligaments tested with a value of  $546.06 \pm 106.97$  MPa, followed by the MCV ligament with a mean modulus of  $382.38 \pm 180.50$  MPa. Elastic moduli did not differ significantly between the PU and PR ligaments ( $p = 0.856$ ) or between the MC and LC ligaments ( $p = 0.196$ ). Values for elastic modulus differed significantly ( $p < 0.001$ ) among the 3 ligament groups. Mean stiffness coefficients for each ligament were determined. Mean  $\pm$  SD stiffness did not differ significantly ( $p = 0.095$  or greater for all comparisons) among the MC ( $72.65 \pm 10.86$  N/mm), LC ( $61.10 \pm 30.42$  N/mm), PR ( $80.20 \pm 41.21$  N/mm), PU ( $94.70 \pm 14.43$  N/mm), and AMC-IV ( $72.33 \pm 14.66$  N/mm) ligaments. Mean stiffness of the AMC-V ligament ( $145.864 \pm 49.44$  N/mm) was significantly ( $p = 0.014$  or greater for all comparisons) higher than that for all other ligaments. Mean failure loads for each ligament were determined. Mean ( $\pm$  SD) failure loads did not differ significantly ( $p = 0.84$  or greater for all comparisons) among the AMC-IV ( $426.15 \pm 100.79$  N), MC ( $392.45 \pm 132.61$  N), and PU ( $414.66 \pm 72.29$  N) ligaments.

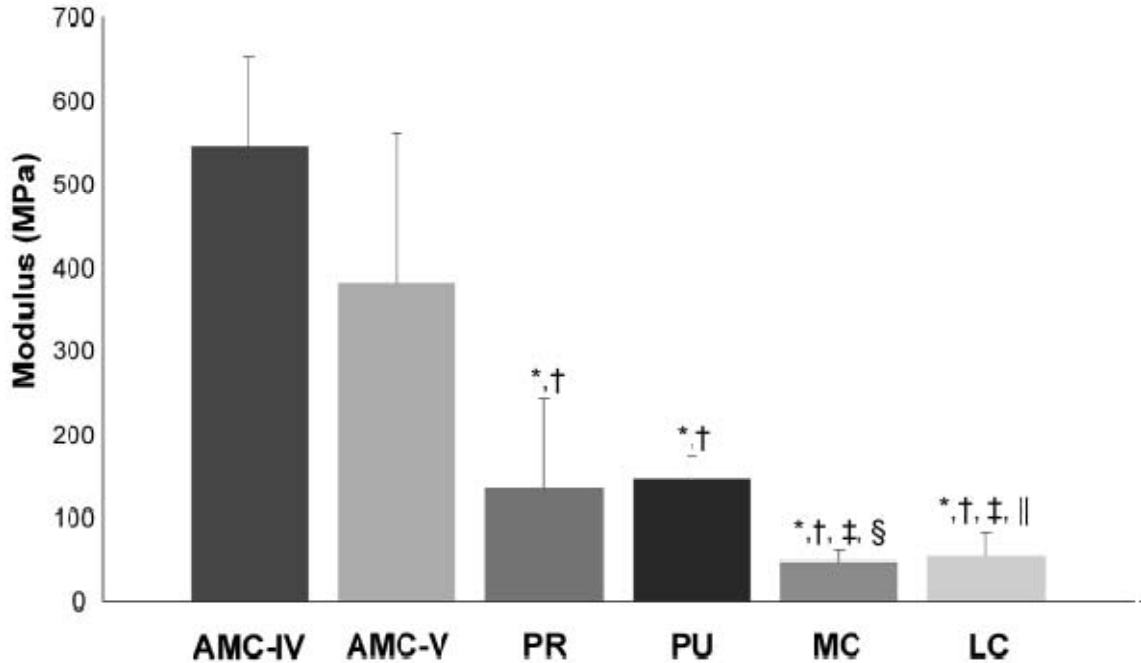


Figure 14-Mean  $\pm$  SD elastic modulus for each of the 6 canine ligaments (n = 8 specimens/ ligament) evaluated. Values for elastic modulus differ significantly ( $p < 0.001$ ) among the 3 ligament groups (group 1 comprised the AMC-IV and AMC-V ligaments, group 2 comprised the PR and PU ligaments, and group 3 comprised the MC and LC ligaments). \*Value differs significantly ( $p < 0.001$ ) from the value for the AMC-IV ligament. †Value differs significantly ( $p = 0.001$ ) from the value for the AMC-V ligament. ‡Value differs significantly ( $P < 0.001$ ) from the value for the PU ligament. §Value differs significantly ( $p = 0.007$ ) from the value for the PR ligament. || Value differs significantly ( $P = 0.004$ ) from the value for the PR ligament.

Ligament	Type of Failure		
	Midsubstance	Bone-Ligament Interface	Bony Avulsion
AMC-IV	3	2	3
AMC-V	1	6	1
PR	5	1	2
PU	7	0	1
MC	7	0	1
LC	5	0	3

Table 1- Failure modes (n = 8 specimens/ligament) for each of the 6 canine ligaments, categorized on the basis of the location of the failure detected during load-to-failure tests.

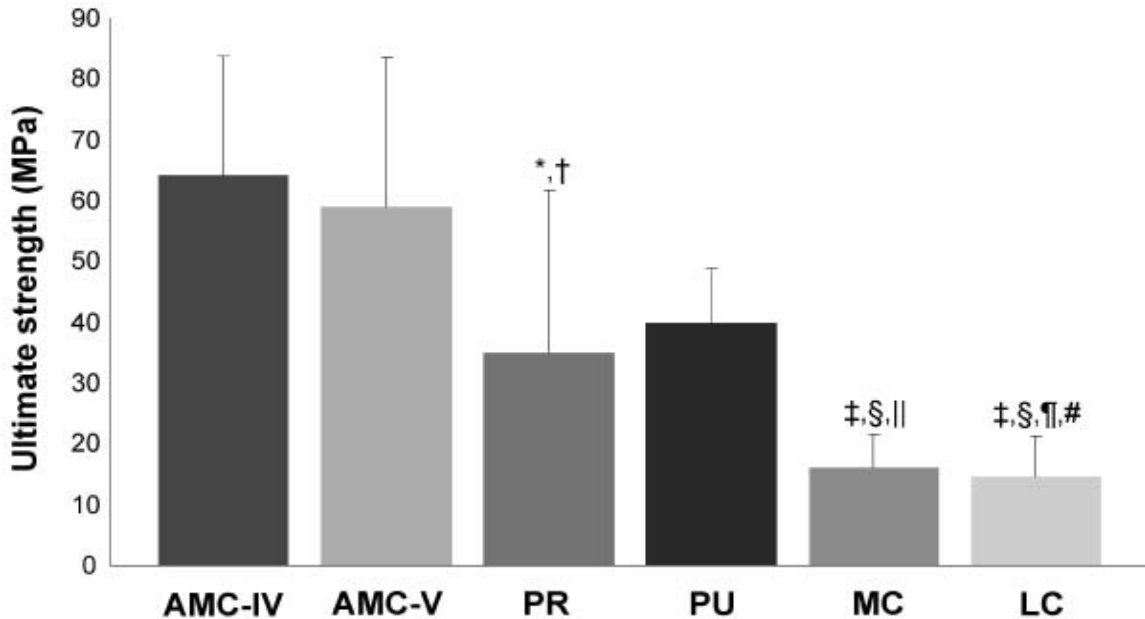


Figure 15-Mean  $\pm$  SD ultimate strength for each of the 6 canine ligaments ( $n = 8$  specimens/ligament) evaluated. Values for elastic modulus differ significantly ( $p < 0.001$ ) among the 3 ligament groups. \*Value differs significantly ( $p = 0.004$ ) from the value for the AMC-IV ligament. †Value differs significantly ( $p = 0.012$ ) from the value for the AMC-V ligament. ‡Value differs significantly ( $p < 0.001$ ) from the value for the AMC-IV ligament. §Value differs significantly ( $p < 0.001$ ) from the value for the AMC-V ligament. || Value differs significantly ( $p = 0.024$ ) from the value for the PR ligament. ¶Value differs significantly ( $p = 0.044$ ) from the value for the PR ligament. #Value differs significantly ( $p = 0.003$ ) from the value for the PU ligament. See Figure 4 for remainder of key.

The mean failure load for the AMC-IV ligament differed significantly, compared with the mean failure load for the PR ( $p < 0.001$ ) and LC ( $p = 0.013$ ) ligaments. The AMC-V ligament had the highest mean failure load ( $602.54 \pm 165.22$  N) and differed significantly ( $p = 0.005$  or greater for all comparisons) from mean values for all other ligaments. Mean failure load did not differ significantly ( $p = 0.169$ ) between the LC ( $233.11 \pm 144.86$  N) and PR ( $149.27 \pm 68.61$  N) ligaments. The PR ligament had the lowest mean failure load of all the ligaments tested. Failure modes for each ligament are summarized in Table 1. The highest number of midsubstance failures was found for the MC and the PU ligaments, with 7 of 8 specimens failing at the midsubstance for both of these ligaments. The LC and PR ligaments each had midligament failure in 5 of 8 specimens, with the remaining failures occurring via bony avulsions. Six of 8 specimens of the AMC-V ligament failed at the bone-ligament interface. The AMC-IV ligament

had 3 specimens with midligament failure, 3 with bony avulsions, and 2 with failure at the bone-ligament interface.

Data on ultimate strength of the 6 ligaments were calculated [Figure 15]. Statistical analysis of the ultimate strength data yielded results similar to those for the elastic modulus. Specifically, significant differences were detected among the 3 ligament groups. However, ultimate strength did not differ significantly between the AMC-IV and AMC-V ligaments ( $p = 0.533$ ), between the MC and LC ligaments ( $p = 0.892$ ), or between the PR and PU ligaments ( $p = 0.197$ ). Mean cross-sectional area was also determined for each ligament. The MC ligament had the highest mean  $\pm$  SD cross-sectional area ( $26.68 \pm 11.34 \text{ mm}^2$ ); this value was significantly ( $p = 0.029$  or greater for all comparisons) higher as compared with the values for the other ligaments. Mean  $\pm$  cross-sectional area of the LC ligament ( $17.93 \pm 11.01 \text{ mm}^2$ ) differed significantly, compared with the area for the PR ( $6.75 \pm 4.77 \text{ mm}^2$ ) and AMC-IV ( $6.96 \pm 1.98 \text{ mm}^2$ ) ligaments, but did not differ significantly, compared with the area for the PU ( $10.82 \pm 2.65 \text{ mm}^2$ ) and AMC-V ( $12.29 \pm 8.72 \text{ mm}^2$ ) ligaments. Mean cross-sectional area did not differ significantly among the PR, PU, AMC-IV, and AMC-V ligaments.

### **3.4 Discussion**

To our knowledge, the study reported here is the first in which mechanical properties of canine carpal ligaments have been described. Computational methods, such as finite element analysis, require accurate representation of soft tissues (including the ligaments) to reproduce the physiologic function of the joint or joints evaluated. Hence, we evaluated the mechanical properties of canine carpal ligaments for use in a finite element model of the canine antebrachium in this study. The AMC ligaments function to prevent hyperextension of the middle carpal joint [91]. In the study reported here, we found that they have relatively higher values for elastic modulus, compared with values for the elastic modulus of the other ligaments

evaluated in this study, which may correspond to their function and the forces they are subjected to in normal carpal extension. The PR and PU ligaments are intra-articular structures and restrict cranial and caudal instability. It has been postulated [12] that the PU ligament is one of the principal stabilizers of the canine antebrachiocarpal joint and prevents caudal translocation. Values for the elastic modulus of these ligaments were found to be significantly ( $P < 0.001$ ) higher than those of the MC and LC ligaments. The MC ligament restricts valgus deviation, and the LC ligament prevents varus deviation [12]. These are primarily supportive ligaments and had the lowest values for elastic modulus of all the ligaments tested. The stiffness coefficients for all ligaments, excluding the AMC-V ligament, were not significantly different, which indicated that stiffness cannot be correlated with corresponding physiologic function of the ligaments. Specifically, the inherent material properties of the tissue, rather than apparent structural properties, appear to mimic the functionality of these ligaments.

This study had certain limitations. The strain data were obtained from the displacement measurements of the MTS. Given the small size of these ligaments, it was not possible to obtain the instantaneous strain by use of stereophotogrammetry, which would have provided a more resolute strain measurement. Another common method for gripping soft tissue involves the use of cryogenic fixation via clamps. However, because of the small size of these ligaments, use of cryoclamps was not a viable option. Gauge lengths were approximately 15 mm for the MC, LC, and PR ligaments and approximately 25 mm for the PU and AMC-V ligaments. Cryoclamps would introduce major temperature gradients across the midsubstance of these ligaments and cause considerable changes in the mechanical properties. The modes of failure indicated that of the 48 specimens tested, 28 (58.3%) failed at midsubstance, 11 (22.9%) had avulsion failure, and 9 (18.8%) failed at the bone-ligament interface. Most of the failures at the bone-ligament

interface were for the AMC-V ligament. This may have been attributable to technical difficulties encountered in aligning this ligament along its anatomic (tensile) axis. The high SD for the elastic modulus of the PR ligament could have been attributable to the fact that its cross-sectional area was too small to be measured with an area micrometer. Handheld Vernier calipers were used to determine the geometric area of these ligaments, which could have induced errors in measurement. Other important soft tissue structures in the canine antebrachium aid in the stability of the joint, such as the palmar fibrocartilage and the flexor retinaculum. Harvesting intact specimens of these structures is inherently challenging; therefore, they were not included in this study. The triangular fibrocartilage and the interosseous ligament, which provide important stabilization of the antebrachial region should be evaluated for their mechanical properties. Analysis of the results obtained indicated a strong relationship between ligament function and elastic modulus. Because the stiffness coefficient does not take into account the geometry of a specimen, a relation between ligament function and stiffness cannot be expected. Such differences in the mechanical properties among ligaments would result in substantial improvements in the accuracy of a canine antebrachium finite element model. A finite element model will have applications in optimizing the design of endoprosthetic implants for limb salvage after resection of primary osteosarcoma of the distal portion of the radius. It can also be used when designing focused experiments to assess modifications to surgical techniques. There are conflicting opinions on the role of preservation or resection of the distal portion of the ulna in stability of the carpal region after limb-salvage surgery and use of an endoprosthesis or allograft, as determined on the basis of biomechanical and clinical evaluation. The closest oncologic margin in many dogs with osteosarcoma of the distal portion of the radius is at the radioulnar articulation; hence, resection of the distal portion of the ulna is preferable from a surgical perspective because a wide surgical margin can be obtained. The distal portion of the

ulna provides an insertion site for the LC, radioulnar, and PU ligaments. It also articulates with the distal portion of the radius, accessory carpal bone, and ulnar carpal bone. There is a nearly equal distribution of axial load at the proximal ends of the radius and ulna [4]. Hence, from a biomechanical standpoint, the ulna appears to play a major role in load transmission. The importance of the ulna after limb-salvage surgery can be assessed by use of a finite element model of the antebrachium.

A total of 48 specimens of canine carpal ligaments were tested to obtain material properties, such as stiffness and elastic modulus, for use in development of a finite element model of the canine carpal joint. Quasi-static tensile tests were performed, and analysis of the results obtained indicated a strong function-elastic modulus relationship in the 6 ligaments evaluated. Future studies should evaluate the microstructure-function relationship by measuring total collagen content or determining the diameter of collagen fibrils by use of established protocols.

## 4 Model Development

In order to evaluate the current endoprosthesis and facilitate novel designs for canine limb-sparing, a finite element model of the canine antebrachium was developed using computed tomography data.

### 4.1 Model Generation

#### 4.1.1 Geometry

##### 4.1.1.1 Bony Geometry

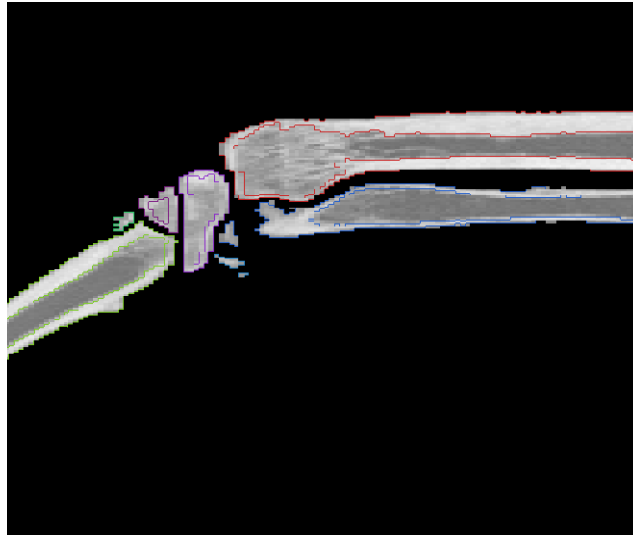
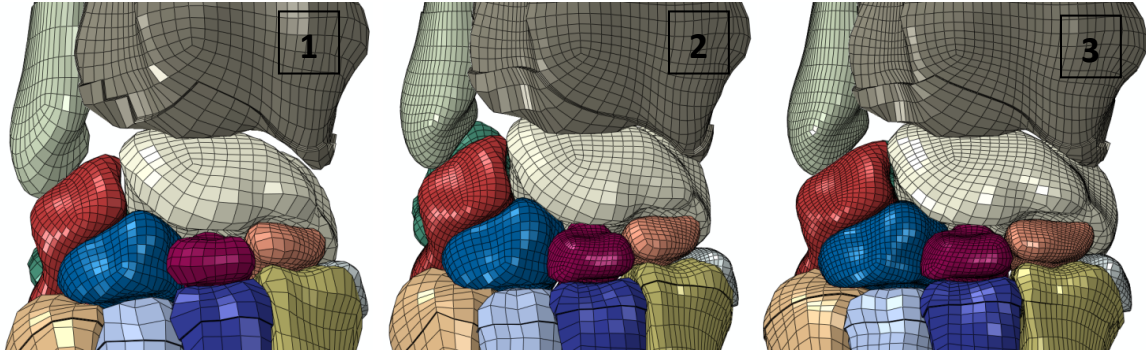


Figure 16-Segmentation of cortical bone in AMIRA.

The bony geometry for the canine forelimb finite element model was based on cadaveric CT image data. To this end, qCT images of the forelimb of a 38Kg Chesapeake Bay retriever were obtained. The forelimb was scanned at 1.0mm longitudinal resolution with 0.5mmx0.5mm transverse (in-plane) resolution. The images were then imported into a commercial medical image segmentation software (AMIRA Visage Imaging, Inc., San Diego, CA) [Figure 16].

Owing to the complicated geometry and contact surfaces present in the phalangeal region of the canine forelimb the model was limited to the antebrachial, carpal and the metacarpal regions. Furthermore, the first metacarpal bone, which provides no significant contribution to



**Figure 17-Three models of the canine forelimb with increasing mesh resolutions. 1) 150785 elements 2) 288735 elements 3) 432161 elements.**

the biomechanical stability of the carpo-metacarpal joint was excluded. In the end, the model consisted of thirteen bones (radius, ulna, seven carpal bones and four metacarpal bones). The exterior cortical shell for all bones was segmented by querying the Hounsfield unit (HU) attenuation values. A minimum thickness of two voxels was imposed for the cortical shell at all metaphyseal regions of long bones in order to reduce future computational complications. All voxels on the exterior with intensity values greater than 1000HU were deemed cortical bone. Since there exists overlap of intensity values between cancellous and trabecular bone, completely automated thresholding of cortical bone could not be performed. The threshold values for cortical bone ranged between 530-2109 HU. The remaining voxels within the metaphyseal regions of long bones were labeled as trabecular bone. The diaphyseal regions of long bones were left empty due to the absence of cancellous bone in these marrow regions. Owing to the difficulties of separating out trabecular bone in the small carpal bones, all voxels present were labeled as cortical bone. Initially, all bones were meshed with tetrahedral elements using the automated mesh generator in AMIRA. Each of these tetrahedral elements were then divided into four hexahedral elements using a custom-written program [Wes

Womack, OBRL]. However, the extremely skewed geometry of these elements was deemed to be detrimental for contact resolution. Hence, surface data in the form of STL Files from AMIRA were imported into TrueGRID (XYZ Scientific Applications, Inc., Livermore, CA), a hexahedral mesh generating software program. Care was taken to ensure optimal mesh resolution at all contacting surfaces. A total of three models of increasing mesh resolution were generated for the purposes of establishing convergence [Figure 17].

#### ***4.1.1.2 Articular cartilage***

Since no published data exists regarding the spatially varying thickness of articular cartilage in the canine carpal joint, cartilage was extruded as a three-element thick layer from all osteochondral surfaces with a constant thickness. The articular cartilage at the distal end of the radius was ascribed a thickness of 0.6mm. The cartilage on the radial carpal bone was assigned a thickness of 0.5 mm. All other cartilage was assigned a thickness of 0.2 mm. Care was taken to ensure no overlap of cartilage elements occurred between any articulating surfaces.

#### ***4.1.1.3 Ligaments***

Ligaments were modeled as one-dimensional, non-linear spring elements [Figure 18]. The origin and insertion points of all ligaments were determined by comparison to published anatomical data [3]. A custom MATLAB (The Mathworks Inc., Natick, MA) program ensured accurate placement of ligaments for all three models. After accurate positioning of all ligaments in the mid-resolution model the program recorded the three-dimensional positions of all ligament-insertion nodes and detected the closest corresponding nodes in the target model.

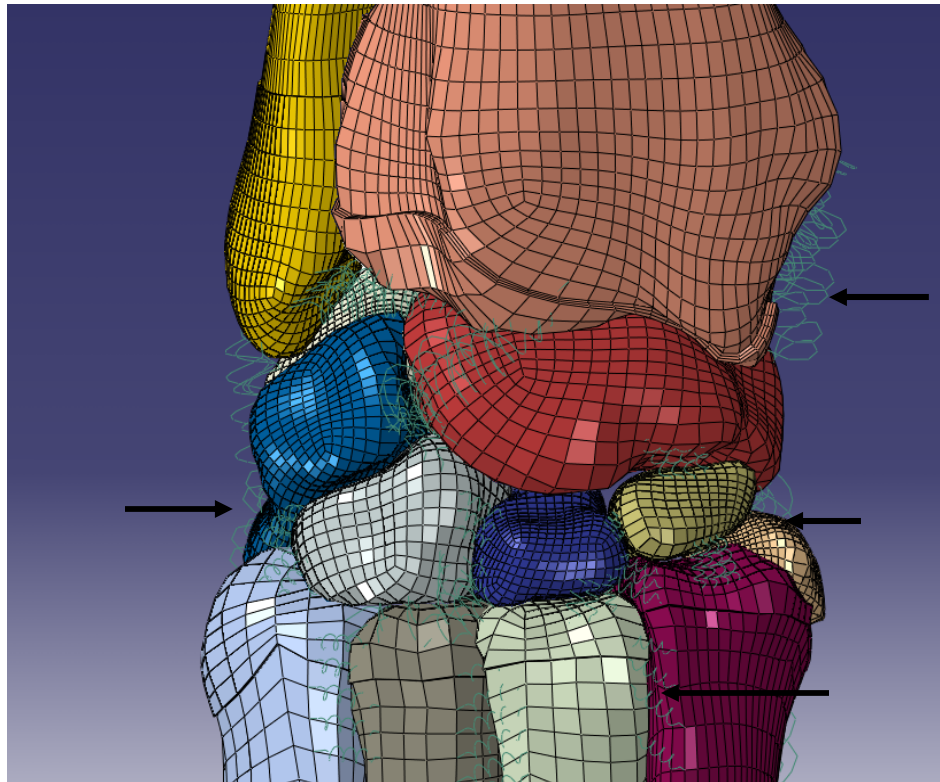


Figure 18-Ligaments represented as nonlinear one-dimensional spring elements (arrows).

## 4.1.2 Material Properties

### 4.1.2.1 Cortical and Trabecular Bone

Because the primary loading of all bones in the canine forelimb is in the axial direction both the cortical and trabecular bone were modeled as linearly elastic and isotropic [14]. The Young's modulus of cortical bone was set at 15GPa with a Poisson's ratio of 0.3. The Young's modulus of trabecular bone was set at 4000MPa with a Poisson's ratio of 0.3. Since all carpal bones had minimal amount of trabecular bone and the long bones had trabecular bone only in the metaphyseal region it was concluded that custom-designed trabecular bone properties using qCT attenuation values, would provide an insignificant, yet time-consuming, result on the model predictions.

#### 4.1.2.2 Articular Cartilage

Articular cartilage was modeled as a Mooney-Rivlin hyperelastic material [Figure 19]. The specific coefficients are provided in Table 2 where the  $C_{01}$  and  $C_{10}$  define the deviatoric response of the material and  $D$  defines the volumetric response of the material. The slope in the operating range of the nonlinear curve was approximated to be 15MPa. This value was based on the Young's modulus of human knee cartilage [35, 92] since no literature exists that has investigated the compressive mechanical properties of articular cartilage in the canine carpal joint. Considering the short time scales involved in the loading of cartilage within the carpal joint, a single phase representation was deemed appropriate [14].

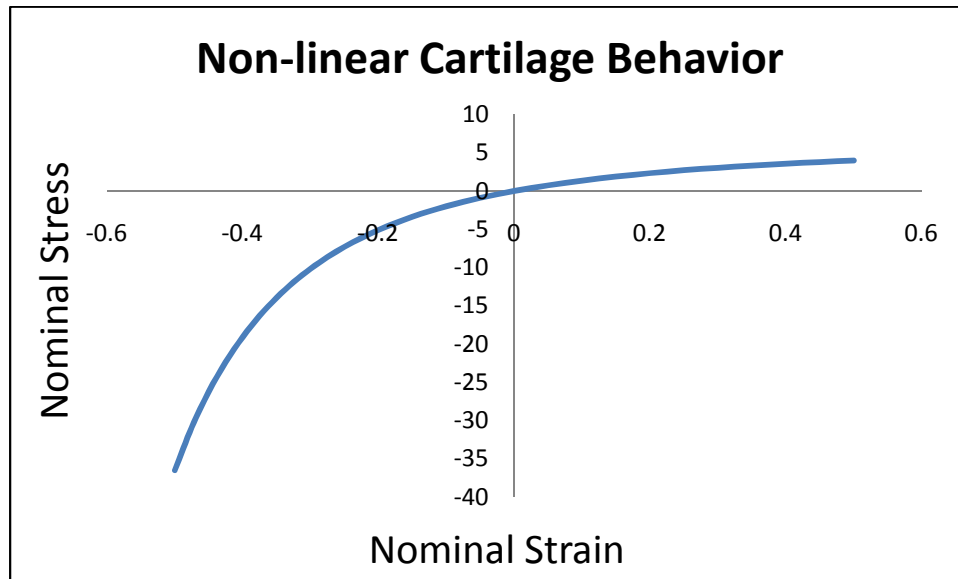


Figure 19-Nonlinear hyper elastic material behavior applied to all cartilage layers.

$C_{10}$	$C_{01}$	$D_1$
0.22MPa	2.5MPa	0.06

Table 2-Mooney-Rivlin coefficients for the hyperelastic cartilage behavior used in this model ( $D_1$  is unitless).

### 4.1.2.3 Ligaments

Force-displacement data is required to model ligaments as nonlinear springs in ABAQUS. For the six important stabilizing ligaments described, the data were obtained from uniaxial tensile tests. The toe region was also included in the force-displacement data for all six ligaments, and the ligaments were constrained to support no load under compression [Figure 20]. The remaining ligaments excluding the interosseous ligament were also modeled as nonlinear springs which did not support load under compression. The interosseous ligament was modeled as a linear spring with a high stiffness coefficient ( $k=100000\text{N/mm}$ ) to represent the extremely stiff nature of this ligament.

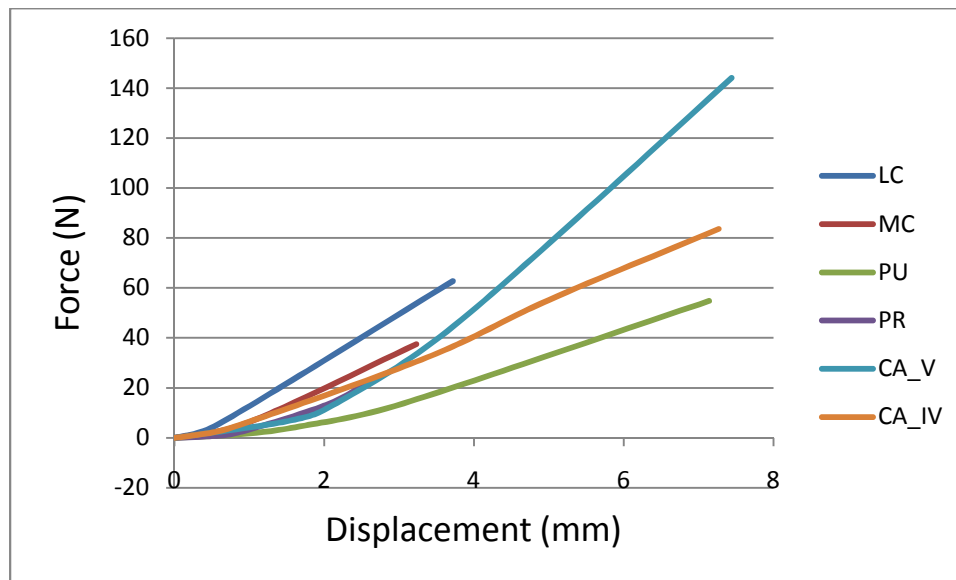


Figure 20-Non-linear force-displacements curves for the six primary carpal ligaments obtained from *in vitro* experiments.

### 4.1.2.4 Endoprosthesis

The spacer, DCP and cortical screws were made of stainless steel grade 316L. The Young's modulus was set at 193GPa and the Poisson's ratio was defined as 0.3 for all three parts.

## 4.2 Model Convergence

A total of three models with increasing mesh resolution were created using TrueGrid and ABAQUS. The total number of elements ranged from 150785 to 432161 and the total number of nodes ranged from 215320 to 589367 [

Figure 21]. Model convergence was examined throughout the complete load range. The parameters examined were bone strains (proximal [location 1], mid-diaphyseal [location 2] and distal [location 3] regions of the radius and the mid-diaphyseal region [location 4] of the ulna) [Figure 27], total area in contact within the radiocarpal joint and displacement of the radial carpal bone. The convergence data summary is provided in Figure 22 as a percentage difference as compared with the high resolution model and data over the full load range is provided in Figure 23, Figure 24, Figure 25 and Figure 26 for the medium and high resolution models. The convergence threshold was set at 10%.

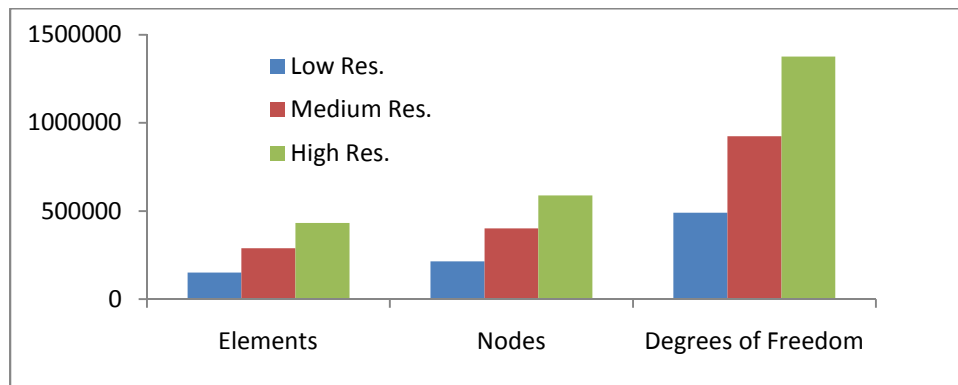


Figure 21-Convergence model parameters.

Mesh	Location 1 (Strain)		Location 2 (Strain)		Location 3 (Strain)		Location 4 (Strain)		Radial Carpal Bone		Strain Energy
	Maximum Principal	Minimum Principal	Contact Area	Displacement	Whole Model						
Mid	7.9%	12.66%	-5.18%	-6.94%	4.38%	11.55%	4.99%	3.5%	-0.712	-1.68%	7.05%

Figure 22-Convergence data summary. All values are presented as percentage difference compared to the high resolution model.

For the medium resolution model, all parameters were with the 10% threshold, except the minimum principal strain predictions at the distal and proximal regions of the radius. These locations were observed to have significant strain gradients. Owing to the coarse mesh of the low resolution model, contact convergence was difficult to achieve. Hence, the low resolution model was not included in this study.

Inter-model variability in the maximum principal strains for all four investigated locations was within 7.9%. The displacement of the radial carpal bone was within 1.68% and the total area in contact for the radiocarpal joint (radius and radial carpal bone) was within 0.72%. The total strain energy of the medium resolution model was within 7.05% of the high resolution model predictions. Based on the above presented convergence data, the medium resolution mesh was considered converged for the parameters being investigated.

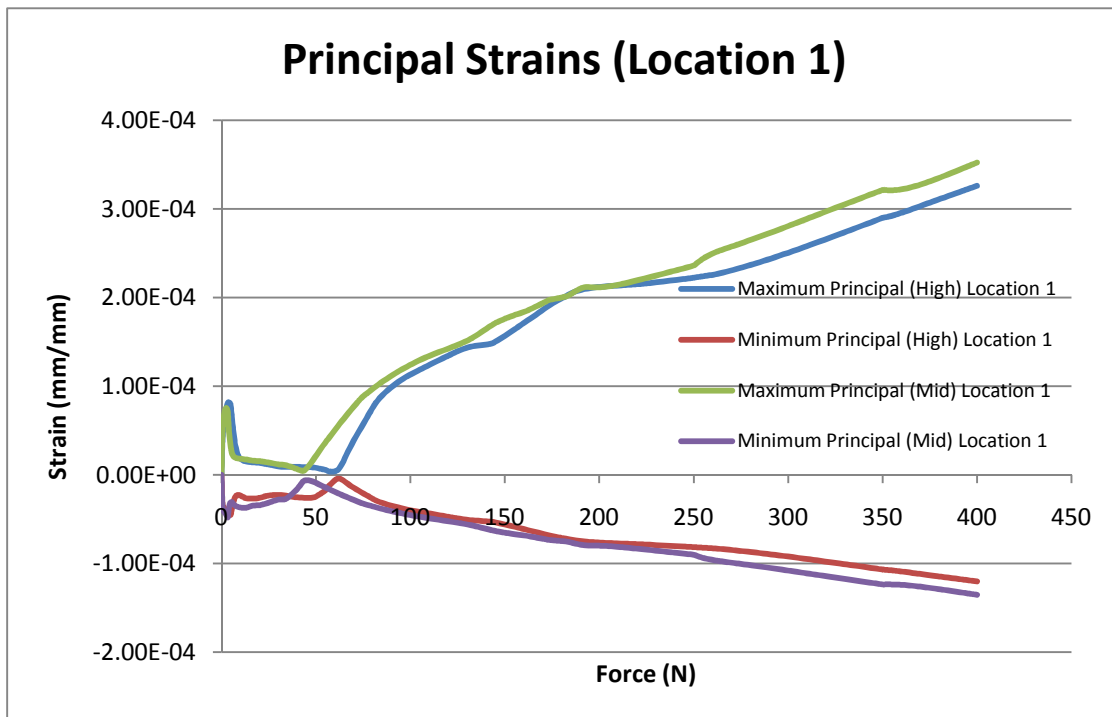


Figure 23-Principal strains at location 1.

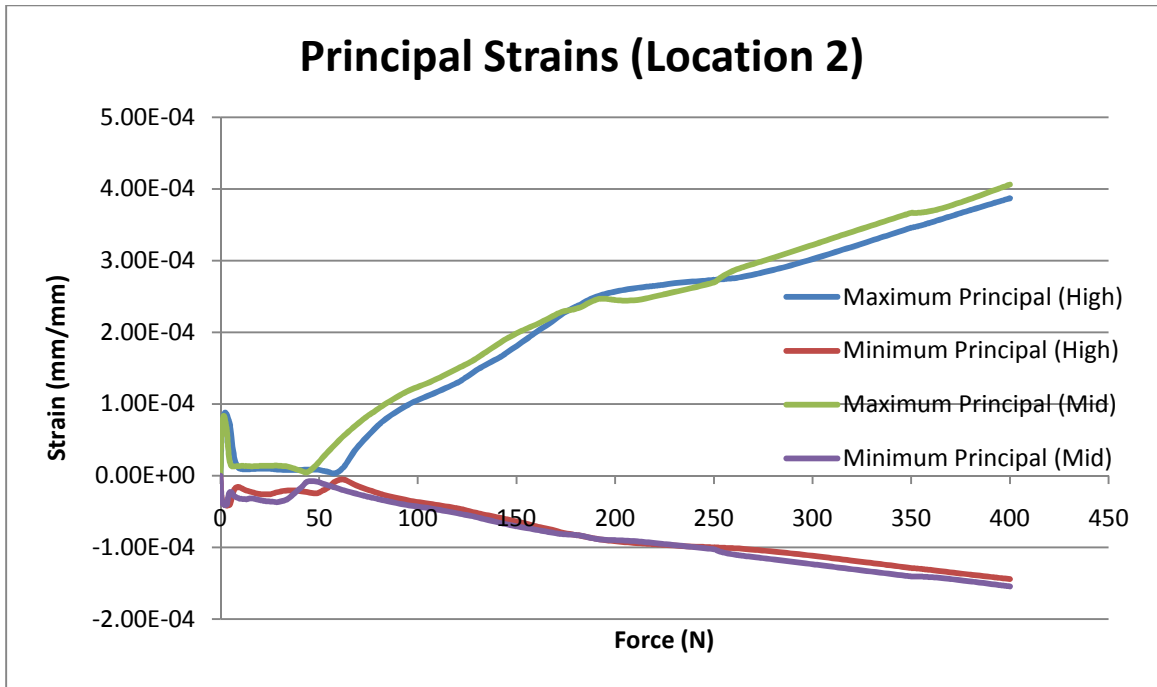


Figure 24-Principal strains at Location 2.

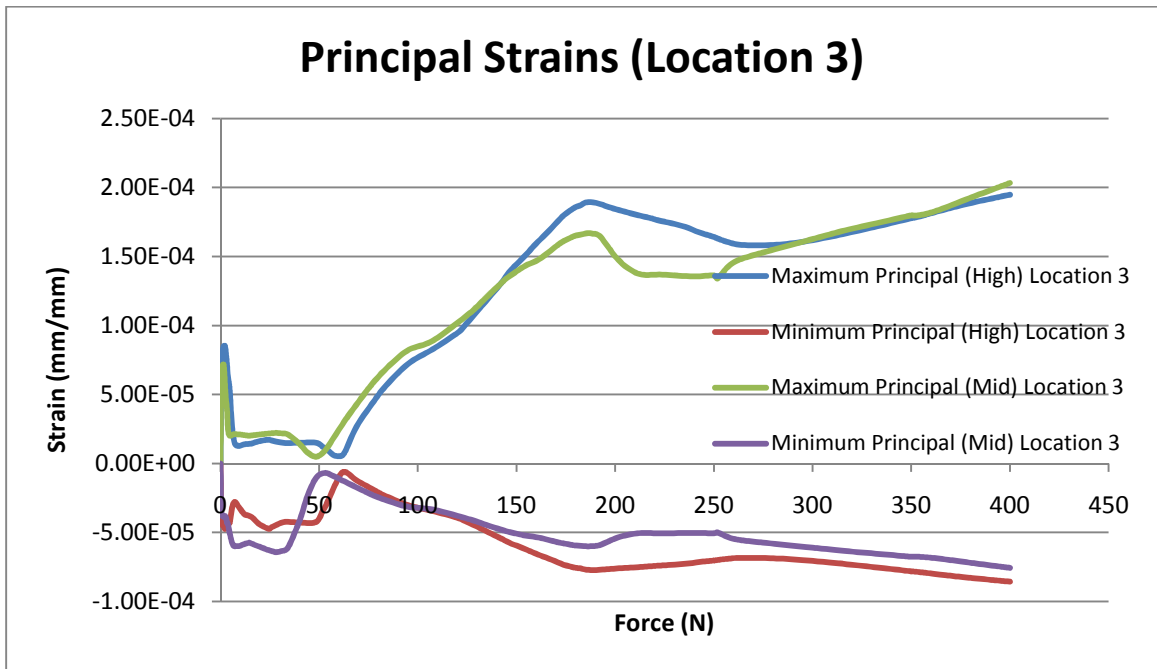


Figure 25-Principal strains at Location 3.

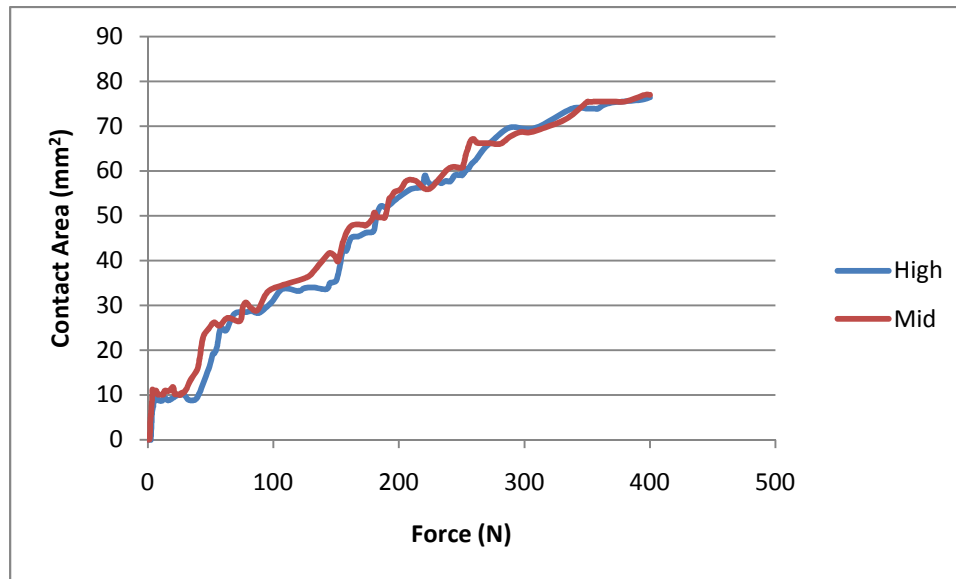


Figure 26-Total contact area for the radiocarpal joint.

## 4.3 Model Validation

### 4.3.1 Cadaver Experiments

Eight forelimbs were obtained from the Colorado State University's Veterinary Teaching Hospital for the purposes of model validation. All extraneous soft tissue was excised from the limbs. Care was taken to not damage any tendons which support load under extension. Care was also taken to not damage any ligaments present in the carpal joint. The cranial surfaces of both the radius and ulna were cleared of any soft tissue to attain a clean surface for strain gauge attachment. The strain gauges were used to measure surface strain at three locations (proximal, mid-diaphyseal, distal) on the radius [Figure 27] and the mid-diaphyseal region on the ulna [Figure 27]. The distal ends of metacarpals II-IV were potted in polymethylmethacrylate.

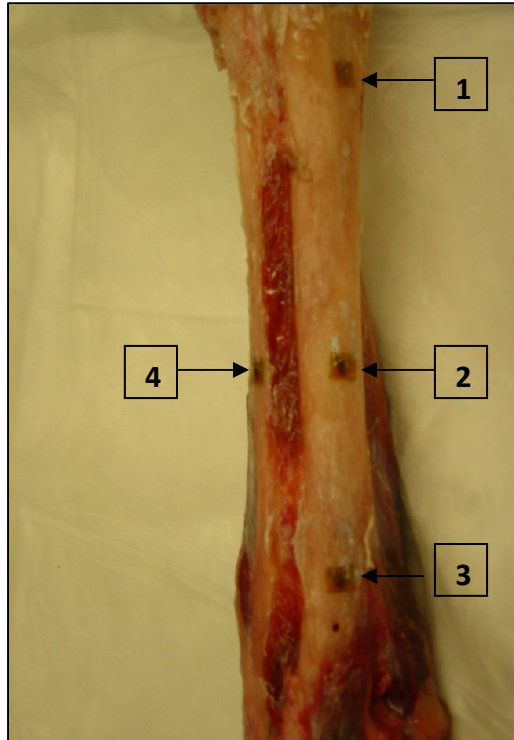


Figure 27-Location of strain gauge rosettes on the radius and ulna.

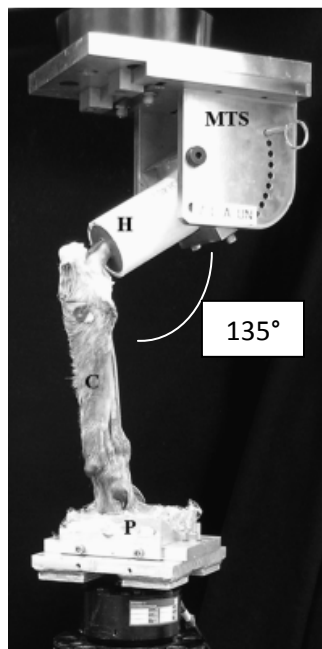


Figure 28-Construct for testing of canine forelimbs (H=Humerus, C=Radius, P=Bottom potting box).

The humerus was freed of any extraneous soft tissue and muscle attachments and was potted in a 2 inch diameter Poly Vinyl Chloride (PVC) pipe. The complete construct was fixed in a custom-designed apparatus for testing canine forelimbs [57] [Figure 28]. The angle between the antebrachial region and the humerus was set at 135 degrees with the aid of a goniometer. The angle between the metacarpal region and the antebrachial region was set at 10 degrees (from vertical) of extension [93]. Motion analysis marker triads were attached at the mid-diaphyseal region of the radius and the mid-diaphyseal region of the metacarpal-III bones to measure relative motion between the two regions. A single marker was attached to the caudal end of the radial carpal bone to measure its total displacement through the loading cycle. The limb was loaded to 110% BW, which is the load observed in the forelimb at trot [81]. A total of two loading regimes were established for each forelimb tested. The forelimb was first loaded with all extensor tendons intact. In the second regime all tendons supporting load under extension were resected. This was performed since the finite element model did not include any of these tendons. The specimen was hydrated with liberal saline spray at every 15 minute intervals. All data was collected at a frequency of 60Hz.

#### **4.3.2 Validation Results and Discussion**

Several studies have reported the development of finite element models of the human wrist joint [60, 62, 65, 68]. However, most of these studies fail to report any validation data which is a crucial step in the development of any finite element. It is generally agreed that complete validation of any biological finite element model is impossible. Specifically, the model must be validated for the parameters being investigated in order to establish confidence in the model's predictions.

The validation parameters investigated in this study were: bone surface strains and radial carpal bone motion.

The results comparing surface principal strains obtained from the validation experiments and the model can be seen in Figure 29. A 4x4 array of nodes were selected from the model in the approximate area where the experimental strain gauges were attached. The strain predictions for each of the 16 nodes were then averaged for comparison with the experimental results. The error bars for model predictions in Figure 29 represent the standard deviation of the 16 nodes probed from the model. All strain predictions fell within one standard deviation of the experimental strain results with the lone exception being strain gauge #3. Previous studies have measured *in vivo* strains at the mid-shaft of the radius. Turner et al. [94] investigated the high frequency components of bone strain for dogs at a walk. However, they report peak microstrain values for only a single dog. Coleman et al. [95] report *in vivo* strain values of 1000 microstrain at the mid-shaft of the radius. Again, this value is for a single dog. Both these studies do not provide strain values over a statistically significant canine population and hence the data cannot be directly compared to those obtained in this study. The distal radius cranial surface has a significant strain gradient and owing to the difficulties associated with finding the exact location of the strain gauges in the model the strain gauge 3 predictions did not fall within one standard deviation of the experimental results. It is to be noted that the experimental strain values were obtained from the excised tendons loading regime. These strain values tended to be lower as compared to the intact values indicating the significant contribution of tendons to bone strain.

Comparison of minimum principal strain predictions between the model and the experimental results is shown in Figure 30. The difference in maximum principal strain values between

loading the specimen in the intact condition as compared to all extensor tendon resection is shown in Figure 31.

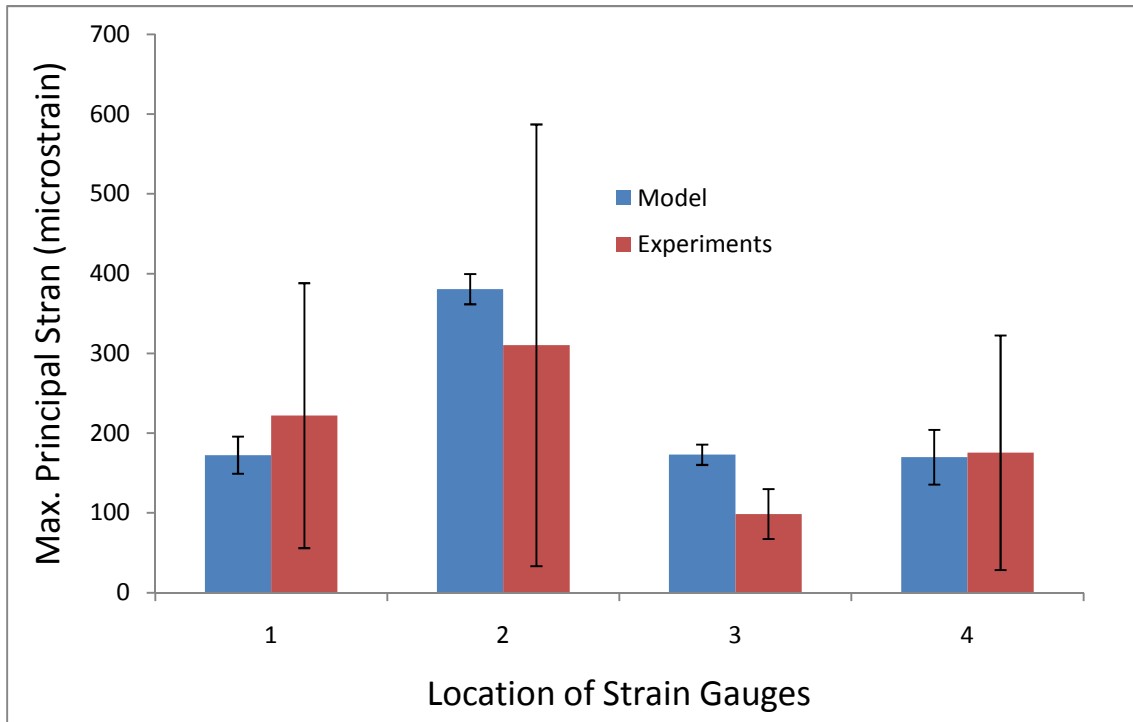


**Figure 29-Comparison of strain predictions from the model with values from the validation experiments.**

Interestingly, a decreasing trend in the values of maximum principal strains was observed for the strain gauges on the radius, while the maximum principal strain values increased at the mid-diaphysis of the ulna, indicating a biomechanical change in the joint after tendon resection.

The displacement of the radial carpal bone predicted by the model was within one standard deviation of the experimental results. The model predicted a displacement of 11.45mm and the average $\pm$ SD value obtained from the validation tests was 10.1 $\pm$ 1.55mm.

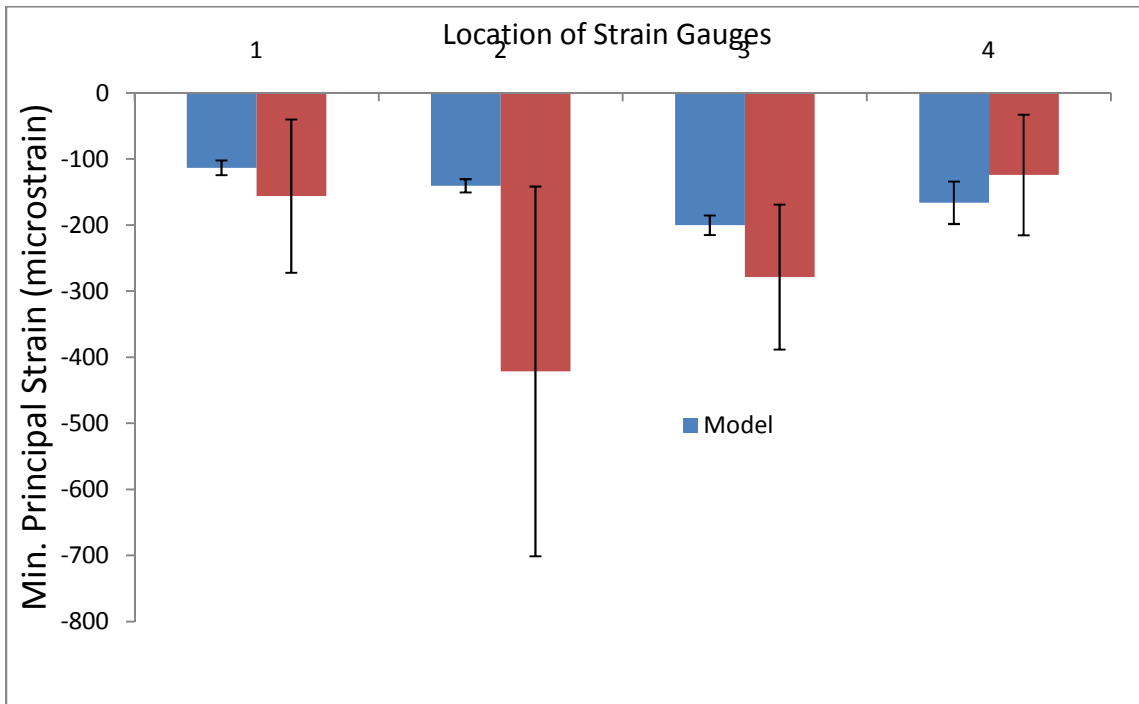


Figure 30-Comparison of minimum principal strain predictions from the model with values from the validation experiments.

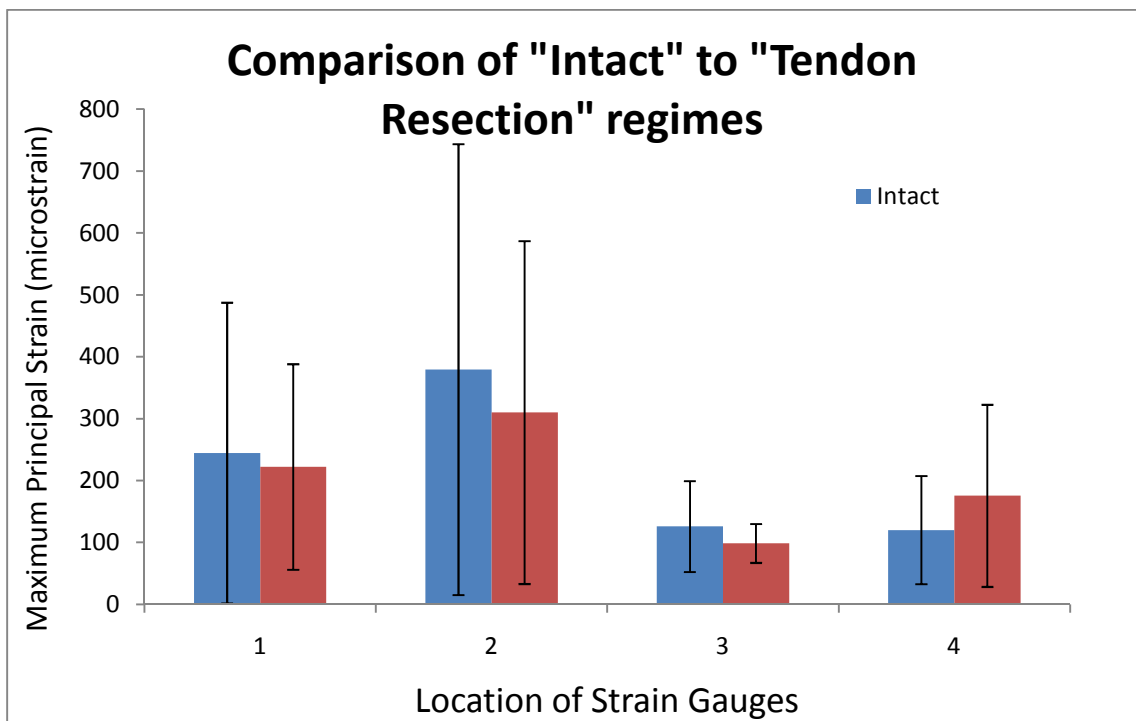


Figure 31-Comparison of maximum principal strains between the two loading regimes (Intact Vs. Tendon Resection).

## **5 Evaluation of Current Generation Endoprosthesis**

### **5.1 Introduction**

The design process for the current generation endoprosthesis skipped the crucial step of computational model evaluation. Biomechanical cadaveric testing is an important step in implant evaluation. However, it can only provide knowledge regarding the global failure mechanisms of the implant and cannot provide specific stress values and locations of high stresses which could be crucial in determining the efficacy and stability of the implant. Computational modeling is a very useful tool in comprehensively evaluating the proposed design before biomechanical testing is performed.

Results from the biomechanical cadaveric testing of the current generation endoprosthesis did not predict failure within the radial or metacarpal screws [57]. A quasi-static ramp to failure test predicted failure of the dynamic compression plate in most cases and metacarpal screw pullout in the rest. Based on the results obtained in the biomechanical study, the endoprosthesis was recommended for clinical trials. However, the effects of long-term cyclic loading on this implant were not investigated. The results for the clinical trials conducted with this current generation endoprosthesis yielded different results. In no cases was bending of the plate observed. Proximal radial screw pullout or complete shear failure was observed in all cases of construct failure indicating the mechanism of failure was fatigue loading as compared to trauma.

The mechanical underpinning of clinical failures observed with the implant could not be conclusively determined from the biomechanical testing results. Successful design of a new endoprosthesis could not be achieved without determining the exact structural causes for failure of the current generation endoprosthesis. To this end, the validated and converged model of the canine antebrachium was used in evaluating the current implant. The results obtained would be essential in the development of the new endoprosthesis.

## 5.2 Model Development

The geometry of the 2<sup>nd</sup> generation endoprosthesis was obtained from engineering drawings.



Figure 32-Endoprosthesis spacer.

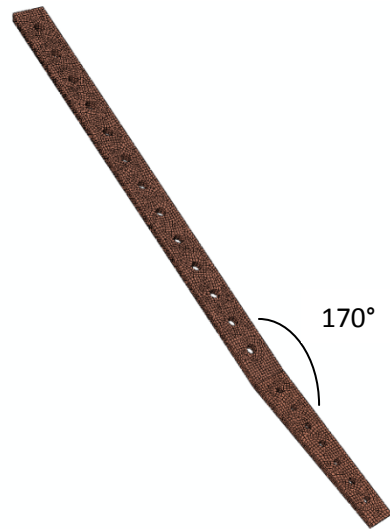


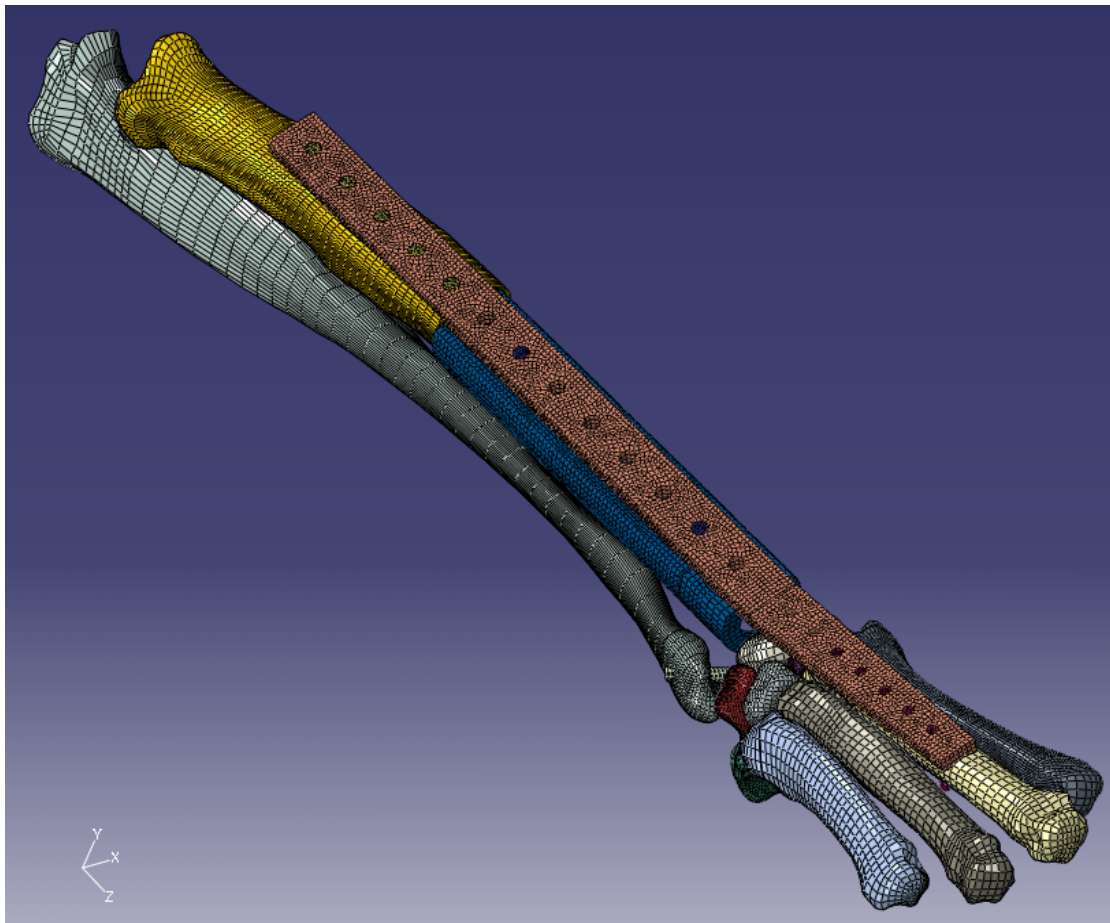
Figure 33-Dynamics Compression Plate (DCP).

Since no engineering drawings were available for the dynamic compression plate (DCP), the dimensions were obtained by the use of Vernier calipers. The normal angle between the antebrachial and metacarpal region when the dog is standing is 10 degrees (with respect to the vertical) in extension [93]. Hence, the DCP was implanted with a 10 degree angulation at the radiocarpal junction. Both the spacer [Figure 32] and the DCP [Figure 33] were modeled in ABAQUS and meshed with linear hexahedral elements.

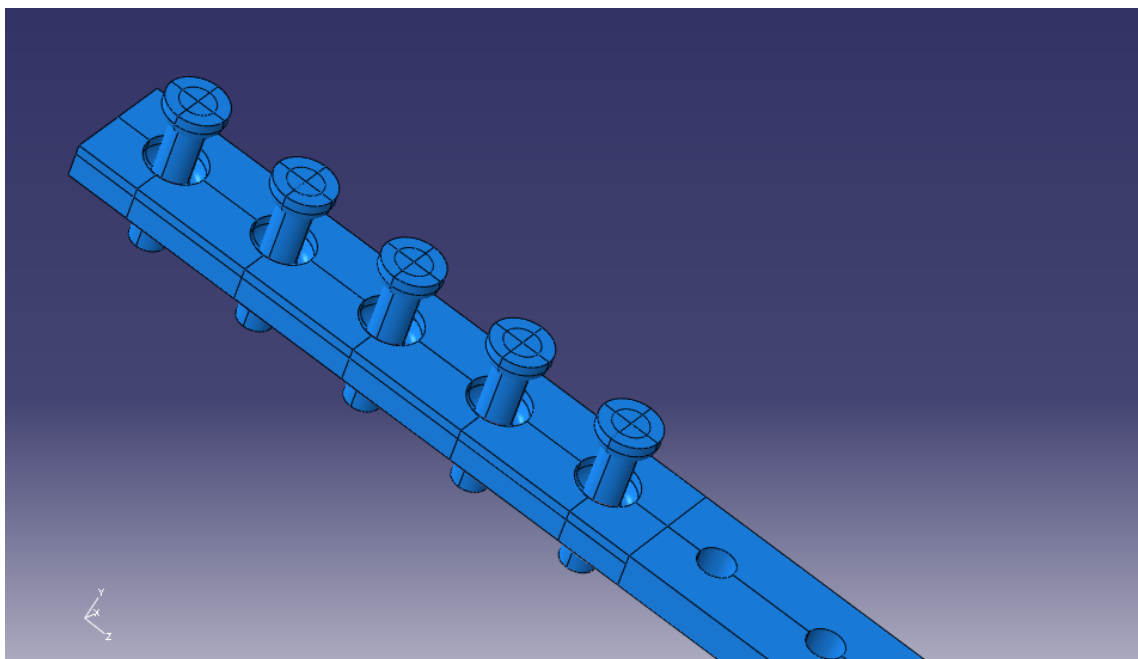


Figure 34-Radius with holes created in TrueGrid for insertion of proximal screws.

Three models of the spacer were developed for determining convergence. Potential areas of failure were investigated by evaluating the endoprosthesis spacer under a load of 400N in compression. The cortical screws were also modeled in ABAQUS. Since we were only interested in the global mechanical behavior of the endoprosthesis, threads on the cortical screws were not modeled. A typical surgical limb salvage protocol requires 50% of healthy bone (radius) to be present. Hence, the radius was resected by 50% from the distal end by deleting the corresponding elements. Screw holes in the radius were created using TrueGrid by deleting elements and projecting the ensuing element faces to a cylindrical surface with a radius of 3.5mm [Figure 34].



**Figure 35-Final model incorporating the current endoprosthesis construct.**



**Figure 36-Non-locking plate and screw design used for evaluating the current generation endoprosthesis. A coefficient of friction value of 0.25 was set between the plate and screw heads.**

The complete construct [Figure 35] was imported into ABAQUS and incorporated with the intact canine forelimb model. To simulate fusion of all carpal bones, the ligaments connecting these carpal bones were given a high spring stiffness coefficient ( $k=10,000\text{N/mm}$ ). The screw insertions in the metacarpal-III bone were simulated using tie constraints. To simulate complete union between the screws inserted in the proximal radius a friction coefficient of 0.99 was established between the two contacting surfaces. The friction coefficient between the screw heads and the non-locking plate was set at 0.25 [96] [Figure 36].

The effect of using a locking plate in place of the current non-locking plate was also investigated. A tie-constraint between the screw heads and plate simulated the locking mechanism. The effect of distal support to the endoprosthesis was also examined. Support at the distal end of the spacer was simulated with a tie constraint between the spacer and the proximal surface of the radial carpal bone.

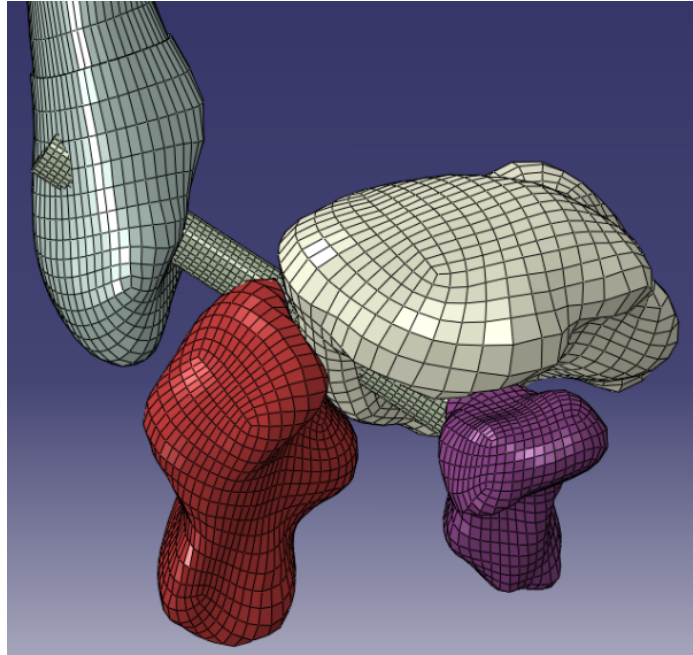


**Figure 37-An ulnar pin was inserted to evaluate the possible biomechanical contribution of the ulna.**

The effect of providing ulnar support was investigated by inserting a pin through the ulna and carpal bones [Figure 37]. All models were loaded to 110% BW in axial compression, which equated to 400N for a 38Kg dog.

### **5.3 Endoprosthesis Evaluation Results**

A maximum von Mises stress of 405.3MPa was predicted within the proximal radial screws for the model with a non-locking plate construct. Ignoring stress concentrations arising from point contact between the screw head and the dynamic compression plate, a maximum average stress of 210MPa was predicted at the third radial screw [Figure 38]. The maximum stress predicted in the radius bone was 559MPa [Figure 39]. The maximum von Mises stress prediction within the distal metacarpal screws was 128MPa [Figure 40] and within the 3<sup>rd</sup> metacarpal was 76MPa [Figure 41]. The maximum von Mises stress prediction within the screws connecting the metal endoprosthesis spacer to the dynamic compression plate was 340.7MPa [Figure 42]. The

endoprosthesis spacer reported a maximum von Mises stress of 124.1MPa [Figure 43]. The maximum von Mises stress within the dynamic compression plate was 126.2MPa [Figure 44].

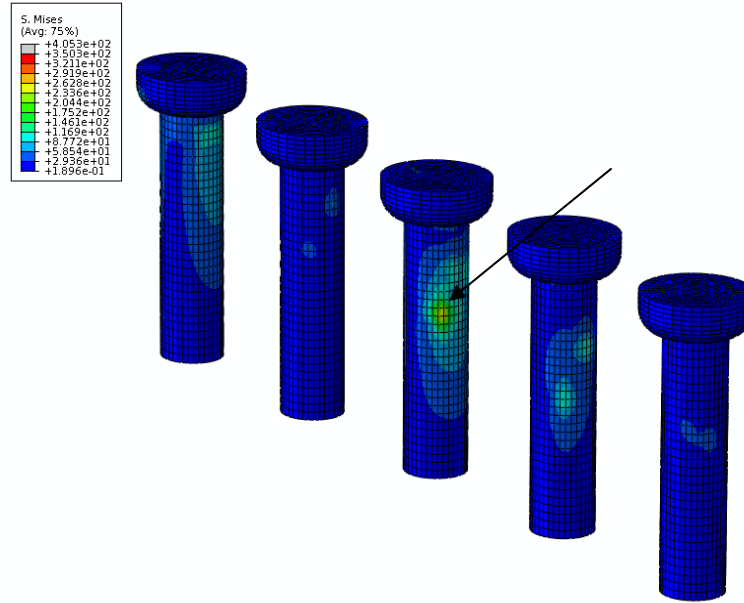


Figure 38-von Mises stress distribution within the proximal radial screws. Arrow indicates location of maximum stress (405.3MPa).

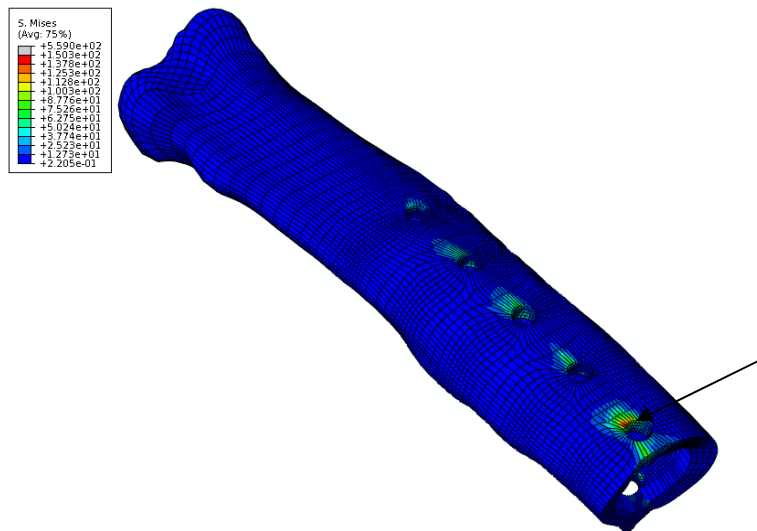


Figure 39-von Mises stress distribution within the radius. Arrow indicates location of maximum stress (559MPa).

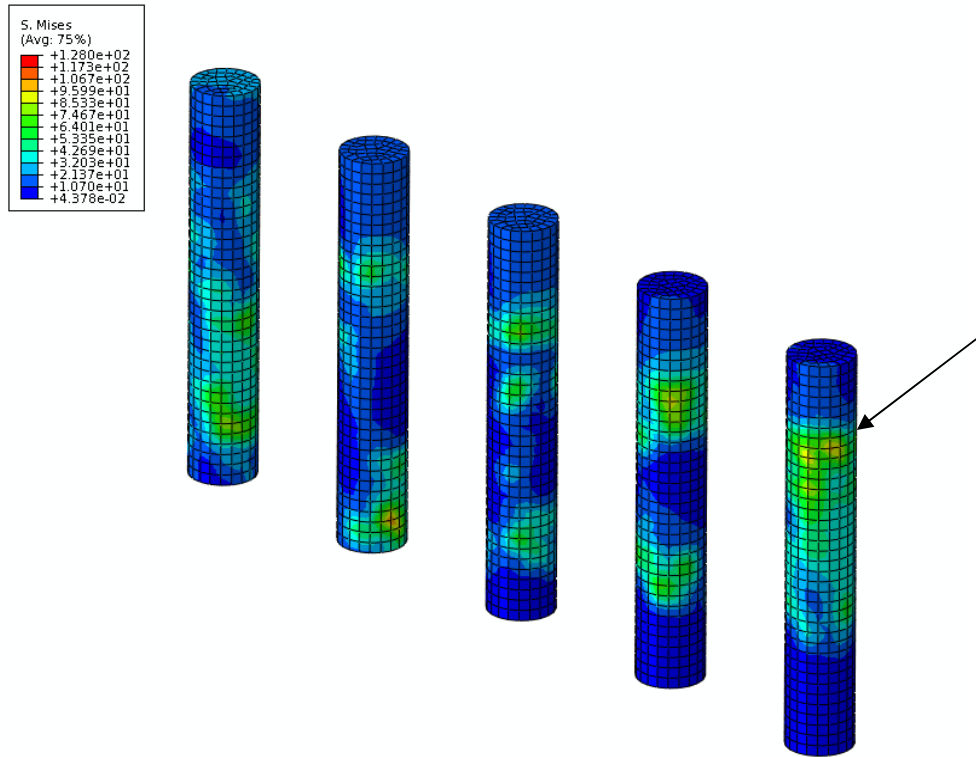


Figure 40-von Mises stress distribution within the distal metacarpal screws. Arrow indicates location of maximum stress (128MPa).

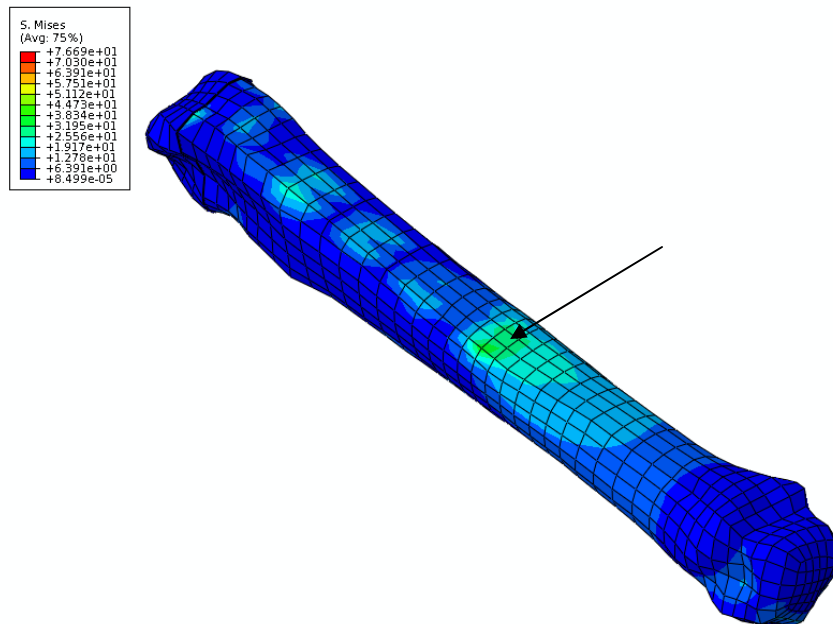


Figure 41-von Mises stress distribution within the 3rd metacarpal bone. Arrow indicates location of maximum stress (76MPa).

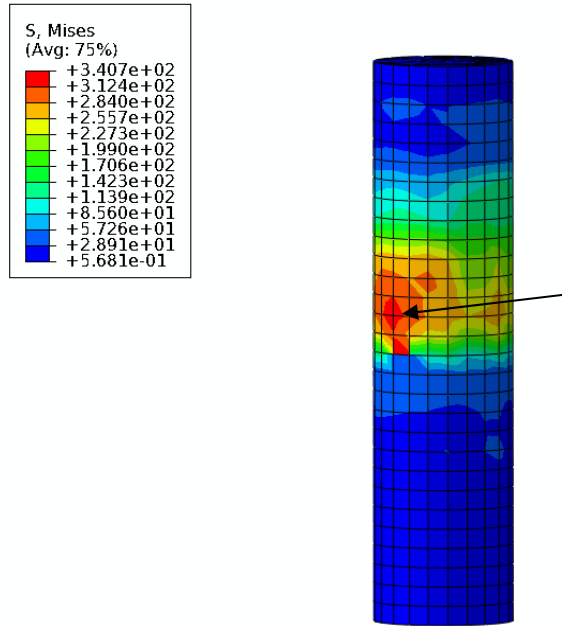


Figure 42-von Mises stress distribution within the endoprosthesis spacer screws. Arrow indicates location of maximum stress (340.7MPa).

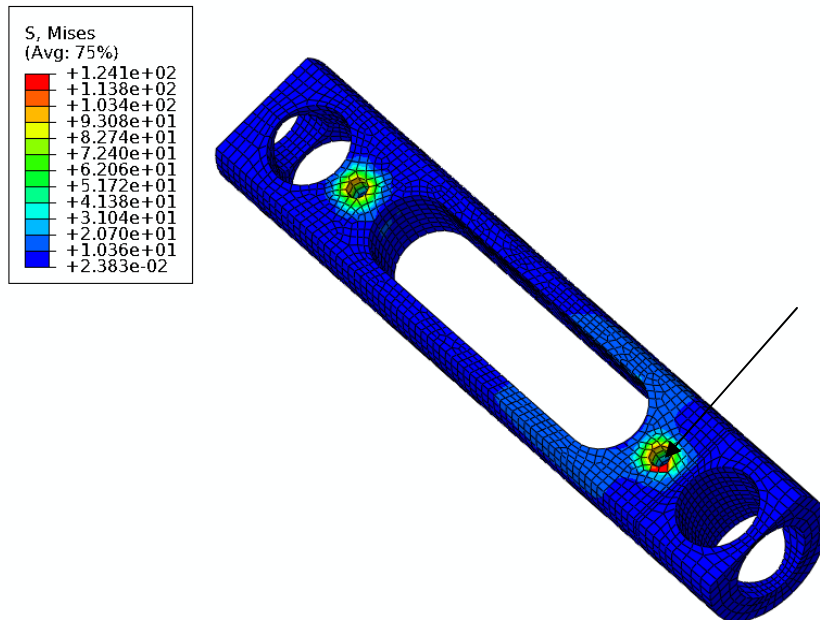
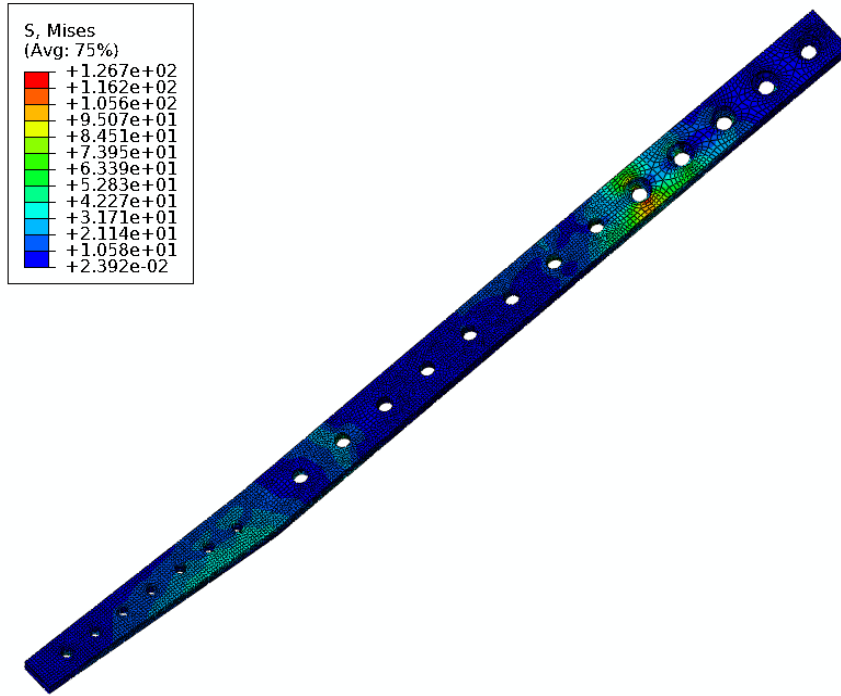


Figure 43-von Mises stress distribution within the endoprosthesis spacer. Arrow indicates location of maximum stress (124.2MPa).



**Figure 44-von Mises stress distribution within the dynamic compression plate.**

For the model with the locking plate construct the maximum von Mises stress predicted within the proximal radial screws decreased slightly to 397MPa as compared to the non-locking construct. The maximum stress within the radius remained similar (574MPa). The maximum stresses within the distal metacarpal screws decreased by 20MPa to a value of 109.7MPa as compared to the non-locking plate construct. Stresses within the spacer screws decreased to 299.9MPa (340MPa). The maximum stresses within the endoprosthesis spacer were predicted to be 114.4MPa. A comparison of maximum stress predictions between the locking and non-locking plate constructs is shown in Figure 45.

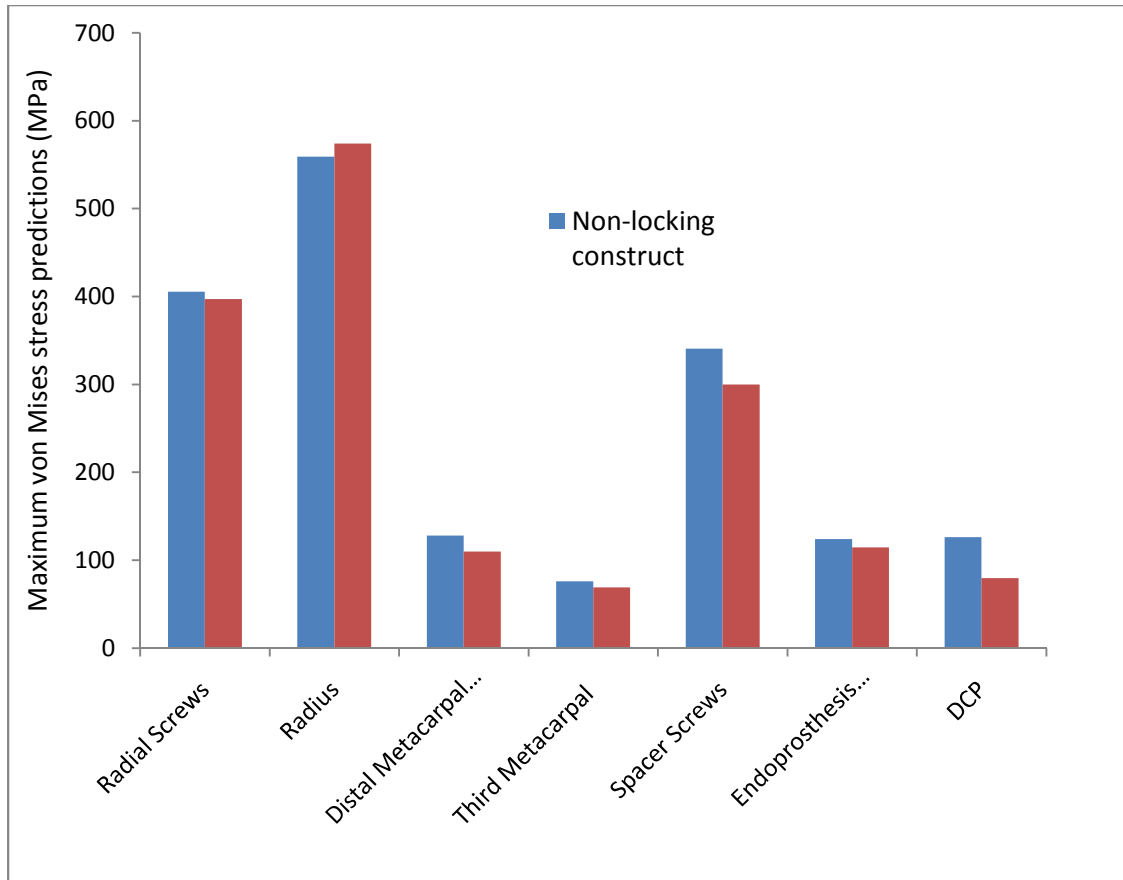


Figure 45-Comparison of von Mises stress predictions between the non-locking and locking constructs.

## 5.4 Discussion

High stresses (maximum von Mises stress = 559MPa) were observed at the bone-screw interface in the proximal radius. High bending stresses (maximum von Mises stress = 405 MPa) were also observed within the radial screws. Considering the fatigue limit of 316L stainless in the body environment is 200MPa for 10 million cycles [74] of loading the predicted stresses are too high for sustained performance of this endoprosthesis. Furthermore, the predicted maximum stresses are close to the reported yield stress of 316L stainless steel of 695MPa, which can be easily approached or exceeded under an impact loading scenario. The observed failure of the proximal screws in the clinical setting is congruent with the findings in this finite element study.

Due to the offset loading of the construct, bending of the DCP was also observed. A maximum displacement of 0.57mm was observed at the distal end of the radius.

The removal of distal support to the spacer tended to mitigate the stresses at the bone-screw interface (a decrease of 19%). However, the stresses within the screws remained unchanged indicating that ensuring support at the distal end of the prosthesis cannot guarantee the stability of the implant. The addition of distal ulnar support also greatly reduced the stresses at both of these locations. The stresses at the bone-screw interface were reduced by 28% while the stresses within the radial cortical screws were decreased by 26%. However, in many cases the ulna has to be necessarily resected to stem the propagation of metastasis. Hence, this solution cannot be recommended for the current generation implant. The use of a locking plate in place of the current non-locking plate did not induce a significant change in the stresses observed at the bone-screw interface (574MPa) or within the radial screws (404MPa). However, a greater dissipation of stress was observed in the proximal radius around the screw holes [

Figure 46]. This is consistent with the observed clinical effects with the use of a locking plate and constitutes a major rationale for recommending implantation of locking plate constructs for osteoporotic patients. The clinical study which evaluated the first generation endoprosthesis reported the major causes of failure were screw pullout and shear failure of the cortical screws. This prospective clinical study conducted by Liptak *et al.* [56] reported 40% failure rate for dogs (n=10) implanted with the first generation endoprosthesis. All implant failures were associated with screw loosening in the proximal radius. The most severe case had shear failure of all five proximal screws within the radius. The high stresses predicted by the model in the proximal radius bone-screw interface are congruent with the screw loosening observed clinically.

Furthermore, the high stresses predicted within the radial screws are in line with the shear failure of these screws observed in the clinical milieu.

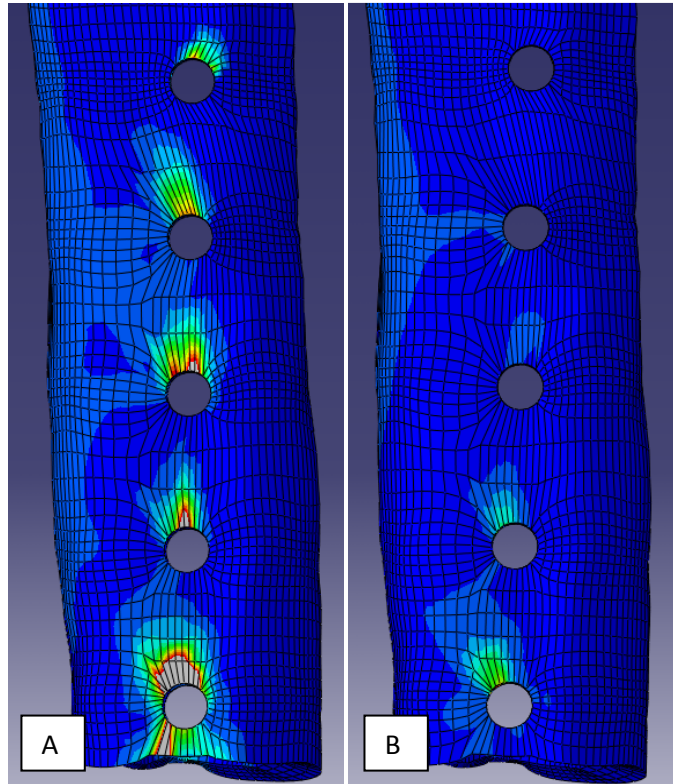


**Figure 46-Greater stress dissipation can be observed within the radius for the locking plate construct (B) as compared to the non-locking plate construct (A).**

## 6 Novel Endoprosthesis Design

### 6.1 Introduction

Novel design strategies of limb sparing prostheses for human osteosarcoma patients have been well documented. However, the design methodologies employed in the development of canine distal radius osteosarcoma limb sparing implants have not been widely reported. A particular second generation endoprosthesis design for canine limb sparing is based on the cortical allograft implant used by oncology surgeons at the Colorado State University Veterinary Teaching Hospital. The massive cortical allograft was replaced by a replica metal spacer attached to an identical dynamic compression plate. Unfortunately, a comprehensive and rigorous engineering-based design procedure was not employed during its development. The results from an extensive computational modeling-based evaluation of the 2<sup>nd</sup> generation endoprosthesis (Chapter 5) mirrored the unfavorable results observed clinically [56], thus emphasizing the need for an engineering-specific approach in the design of the next iteration of this limb-sparing endoprosthesis.

Diverse limb-sparing strategies have been employed in the treatment of distal radius osteosarcoma [97, 98], which deviate from the conventional compression plate and allograft/metal spacer approach [48, 56]. Séguin *et al.* [97] investigated the use of an ipsilateral vascularized ulnar transposition autograft for limb sparing in two dogs. Ehrhart *et al.* [98] have investigated the use of transverse ulnar bone transport distraction osteogenesis for limb-sparing, which inherently requires multiple daily distractions and an external ring fixator. Both techniques provide a viable alternative; however, these techniques also require a highly-skilled team of surgeons and involve complicated post-surgical procedures. Development of a metal endoprosthesis with efficient implementation schema can potentially reduce the costs

associated with expensive external fixator equipment, extensive clinician training and bone bank maintenance and inventory.

### **6.1.1 Locking Vs. Non-locking Plates**

Conventional non-locking plates rely on completely different biomechanical principles for fracture healing as compared to locking plates [99]. When loaded axially, non-locking plates create significant shear stresses at the plate-bone interface [99]. Resultantly, non-locking plates require 2000-3000N of compressive contact force with the underlying bone surface during implantation [100, 101]. This is achieved by applying 3.5-5Nm of insertion torque to each of the non-locking screws [99]. Due to these high compressive forces, one of the major drawbacks of non-locking plates is the loss of periosteal perfusion under the compression plate, which can lead to bone and periosteum necrosis and resorption. Clinically, radiolucency at the screw threads is commonly seen, with concomitant loosening of the screws and plate. Additionally, non-locking plates perform poorly when implanted in patients with osteoporotic bone [102] due to compromised screw purchase and their reliance on the shear forces generated between bone and screws for stability.

Locking plates provide a single beam construct (no motion between the individual components of the beam) when used for fracture fixation [99, 101]. It has been shown that a single-beam construct can provide four times more strength as compared to non-locking plate constructs [99]. Locking plates reduce the relevant shear stresses by placing compressive stresses at the screw-bone interface. This results in a stronger construct since bone can withstand more load under compression [101]. Thus, locking plates also perform better when used with osteoporotic bone [103]. Furthermore, periosteal perfusion is left unhindered since locking plates do not rely on frictional contact with the underlying bone to achieve stability. An intact periosteal blood

supply system is necessary for rapid bone healing and is proposed to play a role in the decreased incidence of infection seen with locking plate constructs [100].

Another major difference between the two plate designs is the mode of fracture healing. Conventional non-locking plate constructs are stiffer, which translates to greater interfragmentary stability (< 2% strain). The resulting healing pathway is commonly devoid of an endochondral ossification mechanism and intramembranous ossification of the fracture is the normal functional outcome. Locking plates are more flexible (< 10% strain) as compared to non-locking plates resulting in indirect bone healing including the formation of a callus [101, 104]. A comprehensive study of the locking compression plate by Stoffel *et al.* [105] recommends at least three screws on either side of the fracture site (in the present study, this would equate to the carpal joint space) for added rigidity. For gap sizes larger than 6mm, the placement of the innermost screws should be as close as possible to the fracture site (joint space).

### **6.1.2 Locking & Non-locking Screws**

Multiple options are available for cortical screws for use in conjunction with a locking compression plate (LCP). An LCP can accommodate both locking and non-locking screw designs. Multiple studies [102, 103, 106] have investigated the use of hybrid locked plating (non-locking and locking screws used together[107]) in lieu of conventional dynamic compression plate (DCP) (which employs only non-locking screws). A comprehensive fatigue analysis of non-locking cortical screws by Zand *et al.* [108] reported that failure occurred most commonly at the root of the thread in the interface between the plate and bone. This was observed with the current generation endoprosthesis, which used non-locking bicortical screws. The use of locked hybrid bicortical fixation increases the implant stability significantly as compared to an unlocked bicortical configuration under anteroposterior bending loads [106].

## 6.2 Preliminary Design Iterations (Methods and Preliminary Results)

For reducing the computational time involved in testing various design iterations, simplified models of idealized 3<sup>rd</sup> metacarpal and radius bones were created [Figure 47]. The initial proposed designs for the endoprosthesis are shown in Figure 48 & Figure 49.

The intramedullary stem approach in Design #1 attempted to remove the off-axis loading observed in the earlier endoprosthesis. An intramedullary stem theoretically provides a higher area in contact with the native bone, and thus, should be capable of supporting more load. The stem was designed to be fixed to the bone by the use of intramedullary nails similar to those used in tibial reconstructions.

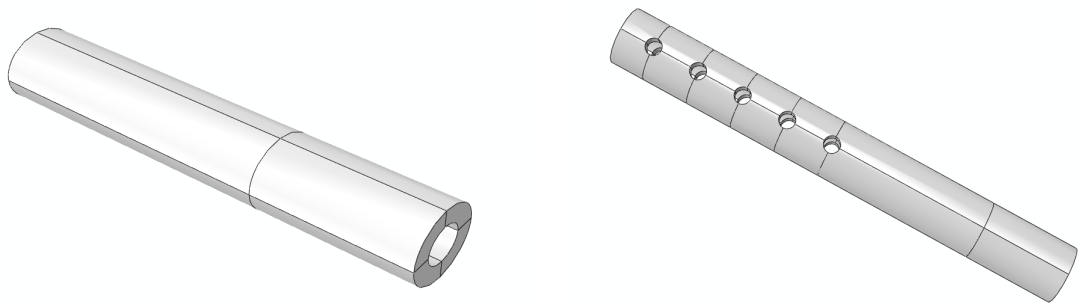


Figure 47-Idealized representations of the radius and 3rd metacarpal bones.

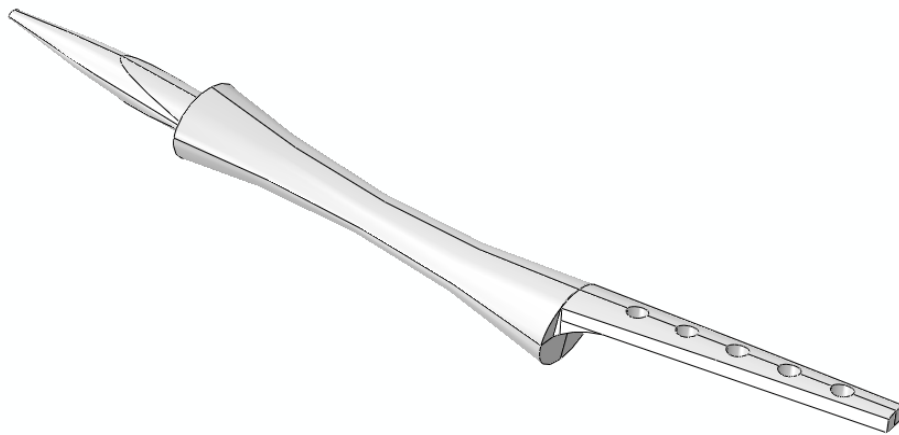
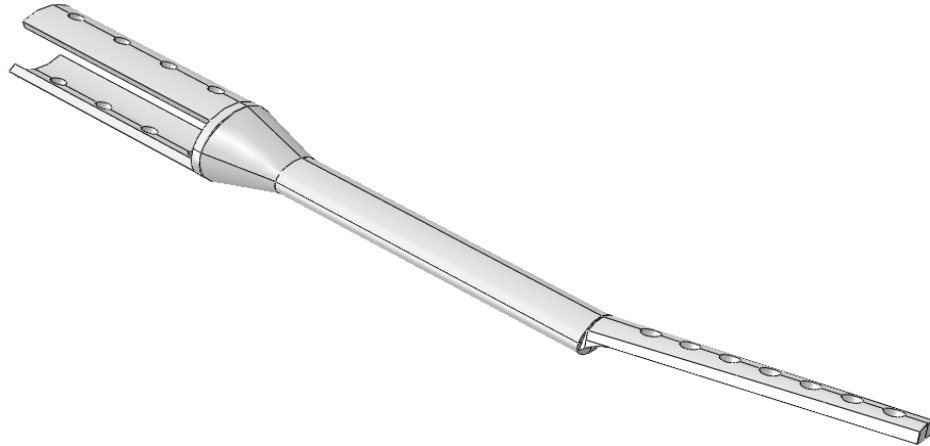


Figure 48-Proposed initial design 1 for the endoprosthesis.



**Figure 49-Proposed initial design 2 for the endoprosthesis.**

The collar approach (Design #2) attempted to reduce the load on the proximal radial screws by providing an additional plate on the opposing side. This was intended to eliminate the relatively high cantilever loading, as was observed in the earlier endoprosthesis design. The collar also eliminated excessive rotation of the radius and also provided support at the distal end of the radius.

Both these designs retained the plate feature at the distal end of the implant. This was justified by the low stresses observed in this region during evaluation of the current generation endoprosthesis. Furthermore, limited joint space in the carpo-metacarpal region was not conducive to major design changes in this area.

An investigative team consisting of Dr. Puttlitz, Dr. Stewart Ryan and Dr. Nicole Ehrhart was established for obtaining a combined engineering (Dr. Puttlitz) and clinical (Dr. Ryan & Dr. Ehrhart) perspective. The two proposed designs were presented to the investigative team. The issues noted by the team for design #1 were its inability to achieve consistent orientation with the radius and the lack of a modular design. Significant size variability of the radial intramedullary canal among the various dog breeds was also a concern. Design #2 shortcomings

were the lack of space between the radius and ulna for inserting the collar. Also, anticipated difficulties associated with accommodating breed size variation and the lack of a modular design were a concern. The following were requirements set by the surgeons on the investigative team:

1. Modular design
2. Ease of alignment between the proximal radius section and the carpus
3. Stress reduction within the radial screws

After recommendations from the VTH oncology surgeons, the next iteration merged the two concepts. This iteration is shown in Figure 50. It incorporated a modular design as required by the surgeons. The primary components consisted of three independent parts namely, the proximal endoprosthesis component (PEC), the mid-diaphyseal endoprosthesis component (MEC) and the distal endoprosthesis component (DEC).

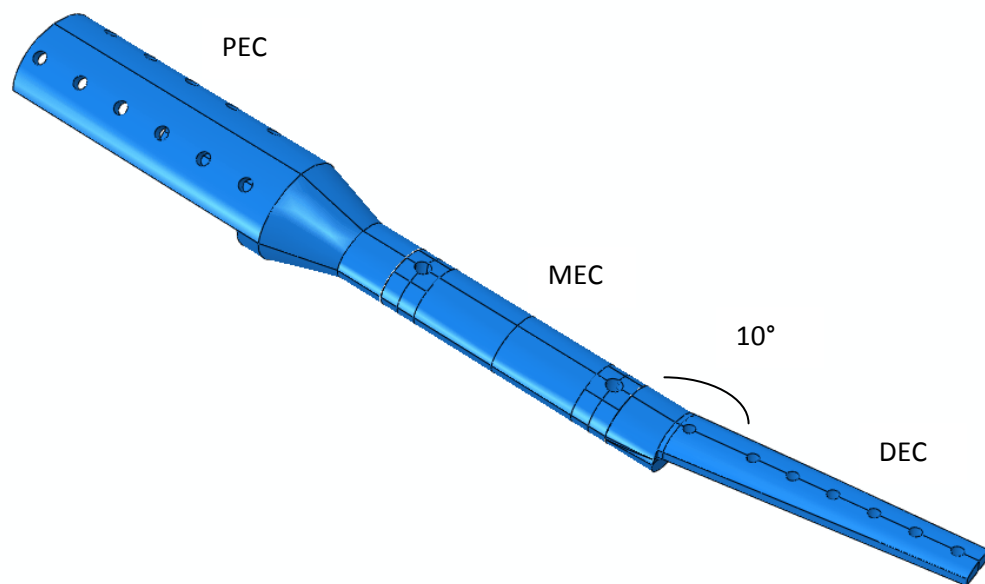


**Figure 50-First iteration based on requirements of the oncology surgeons.**

As can be seen in Figure 50, the distal endoprosthesis component (DEC) was designed with a 10 degree bend to mimic the physiological position of the canine radiocarpal joint at maximum extension. The DEC plate was designed with six distal locking screw holes (2.7 mm cortical screws) for fixation with the 3<sup>rd</sup> metacarpal and a proximal screw hole (3.5 mm cortical screw) for radial carpal bone fixation. The proximal endoprosthesis component (PEC) consisted of an intramedullary stem and a 180 degree wrap-around plate with locking screw holes at 45 degrees with respect to the sagittal plane of the radius. It also included a lip to provide added stability to the proximal end of the resected radius.

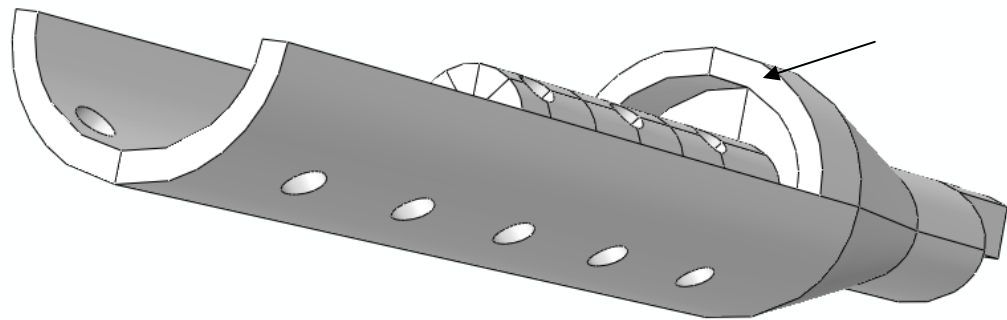


**Figure 51-Lip (arrow) provided at the distal end of the PEC for added stability of the distal end of the radius.**

The complete construct [Figure 52] was evaluated at a load of 1000N. All threaded interfaces were simulated by establishing contact with a coefficient of friction of 0.99 signifying complete union. The distal end of the 3<sup>rd</sup> metacarpal was fixed in place. The radial carpal screw was also inserted in place. It, however, did not provide any support to the construct other than alleviating stress concentrations at the plate-screw interface.

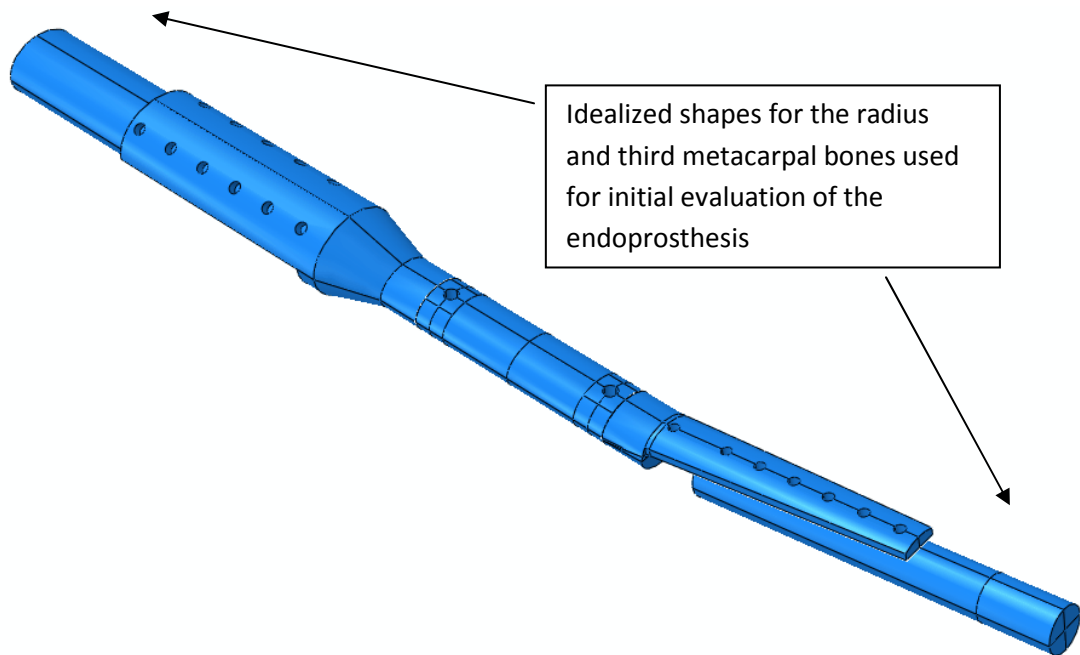


**Figure 52-Implant evaluated using the idealized bone constructs.**

Maximum von Mises stresses of 430MPa were observed within the metacarpal screws. The proposed design for the PEC was successful in eliminating high stresses within the proximal radial screws. The maximum stress observed within these screws was 83MPa (at 1000N of axial load). All other components reported peak stresses below 83MPa.

Based on these preliminary results, the proposed designs for the PEC and the mid-diaphyseal endoprosthesis component (MEC) were deemed acceptable for implantation in the intact forelimb model. It was observed that the 10 degree bend incorporated in the DEC was causing significant offset loading, resulting in unacceptably high bending stresses (430MPa) within the distal screws. A second model of the DEC with zero degrees of extension was created [Figure 53]. Evaluation of this model reduced the maximum stress prediction within the distal screws to 310MPa (at 1000 N), a value that is well under the reported yield strength of 316L (695MPa).

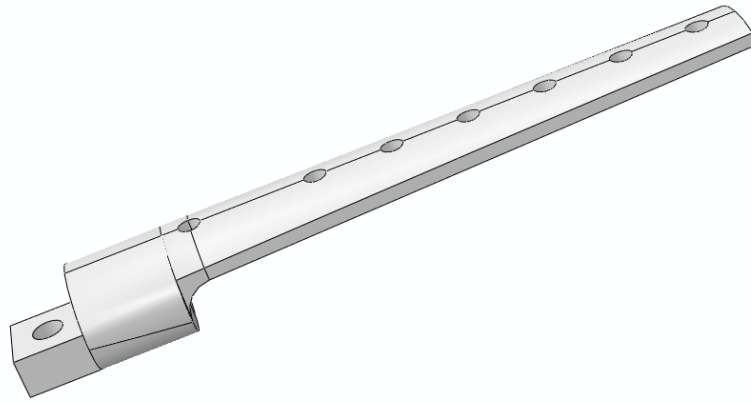


**Figure 53-DEC with a zero degree bend (Iteration 2).**

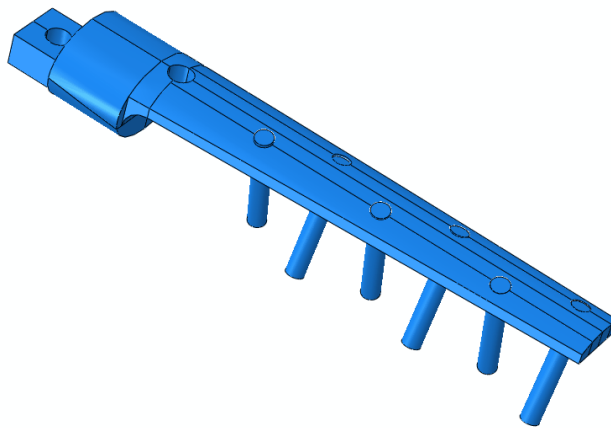


**Figure 54-DEC with screws at a 15 degree angle (Iteration 3).**

A third iteration of the DEC tried to incorporate the alternating and off-axis screw design implemented in the PEC [Figure 54]. It was hypothesized that placement of the screws outside of the loading axis could potentially lower the stress predictions within the screws. The screws were placed at 15 degrees with respect to the mid-sagittal plane [Figure 54]. Owing to the small dimensions of the 3<sup>rd</sup> metacarpal bone, a 45 degree offset (similar to the angle used for screw insertion in the PEC) was not clinically feasible from an implantation perspective. Additionally,

this design failed to further reduce the stresses within the distal metacarpal screws. Therefore, iteration 2 of the DEC was chosen for further analysis using the intact canine forelimb model.

## **6.3 Final Design Rationale and Evaluation**

### **6.3.1 Modular design**

It was determined that a modular design would facilitate continued development of the device and ease implantation of the endoprosthesis. Each module could be available in multiple sizes, which would accommodate the inherent variability of canine breed sizes. This modular aspect overcomes one of the main disadvantages of the older generation endoprosthesis, which was available in only two sizes, which did not encompass the diverse range of sizes seen in the canine population.

The modular design was achieved by creating a three-part implant. It consisted of separate distal, proximal and mid-diaphyseal components. All components were designed with an elliptical profile to mimic the natural cross-sectional shape of the radius. Both the proximal and distal components were incorporated with a locking-screw design to reduce the stress profile within the bone. Locking screws were implemented to address the problem of screw loosening observed in older generation endoprostheses.

The proximal endoprosthesis component (PEC) incorporated an intramedullary stem and a collar spanning 180 degrees of the cranial aspect of the radius [Figure 55]. The proximal radius screw holes were designed to be at 45 degrees on either side of the sagittal plane so as to place the screws away from the loading axis, thus reducing the offset bending loading on these implants [Figure 55]. The PEC also provided a flat surface for the distal radial surface to articulate with the native bone, thus providing an additional axial loading pathway and reducing stresses on the radial screws [Figure 55].

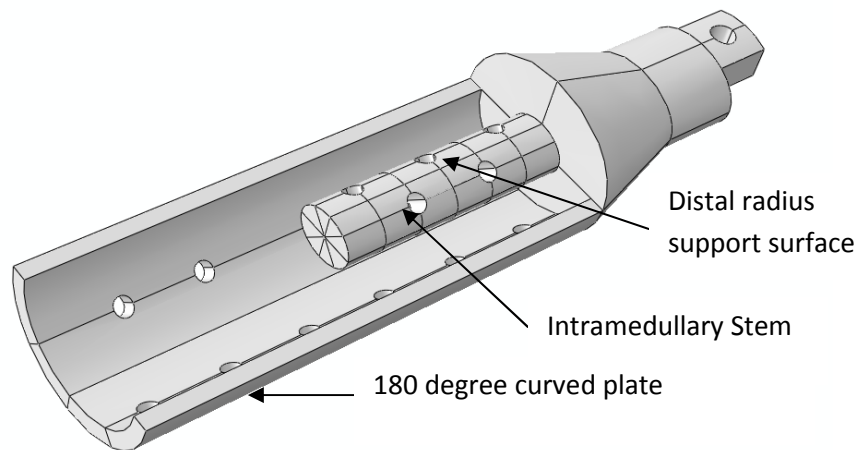


**Figure 55-Final proximal component (PEC).**

The mid-diaphyseal endoprosthesis component (MEC) was designed to be simple with respect to its geometry so as to provide the most ease in manufacturing multiple sizes of the component [Figure 56]. This provides the surgeon with the ability to more accurately fit the endoprosthesis to the length of the patient's limb. The MEC is rigidly fixed to the distal and proximal components with the use of 3.5 mm screws.

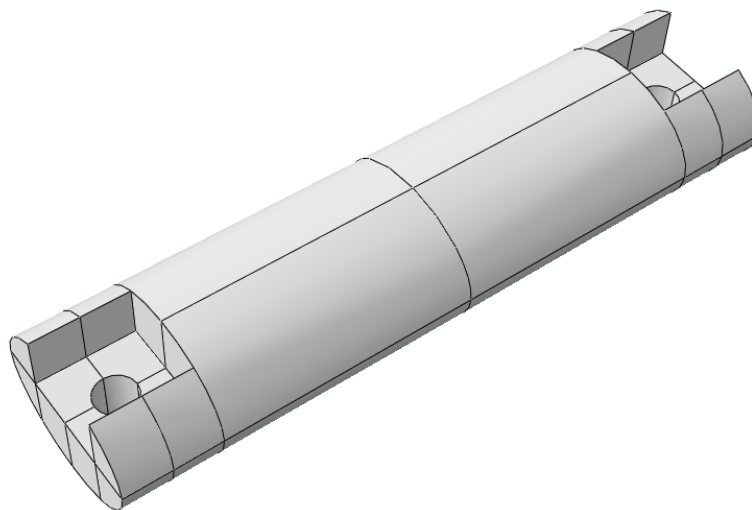


**Figure 56-Final mid-diaphyseal component (MEC).**

The distal endoprosthesis component (DEC) [Figure 57] is designed similar to the distal portion of the 2<sup>nd</sup> generation endoprosthesis since no significant mechanical stress issues were observed in this area as was documented in Chapter 5. 2.7 mm locking cortical screws are used owing to the small profile of the third metacarpal bone. A 3.5 mm screw hole is provided at the proximal end of the DEC plate to provide additional support through the radial carpal bone.

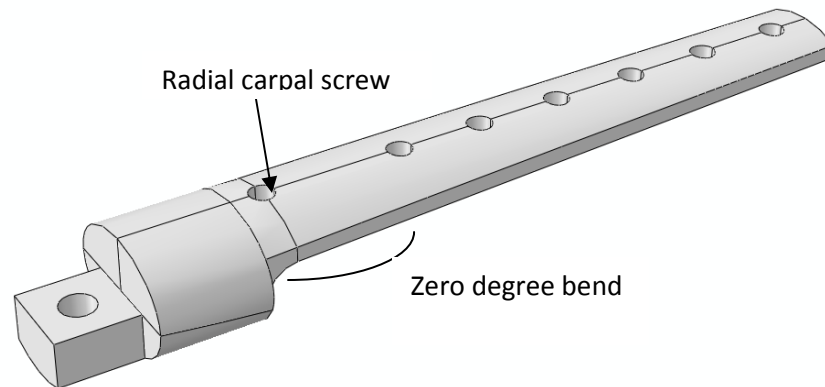


**Figure 57-Final distal endoprosthesis component (DEC).**

### **6.3.2 Ease of alignment between the proximal radius section and the carpus**

A clinically relevant problem associated with the second generation endoprosthesis was the intra-operative difficulty in obtaining proper alignment between the proximal radius and the carpus after tumor resection. To address this issue an intra-operative apparatus was designed to aid the surgeons in aligning the proximal radius and carpus [Figure 58].

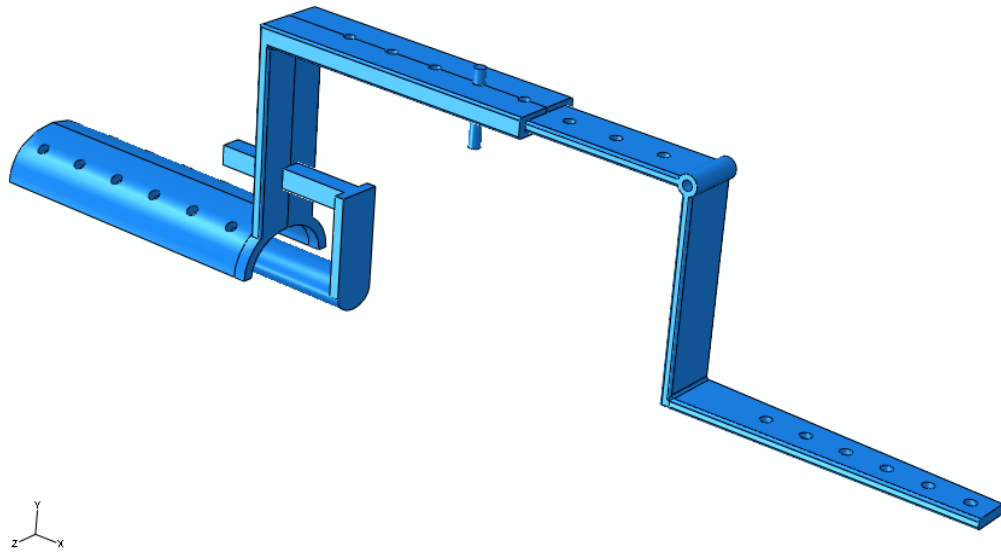


**Figure 58-The intra-operative apparatus for installation of new endoprosthesis.**

The intra-operative apparatus consisted of three parts. The proximal apparatus component (PAC) replicated the collar design of the proximal component of the endoprosthesis. The PAC incorporated a sleeve with graded alignment holes which exactly corresponded to the holes on the distal apparatus component (DAC) [Figure 59a]. These holes were provided for exact alignment of the PEC and DEC in combination with the various sizes of the MEC. A set-screw was provided to hold the PAC and DAC together in place after proper alignment of the components. The apparatus was elevated in the diaphyseal section for ease of handling. The DAC replicated the design of the DEC. The DAC was also provided with a hinge [Figure 59b] to allow the surgeon to open the apparatus while keeping the PAC and DAC in place. This feature allowed the surgeon more space to perform resection of the radius without interference from the apparatus components. The intramedullary apparatus component (IAC) [Figure 59c] replicated the intramedullary stem of the PEC. It enabled the surgeon to prepare the intramedullary canal of the radius (by use of reaming tools or hammering the IAC into place) to accurately fit the

intramedullary stem of the PEC. The IAC and PAC together created an exact replica of the PEC. The PAC also aided in drilling pilot holes for proper alignment of the PEC and DEC post-tumor resection. To this end, two pilot holes are provided proximally on the PAC and the PEC. During PEC implantation after tumor resection, these holes should be aligned exactly with the pilot holes in the radius, which are drilled previously with the help of the PAC.

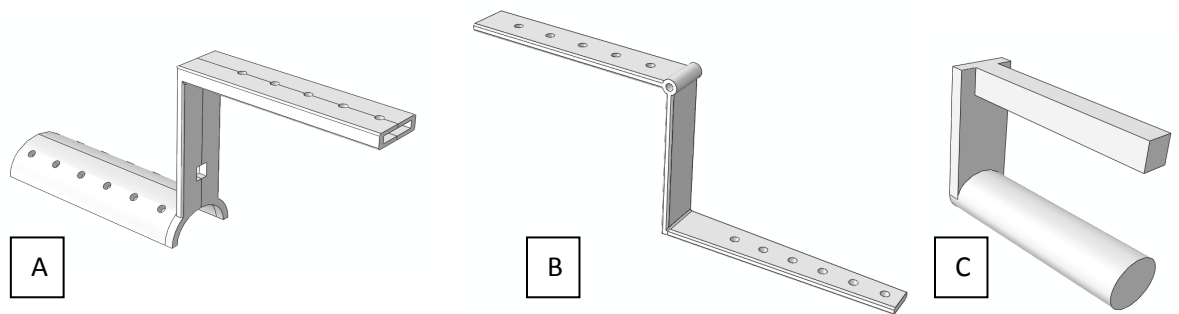


**Figure 59-Individual components of the apparatus (A) PAC (B) DAC (C) IAC.**

### **6.3.3 Stress reduction within the radial screws**

The essential failing of the 2<sup>nd</sup> generation endoprosthesis was the presence of high stresses within the radial screws. This was due to off-axis loading of the construct coupled with the high shear stresses observed by the screws due to the use of a non-locking plate design. For the development of a successful endoprosthesis these issues have to be resolved.

In the current design, all screws were locking screws to reduce the shear stresses within the radial screws. The construct was now designed to be placed in-line with the loading axis of the radius, which ensures essential load distribution among the endoprosthesis components. Finally, the distal surface of the radius was fully supported by the PEC, potentially reducing the bending effects on the radial screws.

#### **6.3.4 Procedure for implantation of endoprosthesis**

The following gives a step-by-step procedure for implanting the endoprosthesis using the above mentioned endoprosthesis and apparatus components.

1. After pre-operative radiographical evaluation of the cancerous forelimb, initial selection of the components (of the MEC in particular) is performed.
2. The PAC and DAC are aligned with the radius and third metacarpal bones, respectively, and alignment holes are drilled.
3. The apparatus is opened with the use of the hinge thus providing access to the radius. The radius is resected at the appropriate location.
4. The IAC is used to prepare the intramedullary canal of the radius to accept the PEC stem. An additional reamer tool can be used if required.
5. The PAC is removed and the PEC is fitted onto the radius while aligning it to the pre-drilled holes.
6. The DAC is removed and the DEC is fitted onto the third metacarpal. The DEC is fixed to the bone with the use of locking screws.
7. The PEC is fixed to the radius with the use of locking screws.
8. Finally, the MEC is fixed to both the PEC and DEC with the provided 3.5 mm screws.

For a successful implant design, all components within the construct have to be evaluated for their contribution, efficacy and redundancy. We identified the following parameters using our developed and validated finite element model:

1. The contribution of the intramedullary stem.
2. The effect of various angle adjustments in the DEC.
3. The effect of distal support to the DEC from the radial carpal bone.
4. The contribution of the radial screw with respect to stress dissipation.
5. The biomechanical contribution of the ulna.

The initial reference configuration for the complete construct included with the following contributions:

1. Intramedullary support provided.
2. Distal radius support provided.
3. Ulna support not provided.
4. Distal DEC support not provided.
5. Radial carpal screw support provided.

All locking interfaces were simulated with the use of tie constraints. Contact was established between all articulating surfaces of the implant with a coefficient of friction as 0.25 [96], and between the distal radius surface and the PEC with a coefficient of friction equal to 0.1. All metallic components were made from 316L stainless steel with a Young's modulus of 193GPa and a Poisson's ration of 0.3. All springs connecting the carpal bones were given a stiffness value of 110N/mm. The construct was implanted in the intact FE element model and loaded to 500N.

## **6.4 Results**

Using the aforementioned reference configuration, predicted a maximum von Mises stress of 216.9MPa was predicted at the most distal screw in the third metacarpal. The average von Mises stress within this screw was 110MPa, located between the plate and bone interface [Figure 60].

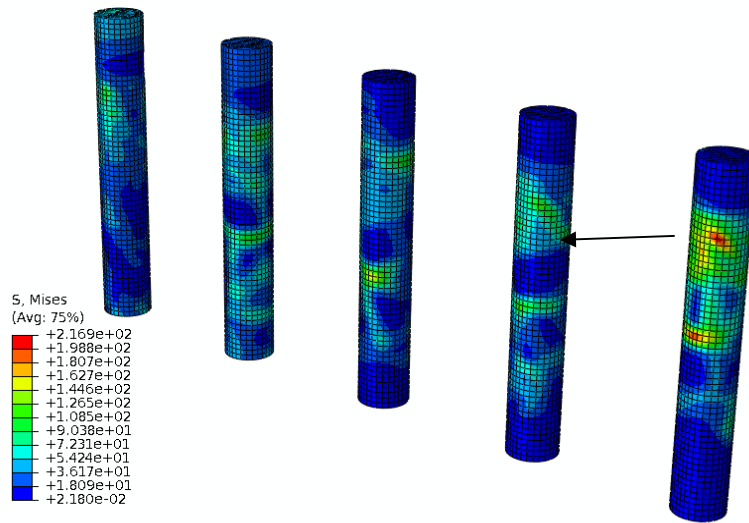


**Figure 60-von Mises stress distribution in the distal metacarpal screws. Arrow shows location of maximum stress (216MPa).**

A maximum von Mises stress of 205.2MPa was observed within the proximal radial screws, with an average von Mises stress of 95MPa predicted for all proximal radial screws [Figure 61].

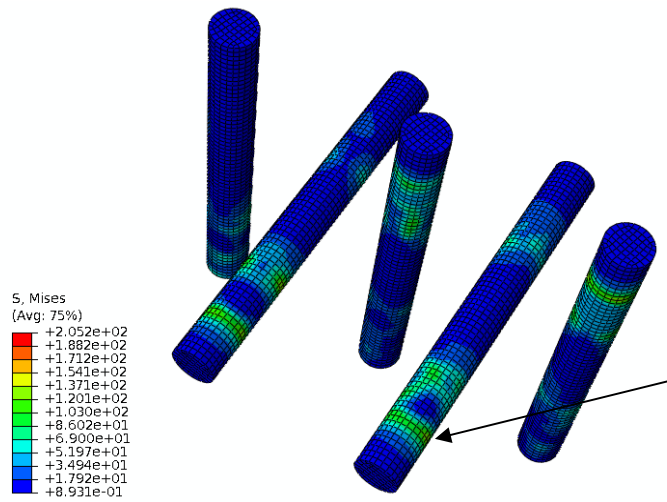


**Figure 61-von Mises stress distribution in the proximal radius screws. Arrow shows location of maximum stress (205MPa).**

The maximum von Mises stress in the radius was predicted to be 42.5MPa [Figure 62] and 57.1MPa in the third metacarpal bone [Figure 63]. The maximum von Mises stress predicted in

the PEC was 59.33MPa [Figure 64] and 79.3 MPa in the MEC [Figure 65]. The maximum von Mises stress within the DEC was 54.62MPa [Figure 66]. The 3.5 mm screws connecting the MEC to the PEC and DEC had a maximum von Mises stress of 46.01MPa.

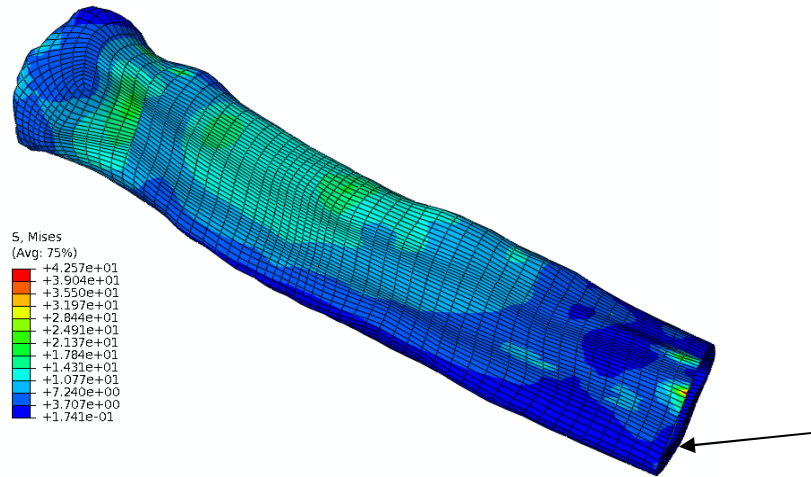


**Figure 62-von Mises stress distribution in the radius. Arrow shows location of maximum stress (42.5MPa).**

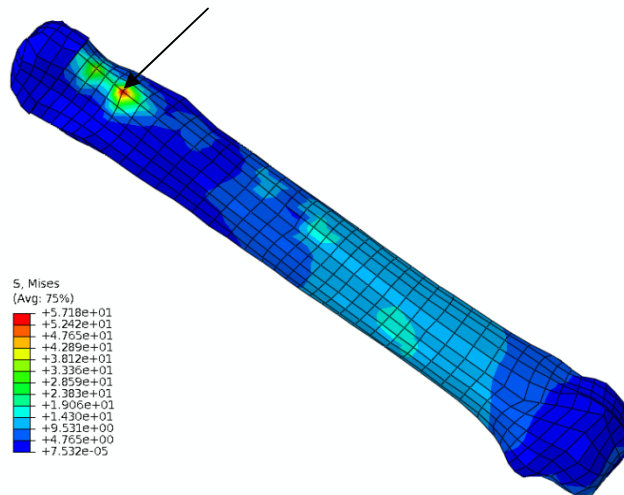


**Figure 63-von Mises stress distribution in the 3<sup>rd</sup> metacarpal. Arrow shows location of maximum stress (57 MPa).**

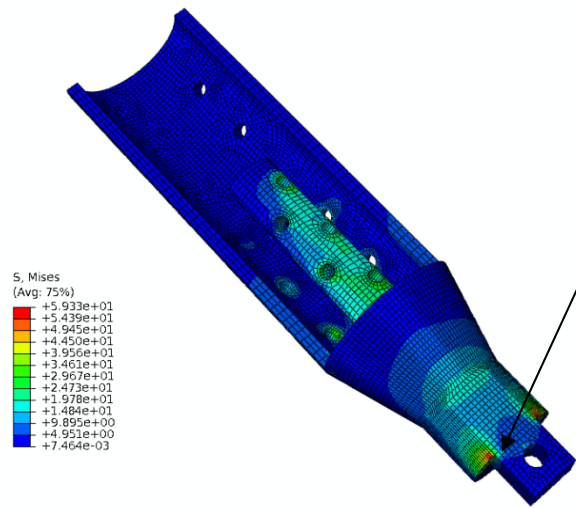


Figure 64-von Mises stress distribution in the PEC. Arrow shows the location of maximum stress (59.33MPa).

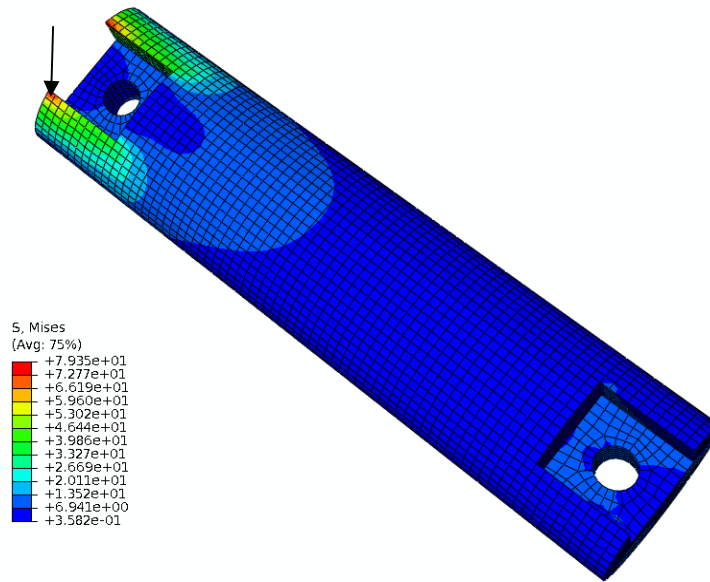
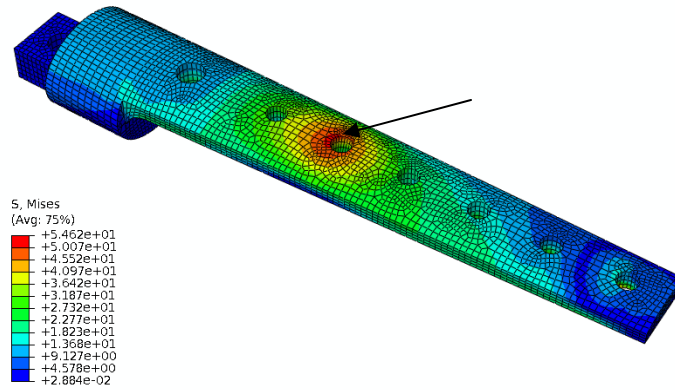


Figure 65-von Mises stress dsitribution in the MEC. Arrow shows location of maximum stress (79.3MPa).



**Figure 66-von Mises stress distribution in the DEC. Arrow shows location of maximum stress (54.6MPa).**

Support to the distal end of the DEC was simulated with tie constraints between the DEC and the proximal surface of the radial carpal bone. This addition resulted in relatively small changes to the stress predictions among all the components. The maximum stress predictions within the various components are tabulated in Figure 67. It also lists the change in stress predictions caused by preservation of the ulna during surgery.

Removal of the intramedullary stem from the proximal component produced large changes in the von Mises stress predictions within the proximal radial screws. The peak stress predictions remained the same, however, high bending stresses were observed in the screw area between the plate and the radius [Figure 68].

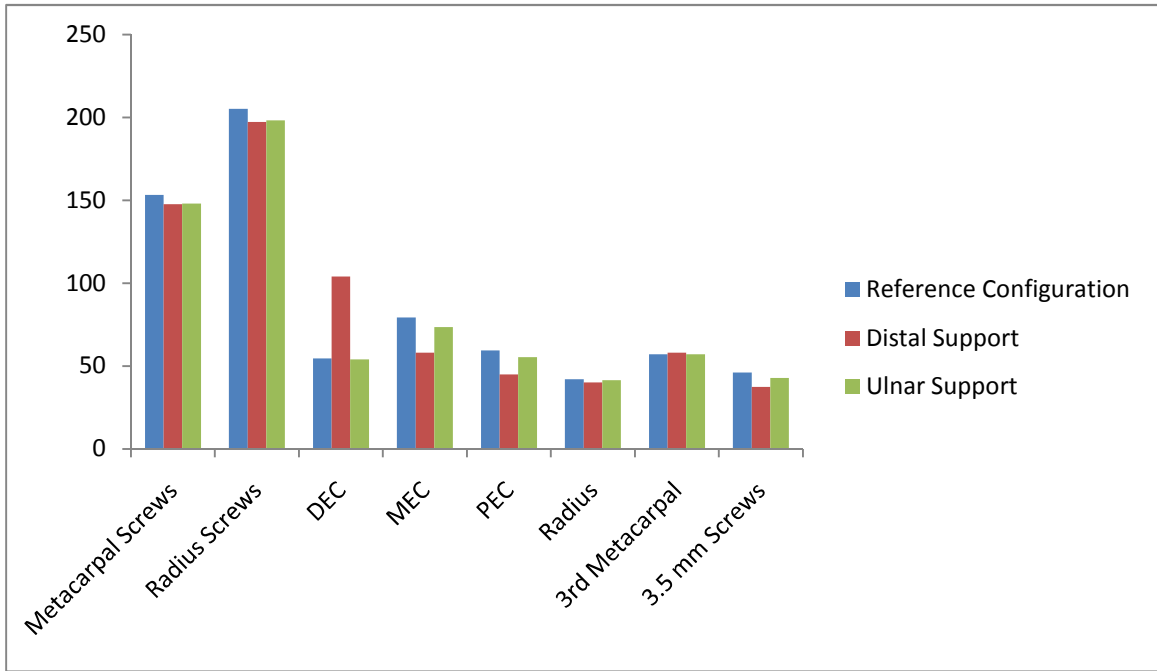


Figure 67-Comparison of peak von Mises stresses for three support conditions (Reference, distal support, ulnar support).

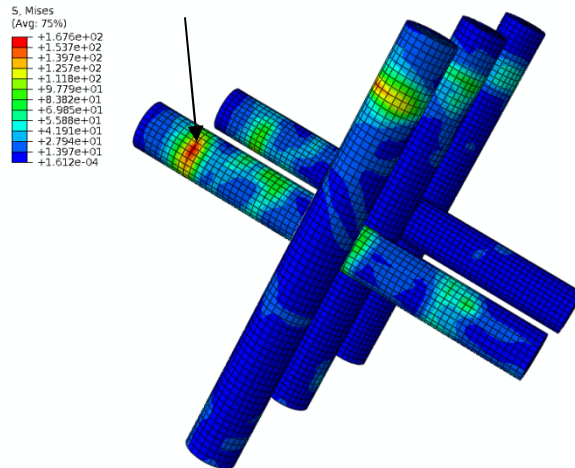


Figure 68-High bending stresses (arrows) due to removal of intramedullary stem support (167.6MPa).

## 6.4 Discussion

The major contributing factors for the failure of the 2<sup>nd</sup> generation endoprosthesis were loosening and fatigue failure of the proximal radial screws [56]. This prosthesis was comprehensively investigated using our computational model in the fifth chapter of this

dissertation. Other potential areas of improvement (as outlined by the CSU veterinary surgeons) were creation of a modular implant for addressing a broader range (size) of patients and development of a pre-operative apparatus for ease of alignment between the proximal radius and carpus after tumor resection.

The reason for high stresses in the proximal radius screws was determined to be the significant off-axis loading caused by the design of the 2<sup>nd</sup> generation implant. Hence, the new design merged the compression plate and metal spacer to more closely align the loading axis of the implant with that of the radius. In the second generation implant, the placement of the radial screws along the loading plane subjected them to a pure bending load. In the latest iteration, the radial screws were placed at an angle of 45 degrees on either side of the sagittal plane, thus alleviating the bending loads. This also allowed for the replacement of the current 3.5 mm cortical screws with 2.7 mm cortical screws. In addition, non-locking screws were replaced with locking screws to reduce the stress profile within the radius. All these changes resulted in a 50% reduction of the peak von Mises stress within the radial screws (as compared with the previous implant). Furthermore, the peak stresses at the bone-screw interface were reduced by a factor of 50%. Distal support to the radius was also an important design element for the observed reduction in von Mises stresses within the radius. Removal of the intramedullary stem resulted in relatively high bending stresses (167.6 MPa) within the radial screws where they entered into the radius. This can be attributed to the cantilever loading scenario caused by the absence of the stem and the use of locking screws. Hence, the stem plays an integral part in reducing the bending stresses within the radial screws.

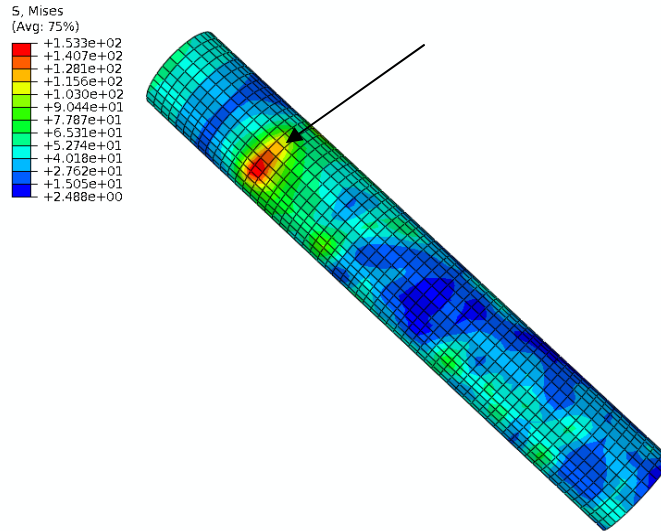


**Figure 69-Location of maximum von Mises stress after ignoring the stress concentrations due to tie constraints (153MPa).**

With the reduction of stresses in the proximal radius and designing for a through-axis loading condition, the highest stresses (weakest link) in the assembly were experienced by the 2.7 mm distal metacarpal cortical screws. The highest bending stresses (153MPa) [Figure 69] were observed at the most proximal screw, which mirrors the results observed in previously published studies [105] evaluating locking compression plate stability under anteroposterior bending loads. The location of this peak stress was between the plate and the 3<sup>rd</sup> metacarpal. This peak von Mises stress is safely below the endurance limit of 316L stainless steel, which has been reported to be 200 MPa (at 10 million cycles run-out, in Ringer’s solution).

The peak stresses observed within the distal metacarpal screws and the proximal radius screws were relatively high. However, these peak stress values can be attributed to the tie constraints used in simulating the union between bone and screw. These tie constraints caused an artifact increase in stress predictions within a single element [Figure 70]. The average stress values obtained from the predictions of the surrounding elements provide a more accurate representation of the average peak stress within the component. Hence, it was deemed that

these stress anomalies could be safely disregarded when considering future failure mechanisms of the device.

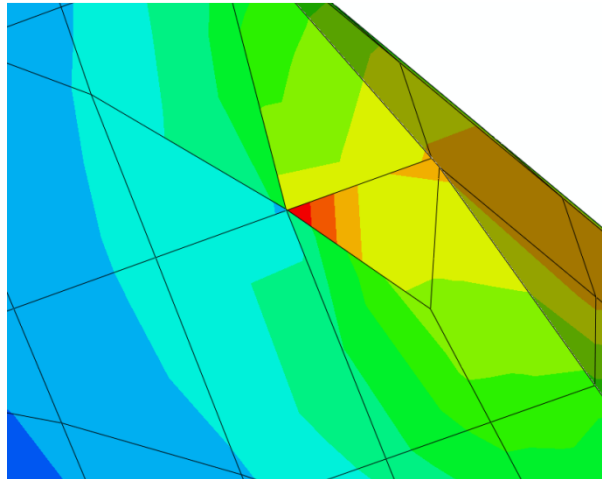


**Figure 70-Abnormal stress concentration caused by tie constraints.**

The addition of support to the distal end of the DEC (by tying the distal surface with the radial carpal bone) resulted in reduced stresses in the most proximal screw (in the 3<sup>rd</sup> metacarpal) of 147MPa as compared to the reference configuration. Therefore, it is recommended that intimate contact be established between the radial carpal bone and the PEC during implantation of the endoprosthesis. The addition of ulnar support did not result in any change in the stress predictions at the proximal metacarpal cortical screw. Hence, the ulna can be safely resected if needed.

A 2007 study by Ahmad *et al.* investigated the effect of distance between the locking plate and bone on implant stability. The authors recommended a distance of less than 2 mm between the bone and plate be established during implantation in order to produce increased axial stiffness. The current study, the average distance between the plate and 3<sup>rd</sup> metacarpal was 2.1 mm, which resulted in a maximum von Mises stress in the distal metacarpal screw of 286 MPa. When the 3<sup>rd</sup> metacarpal bone was spatially repositioned to achieve an average distance of 1.4 mm between the cranial surface of the 3<sup>rd</sup> metacarpal bone and the DEC, the peak stress predicted

at this screw was 216 MPa (reduction of 70MPa). Hence, it is recommended to achieve the minimum possible clearance between the distal locking plate and bone.

The proposed intra-operative apparatus design has been facilitated by extensive collaboration with the veterinary oncology surgical team at Colorado State University. The rigorous step-by-step procedure was evaluated by the collective investigative team and the difficulty in aligning the resected proximal radius with the carpus has theoretically been eliminated. However, this can only be confirmed after prototypes of the apparatus are built and evaluated in a cadaveric model.

The boundary conditions provided at the distal end of the metacarpals do not represent the physiological reality. However, the absence of extensor tendons and the phalangeal bones in the model restricts the application of the accurate boundary conditions present at these metacarpals. The effect of these physiological conditions can only be tested during laboratory and clinical trials of this endoprosthesis. The data indicate that the distal metacarpal screws are the weakest members of the entire implant. However, we hypothesize that kinematic constraint of the distal aspect of the metacarpus produced higher stresses in these screws than would ordinarily be the case had they been placed next to a flexible joint. Also, the small size of the 3<sup>rd</sup> metacarpal necessitates the use of 2.7 mm diameter cortical screws. It is definitely recommended that the size of these screws be increased to 3.5 mm or even 4.0 mm for large and giant breeds of the canine family.

#### **6.4.1 Tie Constraint Stress Predictions**

The stress predictions without special considerations for the tie constraints employed fall outside the fatigue limit of 316L stainless steel. This is a major point of contention in regards to the efficacy of the novel endoprosthesis design. The tie constraints used in the current study

employed a node-to-surface approach for coupling of bone and screw motion. The ABAQUS Analysis User's Manual [109] specifies that node-to-surface constraints do not include stress optimization algorithms, which are only available with surface-to-surface tie constraints. The absence of screw holes in the third metacarpal finite element mesh negated the use of surface-to-surface tie constraints. Therefore, the absence of stress optimization algorithms for node-to-surface tie constraints possibly caused these von Mises stress singularities. Fan *et al.* [110] found an increase of 40% in peak stress predictions with the use of tie constraints.

As with all studies, this study is not without its limitations. The efficacy of the new design under a cyclic loading scenario can only be assessed by performing biomechanical experiments under a rigorous cyclic regime. The stress anomalies produced due to the contact tie constraints employed, are a confounding factor, however, the use of the average stress value mitigates this effect when evaluating the peak stresses in the implant and screws. The size of the intramedullary stem is a simplification that will probably require attention in the future. A "one size fits all" approach has currently been employed; however, the validity of that approach can only be assessed with extensive clinical trials encompassing a wide range of patient sizes. A possible solution to this issue would be to provide a removable intramedullary stem. Obviously, this would alter the entire biomechanics of the construct, which should be investigated thoroughly.

## **7 Conclusion**

### **SUMMARY OF FINDINGS & FUTURE WORK**

Chapter 3 was devoted to the determination of mechanical properties of canine carpal ligaments. Six important carpal ligaments were tested uniaxially in a materials testing machine. Parameters such as stiffness (N/mm), modulus (N/mm<sup>2</sup>), failure load (N) and modes of failure were determined and documented. That data indicated a significant modulus-to-function relationship. These data filled a void in the literature regarding the properties of the canine carpus and aided in the development of a canine forelimb finite element model.

Chapter 4 described the development, convergence and validation of a comprehensive finite element model of the canine forelimb which included the antebrachial, carpal and metacarpal regions. To the best of our knowledge, no previous attempts had been made to develop an FE model involving such a high number of contact pairs. The convergence data indicated convergence of relevant parameters for the medium resolution model within 10% of the high resolution model. Validation of the model was performed by testing 8 intact canine forelimbs with the use of strain gauges and a motion analysis system. All investigated parameters were within one standard deviation of the experimental values. Thus, a validated and converged finite element model of the intact canine forelimb was achieved in Chapter 4.

Chapter 5 used the comprehensively developed finite element model of the canine forelimb developed in Chapter 4 to evaluate the current generation endoprosthesis. The exact mechanical and structural causes for failure of these implants (40% failure rate observed clinically) were determined. The presence of significant off-axis loading was the major cause of failure for these implants. Various stress reduction strategies were also investigated. These involved distal ulnar support and distal endoprosthesis support. The use of a locking plate in place of the current non-locking plate was also investigated. None of the stress reduction

strategies succeeded in reducing the observed stresses to acceptable values. This chapter provided significant insights with respect to the failure modes of the current generation endoprosthesis. These data were extremely valuable in the development of a new endoprosthesis design.

Chapter 6 described the development of a novel endoprosthesis for canine limb-sparing by addressing the shortcomings associated with the current design. A highly experienced investigative team comprised of surgeons and engineers was established. Numerous requirements for the new prosthesis were established by the team. The new design ensured through-axis loading of the prosthesis which was not established in the previous design and represented a major contributing factor for failure of the current generation endoprosthesis. The final design consisted of a three part construct. This facilitated the achievement of a “custom” fit for the patients. The intact finite element model was used for a thorough evaluation of the proposed design. A large reduction in stresses was observed within the proximal radial screws and the metacarpal screws. The predicted maximum von Mises stresses (147MPa) fell within the endurance limit of 316L stainless steel (200 MPa). Based on these results, the proposed design was approved for further biomechanical testing, fatigue analysis and clinical trials by the investigative team.

With regards to future work, the next step in the design process involves prototype development. To this end a prototype manufacture has been located and CAD drawings have been sent for manufacturing of the prototype implants. Biomechanical tests with the use of cadaveric canine forelimbs will be conducted. Longitudinal fatigue tests will also be performed with the use of replica bone specimens. The final step involving clinical trials will be conducted at the Colorado State University’s Veterinary Teaching Hospital Animal Cancer Center.

## 8 References

1. Rho, J.Y., L. Kuhn-Spearing, and P. Zioupos, *Mechanical properties and the hierarchical structure of bone*. Med Eng Phys, 1998. **20**(2): p. 92-102.
2. Mow, V.C., et al., *Biphasic creep and stress relaxation of articular cartilage in compression? Theory and experiments*. J Biomech Eng, 1980. **102**(1): p. 73-84.
3. Evans, H.E. and M.E. Miller, *Miller's anatomy of the dog*. 3rd ed. 1993, Philadelphia: W.B. Saunders. xvi, 1113 p.
4. Mason, D.R., et al., *In vitro force mapping of normal canine humeroradial and humeroulnar joints*. Am J Vet Res, 2005. **66**(1): p. 132-5.
5. Adams, D.R., *Canine anatomy : a systemic study*. 4th ed. 2004, Ames: Iowa State Press. vii, 488 p.
6. Mikic, Z.D., G. Ercegan, and T. Somer, *Detailed anatomy of the antebrachiocondylar joint in dogs*. Anat Rec, 1992. **233**(2): p. 329-34.
7. Mikic, Z.D., *Detailed anatomy of the articular disc of the distal radioulnar joint*. Clin Orthop Relat Res, 1989(245): p. 123-32.
8. Kaiser, A., H.G. Liebich, and J. Maierl, *Functional anatomy of the distal radioulnar ligament in dogs*. Anat Histol Embryol, 2007. **36**(6): p. 466-8.
9. Whitelock, R.G., J. Dyce, and J.E. Houlton, *Metacarpal fractures associated with pancarpal arthrodesis in dogs*. Vet Surg, 1999. **28**(1): p. 25-30.
10. Nordberg, C.C. and K.A. Johnson, *Magnetic resonance imaging of normal canine carpal ligaments*. Vet Radiol Ultrasound, 1999. **40**(2): p. 128-36.
11. Turan, E. and H. Erden, *Computed tomography and morphometry of the carpal canal in the dog*. Ann Anat, 2003. **185**(2): p. 173-8.

12. Warnock, J.J. and B.S. Beale, *Arthroscopy of the antebrachiocarpal joint in dogs*. J Am Vet Med Assoc, 2004. **224**(6): p. 867-74, 865.
13. Weiner, S. and W. Traub, *Bone structure: from angstroms to microns*. FASEB J, 1992. **6**(3): p. 879-85.
14. Womack, W.J. and Colorado State University. Dept. of Mechanical Engineering., *Computational modeling of the lower cervical spine : facet cartilage distribution and disc replacement*. 2009, Colorado State University, 2009. p. xiii, 122, 6 leaves.
15. Gong, J.K., J.S. Arnold, and S.H. Cohn, *Composition of Trabecular and Cortical Bone*. Anat Rec, 1964. **149**: p. 325-31.
16. Turner, C.H., A. Chandran, and R.M. Pidaparti, *The anisotropy of osteonal bone and its ultrastructural implications*. Bone, 1995. **17**(1): p. 85-9.
17. Carter, D.R. and W.C. Hayes, *The compressive behavior of bone as a two-phase porous structure*. J Bone Joint Surg Am, 1977. **59**(7): p. 954-62.
18. Rho, J.Y., R.B. Ashman, and C.H. Turner, *Young's modulus of trabecular and cortical bone material: ultrasonic and microtensile measurements*. J Biomech, 1993. **26**(2): p. 111-9.
19. Reilly, D.T., A.H. Burstein, and V.H. Frankel, *The elastic modulus for bone*. J Biomech, 1974. **7**(3): p. 271-5.
20. Choi, K., et al., *The elastic moduli of human subchondral, trabecular, and cortical bone tissue and the size-dependency of cortical bone modulus*. J Biomech, 1990. **23**(11): p. 1103-13.
21. Ciarelli, M.J., et al., *Evaluation of orthogonal mechanical properties and density of human trabecular bone from the major metaphyseal regions with materials testing and computed tomography*. J Orthop Res, 1991. **9**(5): p. 674-82.

22. Burstein, A.H., D.T. Reilly, and M. Martens, *Aging of bone tissue: mechanical properties*. J Bone Joint Surg Am, 1976. **58**(1): p. 82-6.
23. Wright, T.M. and W.C. Hayes, *Tensile testing of bone over a wide range of strain rates: effects of strain rate, microstructure and density*. Med Biol Eng, 1976. **14**(6): p. 671-80.
24. Helgason, B., et al., *Mathematical relationships between bone density and mechanical properties: a literature review*. Clin Biomech (Bristol, Avon), 2008. **23**(2): p. 135-46.
25. Rho, J.Y., T.Y. Tsui, and G.M. Pharr, *Elastic properties of human cortical and trabecular lamellar bone measured by nanoindentation*. Biomaterials, 1997. **18**(20): p. 1325-30.
26. Kuhn, J.L., et al., *The limitations of canine trabecular bone as a model for human: a biomechanical study*. J Biomech, 1989. **22**(2): p. 95-107.
27. Kang, Q., Y.H. An, and R.F. Friedman, *Mechanical properties and bone densities of canine trabecular bone*. J Mater Sci Mater Med, 1998. **9**(5): p. 263-7.
28. Pressel, T., et al., *Mechanical properties of femoral trabecular bone in dogs*. Biomed Eng Online, 2005. **4**(1): p. 17.
29. Kaneps, A.J., S.M. Stover, and N.E. Lane, *Changes in canine cortical and cancellous bone mechanical properties following immobilization and remobilization with exercise*. Bone, 1997. **21**(5): p. 419-23.
30. Mow, V.C. and R. Huiskes, *Basic orthopaedic biomechanics & mechano-biology*. 3rd ed. 2005, Philadelphia, PA: Lippincott Williams & Wilkins. p.
31. Torzilli, P.A. and V.C. Mow, *On the fundamental fluid transport mechanisms through normal and pathological articular cartilage during function--I. The formulation*. J Biomech, 1976. **9**(8): p. 541-52.
32. Lai, W.M., J.S. Hou, and V.C. Mow, *A triphasic theory for the swelling and deformation behaviors of articular cartilage*. J Biomech Eng, 1991. **113**(3): p. 245-58.

33. Elliott, D.M., et al., *Tensile properties of articular cartilage are altered by meniscectomy in a canine model of osteoarthritis*. J Orthop Res, 1999. **17**(4): p. 503-8.
34. Obeid, E.M., M.A. Adams, and J.H. Newman, *Mechanical properties of articular cartilage in knees with unicompartmental osteoarthritis*. J Bone Joint Surg Br, 1994. **76**(2): p. 315-9.
35. Shepherd, D.E. and B.B. Seedhom, *The 'instantaneous' compressive modulus of human articular cartilage in joints of the lower limb*. Rheumatology (Oxford), 1999. **38**(2): p. 124-32.
36. Wan, L., et al., *In vivo cartilage contact deformation of human ankle joints under full body weight*. J Orthop Res, 2008. **26**(8): p. 1081-9.
37. Woo, S.L.Y., et al., *Mechanical-Properties of Tendons and Ligaments .2. The Relationships of Immobilization and Exercise on Tissue Remodeling*. Biorheology, 1982. **19**(3): p. 397-408.
38. Shetye, S.S., et al., *Determination of mechanical properties of canine carpal ligaments*. Am J Vet Res, 2009. **70**(8): p. 1026-30.
39. Butler, D.L., et al., *Effects of structure and strain measurement technique on the material properties of young human tendons and fascia*. J Biomech, 1984. **17**(8): p. 579-96.
40. Withrow, S.J. and E.G. MacEwan, *Small animal clinical oncology*. 3rd ed. 2001, Philadelphia: W. B. Saunders. xvii, 718 p.
41. Tjalma, R.A., *Canine bone sarcoma: estimation of relative risk as a function of body size*. J Natl Cancer Inst, 1966. **36**(6): p. 1137-50.
42. Ru, G., B. Terracini, and L.T. Glickman, *Host related risk factors for canine osteosarcoma*. Vet J, 1998. **156**(1): p. 31-9.

43. Rosenberger, J.A., N.V. Pablo, and P.C. Crawford, *Prevalence of and intrinsic risk factors for appendicular osteosarcoma in dogs: 179 cases (1996-2005)*. J Am Vet Med Assoc, 2007. **231**(7): p. 1076-80.
44. Withrow, S.J., et al., *Comparative aspects of osteosarcoma. Dog versus man*. Clin Orthop Relat Res, 1991(270): p. 159-68.
45. Mueller, F., B. Fuchs, and B. Kaser-Hotz, *Comparative biology of human and canine osteosarcoma*. Anticancer Res, 2007. **27**(1A): p. 155-64.
46. Marina, N., et al., *Biology and therapeutic advances for pediatric osteosarcoma*. Oncologist, 2004. **9**(4): p. 422-41.
47. Withrow, S.J. and V.M. Hirsch, *Owner response to amputation of a pet's leg*. Vet Med Small Anim Clin, 1979. **74**(3): p. 332, 334.
48. Straw, R.C. and S.J. Withrow, *Limb-sparing surgery versus amputation for dogs with bone tumors*. Vet Clin North Am Small Anim Pract, 1996. **26**(1): p. 135-43.
49. Mauldin, G.N., et al., *Canine osteosarcoma. Treatment by amputation versus amputation and adjuvant chemotherapy using doxorubicin and cisplatin*. J Vet Intern Med, 1988. **2**(4): p. 177-80.
50. Bacon, N.J., et al., *Use of alternating administration of carboplatin and doxorubicin in dogs with microscopic metastases after amputation for appendicular osteosarcoma: 50 cases (1999-2006)*. J Am Vet Med Assoc, 2008. **232**(10): p. 1504-10.
51. Berg, J., et al., *Treatment of dogs with osteosarcoma by administration of cisplatin after amputation or limb-sparing surgery: 22 cases (1987-1990)*. J Am Vet Med Assoc, 1992. **200**(12): p. 2005-8.

52. Thrall, D.E., et al., *Radiotherapy prior to cortical allograft limb sparing in dogs with osteosarcoma: a dose response assay*. Int J Radiat Oncol Biol Phys, 1990. **18**(6): p. 1351-7.
53. Kuntz, C.A., et al., *Limb salvage surgery for osteosarcoma of the proximal humerus: outcome in 17 dogs*. Vet Surg, 1998. **27**(5): p. 417-22.
54. Morello, E., et al., *Bone allografts and adjuvant cisplatin for the treatment of canine appendicular osteosarcoma in 18 dogs*. J Small Anim Pract, 2001. **42**(2): p. 61-6.
55. Straw, R.C., et al., *The effect of intramedullary polymethylmethacrylate on healing of intercalary cortical allografts in a canine model*. J Orthop Res, 1992. **10**(3): p. 434-9.
56. Liptak, J.M., et al., *Cortical allograft and endoprosthesis for limb-sparing surgery in dogs with distal radial osteosarcoma: a prospective clinical comparison of two different limb-sparing techniques*. Vet Surg, 2006. **35**(6): p. 518-33.
57. Liptak, J.M., et al., *Cortical bone graft and endoprosthesis in the distal radius of dogs: a biomechanical comparison of two different limb-sparing techniques*. Vet Surg, 2006. **35**(2): p. 150-60.
58. Brekelmans, W.A., H.W. Poort, and T.J. Slooff, *A new method to analyse the mechanical behaviour of skeletal parts*. Acta Orthop Scand, 1972. **43**(5): p. 301-17.
59. Huiskes, R. and E.Y. Chao, *A survey of finite element analysis in orthopedic biomechanics: the first decade*. J Biomech, 1983. **16**(6): p. 385-409.
60. Carrigan, S.D., et al., *Development of a three-dimensional finite element model for carpal load transmission in a static neutral posture*. Ann Biomed Eng, 2003. **31**(6): p. 718-25.
61. Anderson, D.D. and T.E. Daniel, *A contact-coupled finite element analysis of the radiocarpal joint*. Semin Arthroplasty, 1995. **6**(1): p. 30-6.

62. Lewis, G. and S.R. Vannappagari, *Finite element stress analysis of the wrist joint without and with an endoprosthesis*. Semin Arthroplasty, 1995. **6**(1): p. 20-9.
63. Gislason, M.K., et al., *A three-dimensional finite element model of maximal grip loading in the human wrist*. Proc Inst Mech Eng H, 2009. **223**(7): p. 849-61.
64. Guo, J.Y., et al., *Performances of one-dimensional sonomyography and surface electromyography in tracking guided patterns of wrist extension*. Ultrasound Med Biol, 2009. **35**(6): p. 894-902.
65. Troy, K.L. and M.D. Grabiner, *Off-axis loads cause failure of the distal radius at lower magnitudes than axial loads: a finite element analysis*. J Biomech, 2007. **40**(8): p. 1670-5.
66. Ulrich, D., et al., *Load transfer analysis of the distal radius from in-vivo high-resolution CT-imaging*. J Biomech, 1999. **32**(8): p. 821-8.
67. Rogge, R.D., B.D. Adams, and V.K. Goel, *An analysis of bone stresses and fixation stability using a finite element model of simulated distal radius fractures*. J Hand Surg Am, 2002. **27**(1): p. 86-92.
68. Guo, X., Y. Fan, and Z.M. Li, *Effects of dividing the transverse carpal ligament on the mechanical behavior of the carpal bones under axial compressive load: a finite element study*. Med Eng Phys, 2009. **31**(2): p. 188-94.
69. Coleman, J.C., R.T. Hart, and D.B. Burr, *Reconstructed bone end loads on the canine forelimb during gait*. J Biomech, 2003. **36**(12): p. 1837-44.
70. Ayturk, U.M. and Colorado State University. Dept. of Mechanical Engineering., *Development and validation of a three dimensional high resolution nonlinear finite element model of an L3/L4 functional spinal unit*. 2007, Colorado State University, 2007. p. xi, 90 leaves.

71. Ruckh, T. and Colorado State University. Dept. of Mechanical Engineering., *Development of a high resolution finite element knee model*. 2008, Colorado State University, 2008. p. 98 leaves.
72. Bronzino, J.D., *The biomedical engineering handbook*. 2nd ed. The electrical engineering handbook series. 2000, Boca Raton, FL: CRC Press.
73. Merk, B.R., et al., *A fatigue life analysis of small fragment screws*. J Orthop Trauma, 2001. **15**(7): p. 494-9.
74. Niinomi, M., *Fatigue characteristics of metallic biomaterials*. International Journal of Fatigue, 2007. **29**(6): p. 992-1000.
75. Jones, A.C. and R.K. Wilcox, *Assessment of factors influencing finite element vertebral model predictions*. J Biomech Eng, 2007. **129**(6): p. 898-903.
76. Crawford, R.P., W.S. Rosenberg, and T.M. Keaveny, *Quantitative computed tomography-based finite element models of the human lumbar vertebral body: effect of element size on stiffness, damage, and fracture strength predictions*. J Biomech Eng, 2003. **125**(4): p. 434-8.
77. Viceconti, M., et al., *Extracting clinically relevant data from finite element simulations*. Clin Biomech (Bristol, Avon), 2005. **20**(5): p. 451-4.
78. Amar, J., *Trottoir dynamographique*. Comptes rendus hebdomadaires des seances de l, Academie des Sciences, 1916. **163**: p. 130-133.
79. Dueland, R., D.L. Bartel, and E. Antonson, *Force plate technique for canine gait analysis: preliminary report on total hip and excision arthroplasty [proceedings]*. Bull Hosp Joint Dis, 1977. **38**(1): p. 35-6.
80. Budsberg, S.C., M.C. Verstraete, and R.W. Soutas-Little, *Force plate analysis of the walking gait in healthy dogs*. Am J Vet Res, 1987. **48**(6): p. 915-8.

81. Budsberg, S.C., et al., *Vertical loading rates in clinically normal dogs at a trot*. Am J Vet Res, 1995. **56**(10): p. 1275-80.
82. Bennett, R.L., et al., *Kinematic gait analysis in dogs with hip dysplasia*. Am J Vet Res, 1996. **57**(7): p. 966-71.
83. DeCamp, C.E., et al., *Kinematic gait analysis of the trot in healthy greyhounds*. Am J Vet Res, 1993. **54**(4): p. 627-34.
84. Hottinger, H.A., et al., *Noninvasive kinematic analysis of the walk in healthy large-breed dogs*. Am J Vet Res, 1996. **57**(3): p. 381-8.
85. Nielsen, C., et al., *Two-dimensional link-segment model of the forelimb of dogs at a walk*. Am J Vet Res, 2003. **64**(5): p. 609-17.
86. Schaefer, S.L., et al., *Kinematic gait analysis of hind limb symmetry in dogs at the trot*. Am J Vet Res, 1998. **59**(6): p. 680-5.
87. Bockstahler, B.A., et al., *Reliability of ground reaction forces measured on a treadmill system in healthy dogs*. Vet J, 2007. **173**(2): p. 373-8.
88. Parker, R.B., S.G. Brown, and A.P. Wind, *Pancarpal Arthrodesis in the Dog - a Review of 45 Cases*. Veterinary Surgery, 1981. **10**(1): p. 35-43.
89. LaRue, S.M., et al., *Limb-sparing treatment for osteosarcoma in dogs*. J Am Vet Med Assoc, 1989. **195**(12): p. 1734-44.
90. Savelberg, H.H., et al., *Stiffness of the ligaments of the human wrist joint*. J Biomech, 1992. **25**(4): p. 369-76.
91. Coughlan, A.R., A. Miller, and British Small Animal Veterinary Association., *BSAVA manual of small animal fracture repair and management*. 1998, Shurdington, Cheltenham, U.K.: British Small Animal Veterinary Association. vii, 348 p.

92. Donahue, T.L., et al., *A finite element model of the human knee joint for the study of tibio-femoral contact*. J Biomech Eng, 2002. **124**(3): p. 273-80.
93. Piermattei, D.L., G.L. Flo, and C.E. DeCamp, *Brinker, Piermattei, and Flo's handbook of small animal orthopedics and fracture repair*. 4th ed. 2006, St. Louis, Mo.: Saunders/Elsevier. 818 p.
94. Turner, C.H., et al., *High frequency components of bone strain in dogs measured during various activities*. J Biomech, 1995. **28**(1): p. 39-44.
95. Coleman, J.C., et al., *Characterization of dynamic three-dimensional strain fields in the canine radius*. J Biomech, 2002. **35**(12): p. 1677-83.
96. Oberg, E., C.J. McCauley, and Knovel (Firm), *Machinery's handbook a reference book for the mechanical engineer, designer, manufacturing engineer, draftsman toolmaker and machinist*. 2004, Industrial Press: New York. p. ix, 2693 p.
97. Seguin, B., et al., *Use of an ipsilateral vascularized ulnar transposition autograft for limb-sparing surgery of the distal radius in dogs: An anatomic and clinical study*. Veterinary Surgery, 2003. **32**(1): p. 69-79.
98. Jehn, C.T., et al., *Transverse ulnar bone transport osteogenesis: A new technique for limb salvage for the treatment of distal radial osteosarcoma in dogs*. Veterinary Surgery, 2007. **36**(4): p. 324-334.
99. Egol, K.A., et al., *Biomechanics of locked plates and screws*. J Orthop Trauma, 2004. **18**(8): p. 488-93.
100. Perren, S.M., *Evolution of the internal fixation of long bone fractures. The scientific basis of biological internal fixation: choosing a new balance between stability and biology*. J Bone Joint Surg Br, 2002. **84**(8): p. 1093-110.

101. Miller, D.L. and T. Goswami, *A review of locking compression plate biomechanics and their advantages as internal fixators in fracture healing*. Clin Biomech (Bristol, Avon), 2007. **22**(10): p. 1049-62.
102. Gardner, M.J., et al., *Hybrid locked plating of osteoporotic fractures of the humerus*. J Bone Joint Surg Am, 2006. **88**(9): p. 1962-7.
103. Freeman, A.L., et al., *How much do locked screws add to the fixation of "hybrid" plate constructs in osteoporotic bone?* J Orthop Trauma. **24**(3): p. 163-9.
104. Wagner, M., *General principles for the clinical use of the LCP*. Injury, 2003. **34 Suppl 2**: p. B31-42.
105. Stoffel, K., et al., *Biomechanical testing of the LCP--how can stability in locked internal fixators be controlled?* Injury, 2003. **34 Suppl 2**: p. B11-9.
106. Roberts, J.W., et al., *Biomechanical evaluation of locking plate radial shaft fixation: unicortical locking fixation versus mixed bicortical and unicortical fixation in a sawbone model*. J Hand Surg Am, 2007. **32**(7): p. 971-5.
107. Snow, M., G. Thompson, and P.G. Turner, *A mechanical comparison of the locking compression plate (LCP) and the low contact-dynamic compression plate (DCP) in an osteoporotic bone model*. J Orthop Trauma, 2008. **22**(2): p. 121-5.
108. Zand, M.S., S.A. Goldstein, and L.S. Matthews, *Fatigue failure of cortical bone screws*. J Biomech, 1983. **16**(5): p. 305-11.
109. *Abaqus Analysis User's Manual*. (Version 6.9EF2).
110. Bhatti, X.F.M.P.P.K., *Effect of Finite Element Modeling Techniques on Solder Joint Fatigue Life Prediction of Flip-Chip BGA Packages*. Electronic Components and Technology Conference, 2006: p. 9.